nergy

SOLAR

535
9/27/84
mlr

DR-0432-4

DOE/JPL-1012-97
(DE84014963)

PHOTOVOLTAIC MODULE ENCAPSULATION DESIGN AND MATERIALS SELECTION: VOLUME II

By
E. Cuddihy

June 1, 1984

Work Performed Under Contract No. AI01-76ET20356

Jet Propulsion Laboratory
Pasadena, California

Technical Information Center
Office of Scientific and Technical Information
United States Department of Energy

DISCLAIMER

DISCLAIMER

5101-237
Flat-Plate
Solar Array Project

DOE/JPL-1012-97
(JPL-Pub-84-34)
(DE84014963)
Distribution Category UC-63b

Photovoltaic Module Encapsulation Design and Materials Selection: Volume II

E. Cuddihy

June 1, 1984

Prepared for
U.S. Department of Energy
Through an Agreement with
National Aeronautics and Space Administration
by
Jet Propulsion Laboratory
California Institute of Technology
Pasadena, California

JPL Publication 84 34

THIS PAGE

WAS INTENTIONALLY

LEFT BLANK

ABSTRACT

This is Volume II of "Photovoltaic Module Encapsulation Design and Materials Selection": a periodically updated handbook of encapsulation technology, developed with the support of the Flat-Plate Solar Array Project (FSA), managed for the Department of Energy (DOE) by the Jet Propulsion Laboratory.

Volume I (Reference 1), published June 1, 1982, described encapsulation-material system requirements, material-selection criteria, and the status and properties of encapsulation materials and processes available to module manufacturers. Technical and economic goals established for photovoltaic modules and encapsulation systems and their status were described, to assist material suppliers in assessing the suitability of materials in their product lines and the potential of new-material products. A comprehensive discussion of available encapsulation technology and data was presented to facilitate design and material selection for silicon flat-plate photovoltaic modules, using the best materials available and processes optimized for specific power applications and geographic sites.

Volume II extends and supplements Volume I by describing FSA encapsulation technology developed between June 1, 1982, and January 1, 1984. Emphasis during this period shifted from materials development to demonstration of reliability and durability in an outdoor environment; the updated information in this volume reflects the developing technology base related to both reliability and encapsulation process improvements.

FOREWORD

This document is the second (Volume II) in a planned series that is intended to bring together in an organized presentation, a technically unified overview of all of the various JPL and contractor activities carried out in support of encapsulation technology. These documents are therefore intended not to duplicate JPL and contractor reports, but only to extract from them their essential technical findings. Readers interested in more details or in experimental reports are encouraged to consult the specific JPL or contractor reports referenced in Volumes I and II.

ACKNOWLEDGMENT

The editor gratefully acknowledges the assistance and encouragement of all of the JPL and contractor members of the Encapsulation Task of the Flat-Plate Solar Array Projects for their contributions to this report. Thanks are especially due to John Repar, who prepared the report on the evaluation of shrinkage in Tedlar films (Subsection II H).

CONTENTS

Figures

Tables

SECTION I

INTRODUCTION

A. PURPOSE

This series of reports is for photovoltaic (PV) module manufacturers, designers, and the material supply industry who may be developing and selling module encapsulant materials. The encapsulation system for a flat-plate PV module is a configuration of selected materials required to provide electrical isolation, structural support, and environmental protection for an assembly of active PV solar cells and associated electrical circuitry. The encapsulation protects the solar cells during operation, handling, shipping, installation, and maintenance. Protection is also intended for those working near modules in arrays that may be operating at electrical potentials of 3000 V above ground.

These reports will always be subject to additions and updates, because progress in solar technology areas is rapid. Activities within the Flat-Plate Solar Array Project (FSA) of the Jet Propulsion Laboratory (JPL) and within private industry are continually providing new data on the properties and characteristics of available materials and processes and are developing new and improved ones.

Many JPL and contractor reports on various aspects of PV encapsulation technology have already been published, the results of which are only summarized here. References are made to the published reports for those seeking greater detail or background material. For reader information, Table 1 consists of the table of contents of Volume I.

B. ENCAPSULATION UPDATE TO JANUARY 1, 1984

Table 2 is a list of candidate encapsulation materials currently being evaluated experimentally by FSA and industry, updated from Volume I of this series on photovoltaic module encapsulation design and materials selection (Reference 1). One new material appears in the list, a liquid casting polyurethane pottant designated Z-2591, which is marketed by Development Associates, North Kingston, Rhode Island. This clear and transparent commercial polyurethane is formulated for exterior applications as a weather-protection coating for automotive emblems, outdoor signs, etc. Early test results from exposure of this material to UV at 50°C in RS/4 chambers at Springborn Laboratories and in UV test chambers at JPL are encouraging. During the last year this polyurethane has also received favorable evaluation by several PV manufacturers.

The other liquid pottant candidate, poly-n-butyl acrylate (PnBA), has undergone extensive industrial evaluation, and although it performed well as a pottant, it was rejected by all of the industrial evaluators for the same reason: the material, as currently formulated, has a strong, unpleasant chemical odor that was found offensive by those working with the material. The source of this odor is the n-butyl acrylate monomer used in the uncured liquid system. Ways of correcting this problem are being explored, but pilot-plant production of this pottant for industrial evaluation has been stopped.

Table 1. Table of Contents for Volume I (Reference 1)

Table 1. Table of Contents for Volume I (Reference 1) (Cont'd)

Table 1. Table of Contents for Volume I (Reference 1) (Cont'd)

Table 1. Table of Contents for Volume I (Reference 1) (Cont'd)

Table 2. Candidate Encapsulation Materials Being Evaluated Experimentally by FSA and Industry

Function	Material	Type	Source
Low-Soiling Surface Material	Fluorinated silane	L-1668	3M
	Perfluorodecanoic acid, Dow Corning Z-6020 primer	E-3820	Dow Corning
UV Screening Front Cover	Low-iron tempered float glass	E.g., Sunadex glass	ASG
	UV-screening acrylic films	Acrylar X-22416 2 mils thick	3M
		Acrylar X-22417 3 mils thick	3M
	UV-screening PVF fluorocarbon film	Tedlar 100BG30UT 1 mil thick	Du Pont
Pottant	EVA	A-9918	Springborn, Du Pont, and Rowland, Inc., Berlin, Connecticut
	Ethylene methyl acrylate (EMA)	A-11877	Springborn
	Poly-n-butyl acrylate (PnBA)	BA-13870	Springborn
	Polyurethane	Z-2591	Development Associates, North Kingston, Rhode Island
Porous Spacer	Craneglas non-woven E-glass material	Type 230, 5 mils thick	Electrolock, Inc. Chagrin Falls, Ohio
Dielectric Film	Candidates are the front and back cover plastic film		

Table 2. Candidate Encapsulation Materials Being Evaluated Experimentally by FSA (Cont'd)

Function	Material	Type	Source
Substrates	Mild steel	Cold-rolled	Various
	Hardboards	Super-Dorlux, 1/8 in. thick	Masonite
		Duron, 1/8 in. thick	U.S. Gypsum
Back Covers	White-pigmented plastic film	Tedlar 150BL30WH, 1.5 mils thick	Du Pont
	White-pigmented plastic film	Tedlar 400BS20WH, 4.0 mils thick	Du Pont
	White-pigmented plastic film	Scotchpar 10 CP White 1.0 mil thick	3M
	White-pigmented plastic film	Scotchpar 20 CP White 2.0 mils thick	3M
	White-pigmented plastic film	Korad 63000 White, 3.0 mils thick	Xcel Corp.
Edge Seal and Gasket	Butyl edge-sealing tape	5354	3M
	EPDM gasket-sealing tape	E-633	Pawling Rubber Co., Pawling, New York

Not yet included in the list of pottants in Table 1 is a new, experimental version of ethylene vinyl acetate (EVA) containing a different peroxide curing agent, Lupersol TBEC. As is described in more detail in subsection IIA, the Lupersol 101 peroxide curing agent that is used in the current EVA A-9918 formulation has a tendency to evaporate out of the EVA. If it occurs, this prevents the A-9918 EVA from curing. Preliminary testing indicates that this problem is avoided with Lupersol TBEC. Experimental quantities of EVA containing Lupersol TBEC peroxide curing agent are available from Springborn Laboratories, Inc., for industrial evaluation. The designation of this experimental EVA is EVA 15295.

Also not included in Table 1 is a very recently identified new white film being introduced commercially by the Mobil Chemical Co. This white film is a two-ply laminate consisting of a core of white-pigmented polypropylene, with a thin exterior ply of Saran on one side and a thin exterior ply of a proprietary acrylic on the other side. The nominal thickness of this film is about 1.7 mils, at a selling price on the order of 1.9 /ft^2. Samples of this film will be supplied to FSA for evaluation during the next year.

Emphasis in the encapsulation materials program has shifted from materials development to demonstration of reliability and durability of materials and advanced encapsulation designs for long service life in the outdoor environment. In addition, there is some increased emphasis on improving the encapsulation processibility of already-identified pottants, such as faster curing at lower temperatures. The updated information given in this volume will reflect the developing technology base related to both reliability and encapsulation process improvements.

Noteworthy during the year was the completion and start-up of a novel accelerated aging technique using outdoor racks on which test materials and modules can be heated to fixed temperature levels above ambient, to accelerate aging from exposure to the natural weathering elements, e.g., oxygen, UV, humidity and pollution. Trial outdoor aging tests are currently being carried out at 70°C, 90°C and 105°C. The outdoor heating racks are programmed to turn on at 6:00 a.m. to a preset temperature, and to turn off at 6:00 p.m. to permit test materials and modules to cool overnight. It is intended that the rates of change of material properties and module performance parameters monitored at elevated temperatures in the natural environment can be used to estimate ongoing rates at the lower temperatures associated with actual module performance.

Also during the past year a program activity was initiated to explore the use of conducting polymers as transparent, electrically conducting anti-reflection coatings on solar cells.

SECTION II

TECHNICAL SECTION

A. ETHYLENE VINYL ACETATE

1. Chemical Structure

An analysis (Reference 2) of the polymeric structure of Elvax 150 EVA indicates that this material is a block copolymer; its structure is depicted in Figure 1. One of the two blocks is pure polyethylene, and the other block is a random copolymer of ethylene and vinyl acetate. The composition of Elvax 150 is 33 wt % vinyl acetate and 67 wt % ethylene, and the analysis indicates that the 67 wt % ethylene is divided between the two blocks as 53 wt % in the polyethylene block and 14 wt % in the copolymer block. Chemically, more than half of Elvax 150 EVA is polyethylene. The significance of this with respect to peroxide curing is described below in this section.

2. Material Properties

A data base of the material properties of cured A-9918 EVA is emerging as the material is more intensively studied. Accumulated data on material properties are compiled in Table 3, with material properties of uncured and uncompounded Elvax 150 for comparison. The quoted data on properties for cured A-9918 EVA have been accumulated over time as needs arose for various FSA contractors and JPL in-house studies, and in general are distributed throughout a plethora of contractor and JPL documents and in a recently published Du Pont technical bulletin. The primary sources are listed in the footnote of Table 3. The properties of Elvax 150 are taken from Du Pont technical bulletins for that product.

The major effects of crosslinking Elvax 150 are an increase in tensile strength and hardness, and a decrease in elongation-at-break and in density (Table 1). There is a slight increase in optical transmittance and Young's modulus. All other properties measured in common are essentially unaffected by crosslinking. Figure 2 is a plot of the optical transmittance of cured A-9918 EVA over the wavelength region from 390 nm to 1105 nm, reproduced from Du Pont Technical Bulletin "Elvax 150 Resin as a Solar Photovoltaic Module Pottant, Technical Guide," Polymer Products Dept., Technical Services Laboratory, Wilmington, Delaware, June 1982.

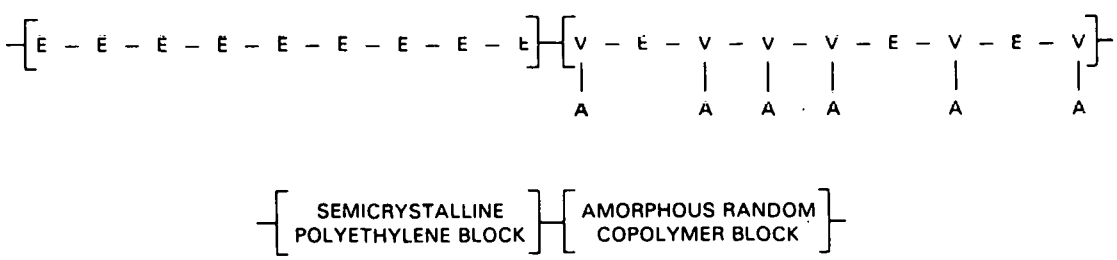

Figure 1. Polymeric Structure of Elvax 150 EVA: Block Copolymer

Table 3. Properties[a] of Elvax 150 and Cured A-9918 EVA

Property	Condition	Elvax 150	Cured E-9918 EVA	Remarks
Optical Transmission		90.5%	91.0%	ASTM E-424 (Springborn)
Glass Transition Temperature, T_g		-43°C	-43°C	JPL measurement
Young's Modulus[b]	23°C	850 lb/in.^{2}	890 lb/in.^{2}	ASTM D-638 (Springborn)
	23°C	700 lb/in.^{2}	-	ASTM D-1708 (Du Pont)
Secant Modulus	1% elongation, 23°C	-	1120-1330 lb/in.^{2}	ASTM D-882 (Du Pont)
Tensile Strength at Break	23°C	850 lb/in.^{2}	1890 lb/in.^{2}	ASTM D-638 (Springborn)
	23°C	700-900 lb/in.^{2}*	1160-1490 lb/in.^{2}**	ASTM D-638*/D-882** (Du Pont)
	23°C	850 lb/in.^{2}	-	ASTM D-1708 (Du Pont)
	-20°C	2700 lb/in.^{2}	-	ASTM D-638 (Du Pont)
Elongation at Break	23°C	1050%	510%	ASTM D-638 (Springborn)
	23°C	900%-950%*	580 - 740%**	ASTM D-638*/D-882** (Du Pont)
	23°C	1050%		ASTM D-1708 (Du Pont)
	-20°C	300%	-	ASTM D-638 (Du Pont)
Flexural Modulus	23°C	1000 lb/in.^{2}	-	ASTM D-790 (Du Pont)
Compression Modulus	10 days at 25°C	65%	-	ASTM D-395 (Du Pont)
	22 h at 70°C	91%	-	ASTM D-395 (Du Pont)
Stiffness	23°C	800 lb/in.^{2}	-	ASTM D-747 (Du Pont)
	-20°C	4300 lb/in.^{2}	-	ASTM D-747 (Du Pont)
Hardness	Shore A, 10s	65-73	76-79	ASTM D-2240 (Du Pont; Springborn)
	Shore D, 10s	24	-	ASTM D-2240 (Du Pont)
Vinyl Acetate Content		33 wt %	33 wt %	Du Pont technical bulletins
Density, g/cm^3	23°C	0.957*	0.920**	Du Pont*/JPL** measurements
Refractive Index, n_d	25°C	1.482*	1.482**	Du Pont*/Springborn** measurements
Dielectric Strength, V/mil	25°C	-	620	Spectrolab measurement
	25°C		500	Springborn measurement
Specific Heat, W-s/g-°C		-	2.09	Spectrolab measurement
Thermal Conductivity, W-mil/ft^2-°C		-	9 x 10^2	Spectrolab measurement
Infra-Red Emissivity	25°C	-	0.88	JPL measurement
Thermal Expansion	Below T_g(-43°C)	1.0 x 10^{-4} °C^{-1}	0.9 x 10^{-4} °C^{-1}	JPL measurement
	-43°C to +10°C	-	2.0 x 10^{-4} °C^{-1}	JPL measurement
	Above +10°C	-	4.0 x 10^{-4} °C^{-1}	JPL measurement

[a]Sources: Property measurements made at Springborn Laboratories under FSA Contract No. 954527
Property measurements made at Spectrolab Inc. under FSA Contract No. 955567
Property measurements made at the JPL's analytical test facilities
Various Du Pont Technical Bulletins on Elvax resins
Du Pont Technical Bulletin "Elvax 150 Resin as a Solar Photovoltaic Module Pottant, Technical Guide," Polymer Products Department, Technical Services Laboratory, Wilmington, Delaware (June 1982).

[b]Initial slope of stress-strain curve

*, **: For each, refer to the Remarks column

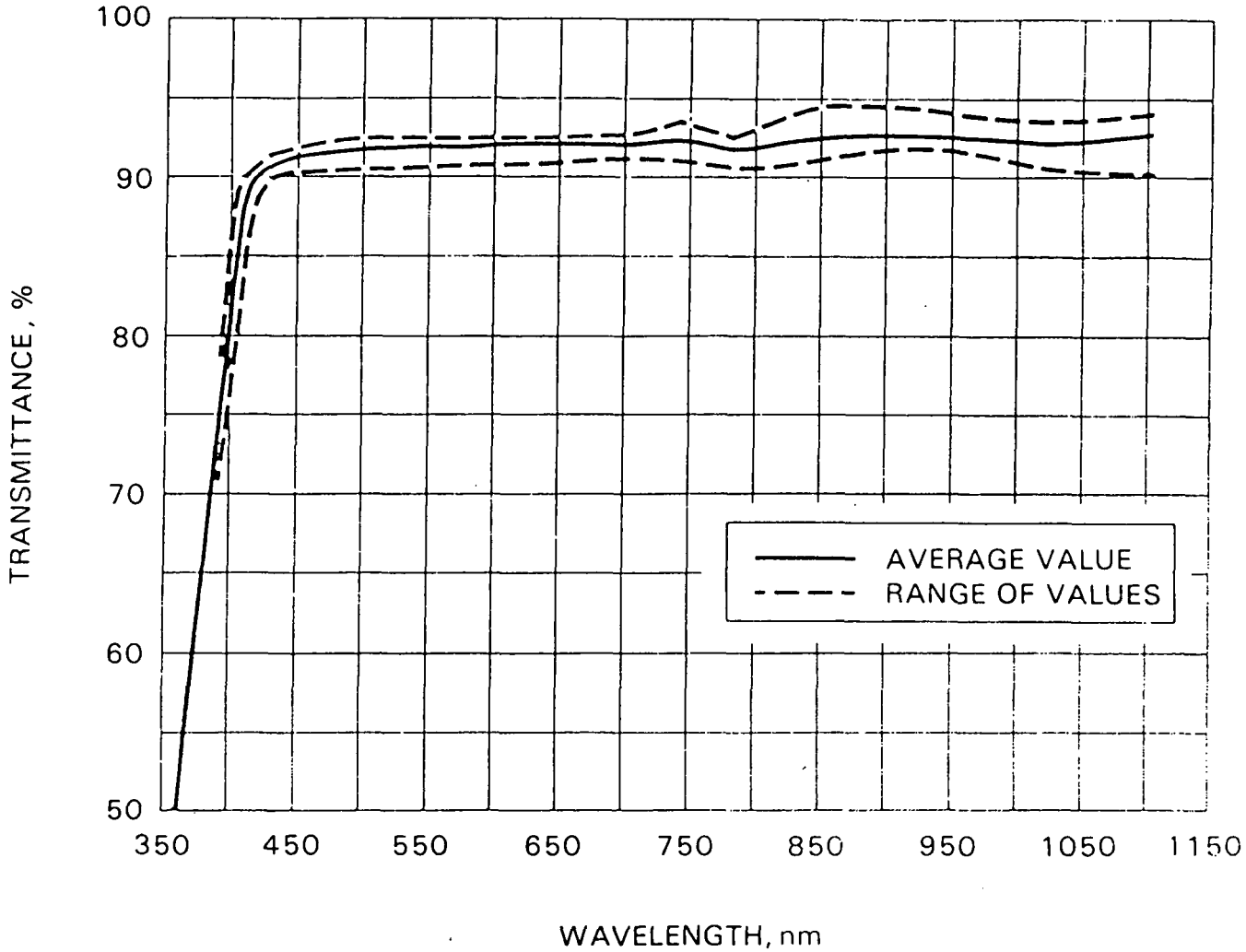

Figure 2. Average Solar Transmittance of 18-mil-Thick Cured EVA A-9918 Film (390-1105 nm)

3. Water Absorption

The equilibrium absorbed-water content of A-9918 EVA has been measured (Reference 3) over the temperature range 20°C to 80°C. The test consisted of suspending specimens of A-9918 EVA over distilled water in sealed jars, and then placing one sealed jar each in five ovens stabilized at 20°C, 50°C, 60°C, 70°C and 80°C. This establishes a relative humidity (RH) of 100% at each temperature. Each A-9918 EVA specimen was initially dried to reference weight in vacuum, and after mounting in the jars, was periodically reweighed until an equilibrium weight was established.

The equilibrium absorbed-water content of the A-9918 EVA, in milligrams of absorbed water per gram of dry EVA (mg/g), is given in Table 4 for each of the five test temperatures. Included in the table is the vapor pressure V_p of water at each of the five temperatures, in units of mm Hg, and the equilibrium absorbed-water content in wt %. The data in Table 3 are sufficient to develop a general expression for the equilibrium quantity of

Table 4. Equilibrium Absorbed-Water Content in A-9918 EVA

Temperature T, °C	Absorbed-Water Content mg/g[a]	Absorbed-Water Content wt %	Saturation Water Vapor Pressure V_p, mm Hg
20	2.5	0.25	17.535
50	3.9	0.39	92.51
60	4.4	0.44	149.38
70	4.9	0.49	233.7
80	5.4	0.54	355.1

[a]Milligrams of absorbed water per gram of dry weight.

absorbed water in A-9918 EVA as a function of relative humidity and temperature. The derivation of this expression follows:

The equilibrium absorbed-water content of hygroscopic materials such as EVA usually obeys the simple expression

$$W = K(T) \cdot V \tag{1}$$

where

W is the absorbed water content in milligrams of water per gram dry weight, mg/g

V is the partial pressure of water vapor in the atmosphere, mm Hg

and K(T) is the absorption isotherm, which is a function of temperature T(°K) only, in (mg/(g)(mm Hg).

The relationship for K(T) as a function of temperature T is Arrhenius in form:

$$K(T) = K_0 \exp\left(\frac{E_1}{RT}\right) \tag{2}$$

where

K_0 is a constant to be determined

E_1 is an activation energy, cal/(°K)(g mol)

R is a constant value = 1.987 for the above units of E_1.

RH at constant temperature T is the ratio of the partial pressure of atmospheric water vapor V to the saturation water vapor pressure V_p at T.

V_p is a function of T, and its relationship also is Arrhenius in form:

$$V_p(T) = V_0 \exp\left(\frac{-E_2}{RT}\right) \tag{3}$$

where V_0, E_2, and R have the same meaning as given for K(T).

Therefore relative humidity in percentage is given by

$$RH = 100 \cdot V/V_p(T) \tag{4}$$

Solving for V yields

$$V = (RH) \cdot V_p(T)/100 \tag{5}$$

Equations 2, 3, and 5 can now be substituted into Equation 1 to yield an expression for W as a function of RH and T:

$$W(RH, T) = (RH) \cdot K_0 \cdot V_0 \cdot \exp\left(\frac{E_1 - E_2}{RT}\right) \tag{6}$$

It is convenient to define $C_0 = K_0 \times V_0$ and $E = E_1 - E_2$, and to use the connective relationship between T in ^{o}K and t in ^{o}C: $T = t + 273.16$. Substituting these into Equation 6 yields the final expression for W as a function of RH in percentage, and t in ^{o}C.

$$W(RH, t) = C_0 \cdot RH \cdot \exp\left(\frac{E}{R(t + 273.16)}\right) \cdot 10^{-2} \tag{7}$$

Using the data in Table 2, the two constants in Equation 7, C_0 and E, can be solved for by a least-squares technique, to arrive at a general expression for the absorbed-water content in EVA as a function of relative humidity and temperature. The resultant expression is

$$W(RH, t) = 2.55 \cdot RH \cdot \exp\left(\frac{-2690}{R(t + 273.16)}\right) \tag{8}$$

4. Experimental EVA Aging Studies

The aging behavior of Elvax 150 and cured A-9918 EVA are being studied at Springborn Laboratories and at JPL. A recent JPL publication (Reference 2) described their separate aging programs and results in detail, and then combined the findings to produce an evolving picture of their aging behavior and an assessment of the materials' service-life potential in array and rooftop-module applications.

A summary of EVA aging, emerging from the combined studies, follows:

Elvax 150 can be degraded by UV photooxidation, thermal oxidation, and by purely thermal decomposition of the acetate groups to acetic acid (in order of decreasing severity), and as protection against each in order is provided, the life and associated peak service temperature of EVA encapsulant may be extended.

Fundamental analysis of Elvax 150 suggests that the UV wavelengths deleterious to this material, and necessary for UV photooxidation, are those shorter than 360 nm. Isolation of Elvax 150 from these UV wavelengths, with UV-filtering outer covers and/or compounding additives such as Cyasorb UV-531, stops UV photooxidation and reduces the aging characteristics of Elvax 150 to thermal effects. This basic and very simple concept was established as a fundamental module design philosophy, and no problem with this concept has been identified in the experimental aging results.

Testing of EVA samples exposed in UV chambers at 55°C included the following combinations:

(1) Elvax 150 with no protection, either additives or UV-screening film overlays.

(2) Elvax 150 with a UV-screening film overlay, but with no antioxidant or UV-absorbing additives.

(3) Fully compounded and cured A-9918 EVA, with an antioxidant and an UV-absorbing additive, but with no UV-screening film overlay.

Elvax 150 sample 1 with no protection yellowed visibly and degraded within 1000 h of exposure; samples 2 and 3, with UV protection as indicated, have survived 20,000 to 30,000 h of exposure with no degrading incidences. Accepting that the UV protection for the latter two samples acted to isolate or protect them from deleterious UV wavelengths, then their aging at 55°C was thermal aging only; and as no aging effects were detected in these two samples, with or without an antioxidant, these tests indicate strongly that Elvax 150 at 55°C is either naturally resistant to thermal oxidation, or undergoes negligibly slow thermal oxidation.

If it can be assumed that a module with Elvax 150 as a pottant provides the necessary UV protection, and if it can be assumed that such a module may be at or near a daily array peaking temperature of 55°C for about 5 h each day, then 20,000 h to 30,000 h of accumulated thermal aging at 55°C corresponds to 11 to 16 years of potential outdoor service. For module applications with daytime peaking temperatures near 55°C, it appears that the life of the EVA encapsulant is related more to the life of the UV protection schemes and less to either the thermal behavior of the EVA or thermal protection schemes (e.g., antioxidants).

The potential for long service life of EVA in modules at rooftop temperatures (e.g., 85°C) looks encouraging, but lifetime predictions would be premature. As at 55°C, permanent UV protection is a must. After that, it is not clearly established which of the thermally driven processes is most critical. These processes would include the basic thermal oxidation properties of the Elvax 150, thermal behavior of antioxidants and the associated

temperature dependence of their protective induction periods, and the temperature dependence of any physical loss and depletion of the protective compounding additives themselves, such as the UV and thermal stabilization additives.

With reference to the last item, a program to identify physical-loss mechanisms of the EVA protective additives has been initiated. The first activity of this program is intended to assess the high-temperature volatility of all of these materials. A preliminary experiment with Cyasorb UV-531 at 90°C has been carried out (Reference 4). For this experiment, 20 g of Cyasorb UV-531 in a 3-in.-dia aluminum dish was put into an air-circulated oven set at 90°C, and the weight of the material was measured periodically. The weight loss data are given in Table 5. This experiment also included an evaluation of the barrier properties of Acrylar and Tedlar plastic films in retarding or stopping the volatile loss of Cyasorb UV-531. Standard 3-in.-dia aluminum perm-cups containing 20 g each of Cyasorb UV-531 were covered with the plastic films. The perm-cups are equipped with a perimeter gasket and clamp fixture to seal the edges against direct leakage. Data for the volatile weight loss through the Acrylar and Tedlar films also appear in Table 5.

Table 5. Volatile Loss of Cyasorb UV-531 at 90°C

	Weight Loss, %		
Days	Tedlar 100BG30UT	Acrylar X-22417	Control
3	0.5	0.5	0.45
7	0.7	0.65	0.75
10	0.7	0.71	0.80
14	0.75	0.77	1.00
18	0.75	0.77	1.00
22	0.75	0.81	1.11
26[a]	0.71	0.68	1.06
30	0.86	0.83	1.25
34	0.91	0.86	1.25
38	0.89	0.88	1.36

[a]The gain in weight at this point coincided with a change in ovens; the cause is not known.

In all three experiments, a more volatile but unknown component or components accounting for about 0.5 wt % of the sample was rapidly boiled off within the first three days, and thereafter the evaporative weight-loss behavior became essentially linear with time. The steady-state rate of loss of Cyasorb UV-531 from the uncovered control cup averaged about 0.14 wt % per week, and about 0.048 wt % per week from the covered cups. These preliminary data demonstrated that Cyasorb UV-531 is volatile at 90°C, but at a very low rate, and that the UV filtering plastic films would slow but would not stop migration and volatile loss of Cyasorb UV-531.

5. Advanced EVA Studies

The available evaluation-ready EVA (A-9918) has been received favorably by the industry. However, its status is still considered to be experimental. To advance EVA toward application readiness, several developmental tasks to improve on quality and durability remain to be completed:

(1) Faster processing, primarily in the cure schedule, which involves a reduction in cure time and temperature; the minimum cure temperature will be dictated by the requirement that the curing system must not become active during film extrusion.

(2) Optimization of the UV-stabilization additives and achievement of resistance against physical loss; the present additives were selected based on literature citation and industrial experience with polymers similar to EVA.

(3) Identification of the peak-service temperature allowed for EVA in a module application, to ensure 20-year life.

(4) Industrial evaluation of the desirability of a self-priming EVA, recognizing the possibility of an additional cost component (cost-benefit-performance tradeoff).

(5) Upgrading the flammability rating of modules fabricated with EVA.

Briefly described herein are some of the early considerations and/or experimental trends relative to 1, 2 and 5. Experimental task 4 is described in some detail in a recently published JPL publication (Reference 5). Task 3 above will be a finding from ongoing acceleration and outdoor aging experiments.

a. Curing-Agent Studies. These studies are intended to identify alternative peroxide curing agents that would reduce cure times and temperatures, as compared with Lupersol 101, to realize a faster lamination cycle at lower temperatures for higher-volume fabrication operations. In addition, there appear to be room-temperature shelf-life limitations associated with the use of Lupersol 101. It has been observed that A-9918 EVA slowly loses its ability to cure if it is stored as unrolled cut sheet. This tendency to lose curability has also been observed for the outer layer of rolled EVA. The time in which this behavior manifests itself can be a few days to several weeks. It is speculated that this behavior may be a result of a gradual volatile loss of the Lupersol 101, or possibly also from rapid

decomposition of the Lupersol 101 resulting from exposure to short-wavelength UV light (<360 nm), which may be generated by room lighting. Occasionally a faint yellow color is observed in uncured A-9918 EVA film that is exposed to room lighting, as observed in the EVA aging studies, which may be associated with the decomposition of the Lupersol 101. Note: The shelf life of A-9918 EVA can be greatly extended by use of protective packaging that acts to stop or limit volatile loss of the Lupersol 101, and by isolation from direct exposure to room lighting.)

Three other peroxide curing agents, all available from the Lucidol Division of the Pennwalt Corp., Buffalo, NY, are being investigated. Their commercial designations are:

(1) Lupersol 99.

(2) Lupersol 331-80B.

(3) Lupersol TBEC.

These agents were substituted for Lupersol 101 in A-9918 EVA and were used at the same concentration of 1.5 phr as used for the Lupersol 101. The modified A-9918 EVA containing these peroxide curing agents was cured at various combinations of time and temperature, and the efficiencies of cure were monitored by measurement of the resultant gel content of the cured EVA.

The cure data for these three peroxide curing agents, with Lupersol 101 cure data for comparison, are given in Table 6. All three of the other peroxides are more efficient than Lupersol 101, resulting in faster cures at lower temperatures, which achieve or exceed the minimum required gel content of 65 to 70 wt % in the cured EVA. These results indicate that, compared with Lupersol 101 cure, one of the new peroxides may be capable of equivalent cure in 1/3 to 1/10 the time, depending on the temperature selected. A high degree of cure at a lower temperature is desirable because of energy savings and reduced time required for heat transfer during lamination. For example, the recommended cure condition for A-9918 EVA with Lupersol 101 is 10 to 15 min at 150°C, to achieve the minimum required gel content. This same level of gel content can be achieved in 10 to 15 min at 120°C with Lupersol 331-80B, or with any of the three alternative peroxides cited above, in 5 min or less at 150°C.

A guideline for selecting peroxide curing agents as alternatives to Lupersol 101 is to recognize that the lowest temperature allowable for EVA cure is dictated by the requirement that no cure of the compounded EVA occur during film extrusion. As the temperature of the EVA within the barrel of the film extruder can be at a temperature of 115°C for a few minutes, the use of a curing agent that would result in measurable cure at this temperature is to be avoided. A safety margin of about 5°C above the peak extrusion temperature establishes an allowable lower-bound cure temperature of about 120°C. Thus, of the three peroxides evaluated to date, and solely on the basis of cure data, Lupersol 331-80B would appear to be the choice as an alternative to Lupersol 101.

However, if it is assumed that one of the shelf-life limitations of A-9918 EVA formulated with Lupersol 101 is related to volatile loss of this peroxide, then an alternative peroxide should also be less volatile compared

Table 6. Cure of A-9918 EVA at Various Times and Temperatures with Four Different Peroxide Curing Agents as Monitored by Gel Content in wt %

Lupersol 101

Cure Time, min	Degree of Cure, % Gel				
	130°C	140°C	150°C	160°C	170°C
1			0	2.1	28.8
2		1.0	4.1	29.5	74.2
5		11.8	21.1	73.0	81.2
10	1.0	23.5	63.2	82.6	92.7
15	2.3	59.3	88.3		
30	3.4	68.2			
60	32.1	80.6			

Lupersol 99

Cure Time, min	Degree of Cure, % Gel					
	110°C	120°C	130°C	140°C	150°C	160°C
2					low	75.2
5				low	70.7	79.0
10	0	low	low	72.2	77.7	79.9
15	0	8.1	69.5	74.9	78.4	
30	low	76.0	82.1	77.7	79.9	

Table 6. Cure of A-9918 EVA at Various Times and Temperatures with Four Different Peroxide Curing Agents as Monitored by Gel Content in wt % (Cont'd)

Lupersol 331-80B

Cure Time, min	Degree of Cure, % Gel					
	110°C	120°C	130°C	140°C	150°C	160°C
2					79.5	84.5
5				88.8	86.9	88.7
10	0	68.2	84.2	89.3	88.0	87.6
15	0	80.4	87.4	92.4	88.9	
30	0	78.5	92.0	89.9		

Lupersol TBEC

Cure Time, min	Degree of Cure, % Gel			
	120°C	130°C	140°C	150°C
2	0	0	73.4	81.5
5	0	60.3	83.7	88.6
10	0	75.0	88.2	91.6
15	0	85.0	90.2	93.5
20	60	78.3	92.7	93.0
30		82.7	92.2	92.6

with Lupersol 101. All four of these Lupersol peroxides are liquids, but their boiling points cannot be measured because chemical decomposition occurs before any evidence of boiling is observed. Furthermore, vapor pressure at room temperature has not been measured, nor found in published literature. However, the flash point of each of these four peroxide liquids is given in Pennwalt technical sales literature for these products; these flash points are listed in Table 7. If it can be assumed that comparison of flash points provides a relative measure of volatility, then Lupersol 331-80B is the most volatile of the four, and Lupersol TBEC is the least volatile. Comparing the

Table 7. Flash Points of the Four Lupersol Peroxide Curing Agents

Peroxide	Flash Point (Volatility)
Lupersol 101	43°C
Lupersol 331-80B	40°C
Lupersol 99	77°C
Lupersol TBEC	101°C

flash points of Lupersol 101 and Lupersol 331-80B suggest comparable volatility, and thus, although substitution of Lupersol 331-80B for Lupersol 101 may result in faster curing at lower temperatures, improvements in shelf life may not be realized; it may even be worse. Therefore, based on volatility behavior suggested by flash-point data, Lupersol TBEC becomes a preferred alternative to Lupersol 101.

A comparison of the chemistry involved in the peroxide curing of EVA with Lupersol 101 and Lupersol TBEC is provided by a laboratory test (Reference 4) that involved curing a series of EVA resins varying in vinyl acetate content. Included in the series was a pure polyethylene, which for the purpose of this test was considered to be an EVA with zero wt % vinyl acetate. The cure results, as monitored by gel content, are shown in Table 8.

Both peroxides cured all of the EVA resins, but Lupersol TBEC was more effective in achieving a greater efficiency of cure (higher gel content). Furthermore, Lupersol TBEC was effective in crosslinking the pure polyethylene sample, but Lupersol 101 was not. As shown in Figure 1, the chemical structure of EVA consists of a separate block of pure polyethylene, and a separate block of an ethylene-vinyl acetate copolymer. Since Lupersol 101 did not cure the polyethylene, these cure results suggest that EVA curing with Lupersol 101 may involve only the ethylene-vinyl acetate block, whereas Lupersol TBEC curing may more effectively encompass all of the EVA block structure. This may explain the greater cure efficiency of Lupersol TBEC compared with that of Lupersol 101.

Continuing work with alternative curing agents and others yet to be identified will involve vapor-pressure measurements, shelf-life characteristics, and effects, if any, of the alternative curing agents on module fabricability, other compounding additives, efficiency and performance of adhesives and primers developed for EVA, and weather aging of EVA-encapsulated modules.

Table 8. Peroxide Curing[a] of Polyethylene and EVA Resins With Lupersol 101 and Lupersol TBEC

Resin	Vinyl Acetate, wt. %	Gel Content, %	
		101	TBEC
Elvax 150	33	75	95
Elvax 450	18	62	95
Elvax 750	9	61	90
Polyethylene	0	0	87

[a]All polymers cured with 1.5 parts peroxide per hundred parts of resin at 150°C for 20 minutes.

b. UV-Absorbing Additives. The EVA aging studies strongly indicate that UV protection of the EVA is essentially assured as long as the Cyasorb UV-531 UV-absorbing additive remains physically within the EVA. However, these same aging studies indicate a tendency toward gradual physical loss of this additive, presumably because of volatility, at elevated temperatures.

A major premise for the durability of low-cost, UV-sensitive pottants is that protection will be ensured by UV filtering through the glass superstrate, or through UV-screening plastic-film front covers, and that any UV that does pass through the filters will be absorbed harmlessly within the pottant itself by uniformly dispersed UV screening agents. Loss of UV protection for the pottant either by chemical consumption of the screening agents or by physical loss from bleeding, migration, rainwater leaching, etc., could limit module longevity.

Thus a program to identify and evaluate chemically attachable UV-screening agents has become a major activity within the last year (Reference 3). An experimental, chemically attachable UV-screening agent, developed by American Cyanamid Co., was made available to FSA for trial evaluation in EVA. The designation of this experimental additive is UV-2098.

UV-2098 was substituted for Cyasorb UV-531 in EVA, and after curing of the EVA, less than 5% of the incorporated UV-2098 could be extracted from the EVA. Under identical solvent extraction conditions, Cyasorb UV-531 is readily and easily extracted from EVA.

Cured EVA samples with chemically attached UV-2098 have been exposed to continuous UV at 55°C for more than 8000 hours in RS/4 test chambers at Springhorn Laboratories. There have been no changes in optical, mechanical, or physical properties, nor any evidence that the UV-2098 is becoming detached from the EVA. The test results are encouraging, and testing will continue.

c. Flammability. Concerns about the fire safety of solar modules encapsulated with EVA were presented in a recent report (Development of Photovoltaic Array and Module Safety Requirements, Underwriters Laboratories Report No. DOE/JPL 955392-1). These concerns resulted from the observation that EVA appears to become fluid under fire conditions, and then runs out of the module structure, possibly igniting other structures. Initial experiments were performed to assess the relative flammability of module construction components and also to test some trial flame-retardant EVA formulations. The test employed was the UL-94 vertical burn test, and was run on the following materials:

Specimens required: Five bars of each formulation, 5 in. long, 0.5 in. wide, 60 mils thick, prepared from the following formulations:

(1) EVA-9918, cured.

(2) EMA 13439, cured.

(3) PU-2591, cured.

(4) BA-13870, cured.

(5) PVB Saflex PT-10.

(6) RTV-615, cured.

(7) Elvax-150, uncured.

(8) EVA-9918, cured with four layers of Craneglas molded in.

(9) EPDM gasket materials.

The flame-retardant EVA formulations listed in Table 9, which can also be used as a flame-retardant reflective white layer behind the cells, were prepared. The formulations were prepared by differential milling and then cured into 60-mil-thick plaques for testing.

For a rating to be assigned to a material, it must not show self-sustained burning longer than 30 seconds or produce flaming drops of resin that ignite a pile of cotton beneath the test specimen. Of the materials tested, only one may be rated by this test. The PU-2591 was the only specimen that showed self-sustained burning of less than 30 seconds and in sequential ignitions; it extinguished within 1 second. The material did drip, however, and also ignited the cotton beneath the specimen. The flame-retardant EVA formulations did show some improvement, the best being B (see Table 9). However, they were still too flammable to be within the range of rating. An important observation was made during these tests, however. The only specimen that did not drip and ignite the cotton was the EVA pottant that had been cured with four layers of Craneglas. Although no improvement was noticed in the flammability of the combination, the problem of flaming drips was totally eliminated. It is possible that this simple and inexpensive modification may prevent drip from modules being fire tested for rooftop acceptability. Efforts to develop better flame-retardant EVA formulations will continue.

Table 9. Candidate Flame-Retardant EVA Formulations

	A	B	C	D	E	F
Elvax 150	100	100	100	100	100	100
TBEC	1.5	1.5	1.5	1.5	1.5	1.5
Antimony Oxide (Harshaw)	2.5	-	-	-	-	1.5
Zinc Borate (Firebrake-ZB)	-	2.5	-	-	-	-
Decarbromodiphenyloxide (Dow-FR-300BA)	5.0	5.0	-	-	-	3
Aluminum Trihydrate (Alcoa-Hydral 705)	-	-	30	20	-	10
Chlorez-700 (chlorinated paraffin oil)	-	-	-	15	-	-
Pliovic WO-2 (PVC resin dispersion)	-	-	-	-	30	10
Zinc Oxide (Kadox 15, NJZ)	5	5	5	5	5	5

B. THERMAL-OPTICAL MODELING

An extensive and greatly detailed thermal-optical model computer program has been developed (Reference 6). The model, key findings and conclusions drawn therefrom are described in an earlier report (Reference 7). The purpose of the model is to assess the effects of encapsulation materials, substitution of encapsulation materials, and encapsulation design options on module operating temperature. The computer model was used this year to investigate the basis for, and the significance of, the experimentally observed near-linear dependence between module operating temperature and solar insolation (References 8 and 9).

Figures 3 through 6 are reproduced from Reference 9, and are plots of $T_{CELL} - T_{AIR}$ (^{o}C) versus insolation in mW/cm^2 for four Block I modules mounted outdoors at JPL in Pasadena, California. Experimental observations reveal that the temperature difference between the solar cell and ambient air, $T_{CELL} - T_{AIR}$, is largely independent of ambient air temperature, and is essentially linearly proportional to the solar insolation level S. What appears as data scatter around the straight line has been related to local fluctuations in ground wind velocities around the modules (Reference 9).

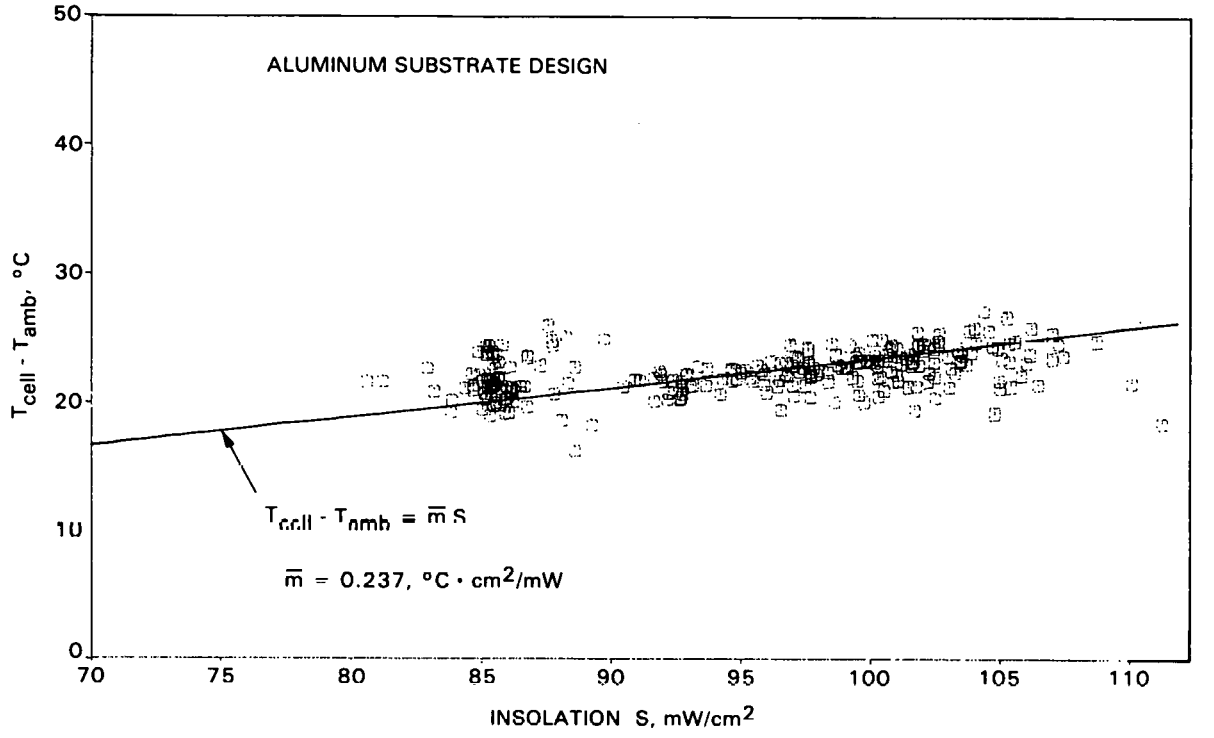

Figure 3. ΔT versus Insolation for Sensor Technology (Now Photowatt International, Inc.) Block I Module

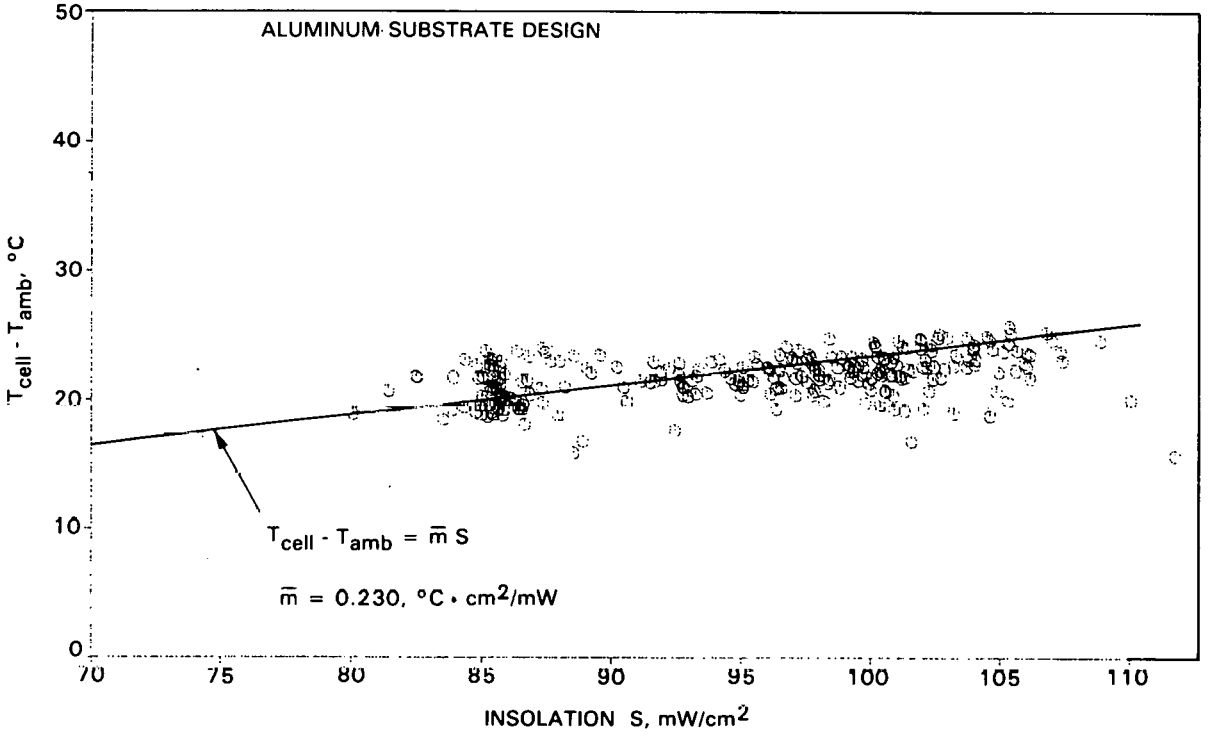

Figure 4. ΔT versus Insolation for Spectrolab, Inc., Block I Module

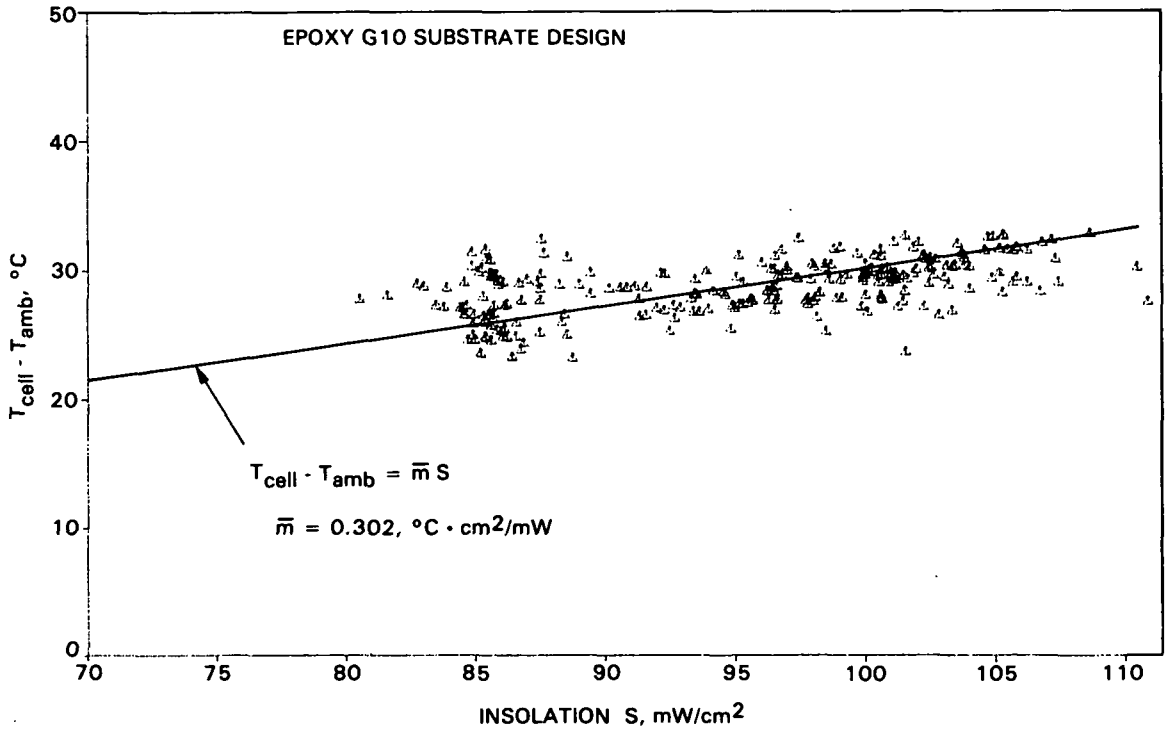

Figure 5. ΔT versus Insolation for Solarex Corp. Block I Module

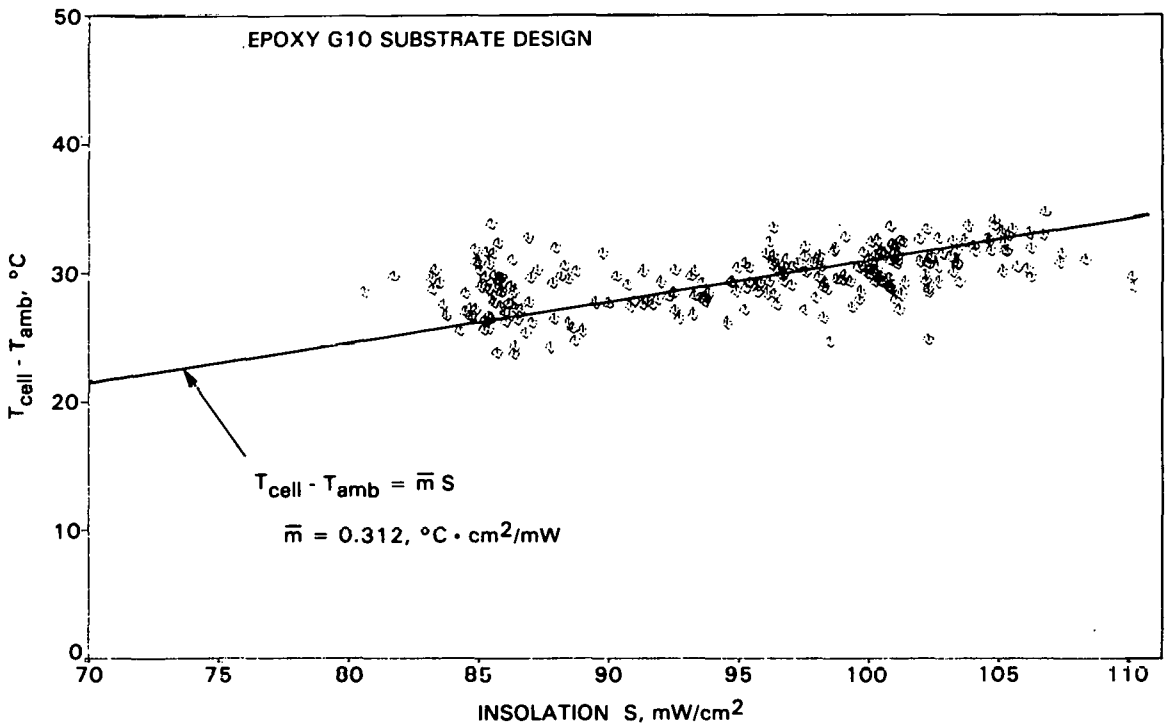

Figure 6. ΔT versus Insolation for Solar Power Corp. Block I Module

Operations with the thermal-optical computer model ultimately resulted in a key finding: those features of a photovoltaic module that are involved in the absorption and conversion to heat of solar insolation can be mathematically treated independently of those features of a photovoltaic module that relate to heat dissipation (Reference 6). Accordingly, a photovoltaic module can be viewed as a thick slab of material layers having as a core a simple heat generator, such as resistance wires. This heat-dissipation model is illustrated schematically in an outdoor environment in Figure 7. Heat, Q_c, generated by the core, conducts thermally through the sun-side and back-side material layers to the front and back surfaces, and then dissipates from the surfaces by radiation, and by both free convection and wind convection. For fixed environmental conditions and thermal properties of the material layers and surfaces, an equilibrium relationship between Q_c and the core temperature T_c can be found.

Another related aspect of the thermal-optical model was investigated this year. The computer program discussed above is not readily available to photovoltaic module designers for analysis of their systems or design options. It was therefore of interest to determine if a simple set of expressions for thermal radiation, conduction, and free convection and wind convection could be used for the heat dissipation model, with negligible error. A JPL publication (Reference 9) titled "An Investigation of the Effects of Wind Cooling on Photovoltaic Modules," by L. Wen, set forth heat-transfer equations for radiation and convection that he found in References 10 and 11. These equations are reproduced in Table 10. Tables 11 and 12 are reproduced from Reference 1. Table 11 lists thermal resistances and thicknesses of representative encapsulation materials; Table 12 shows total thermal resistivity values

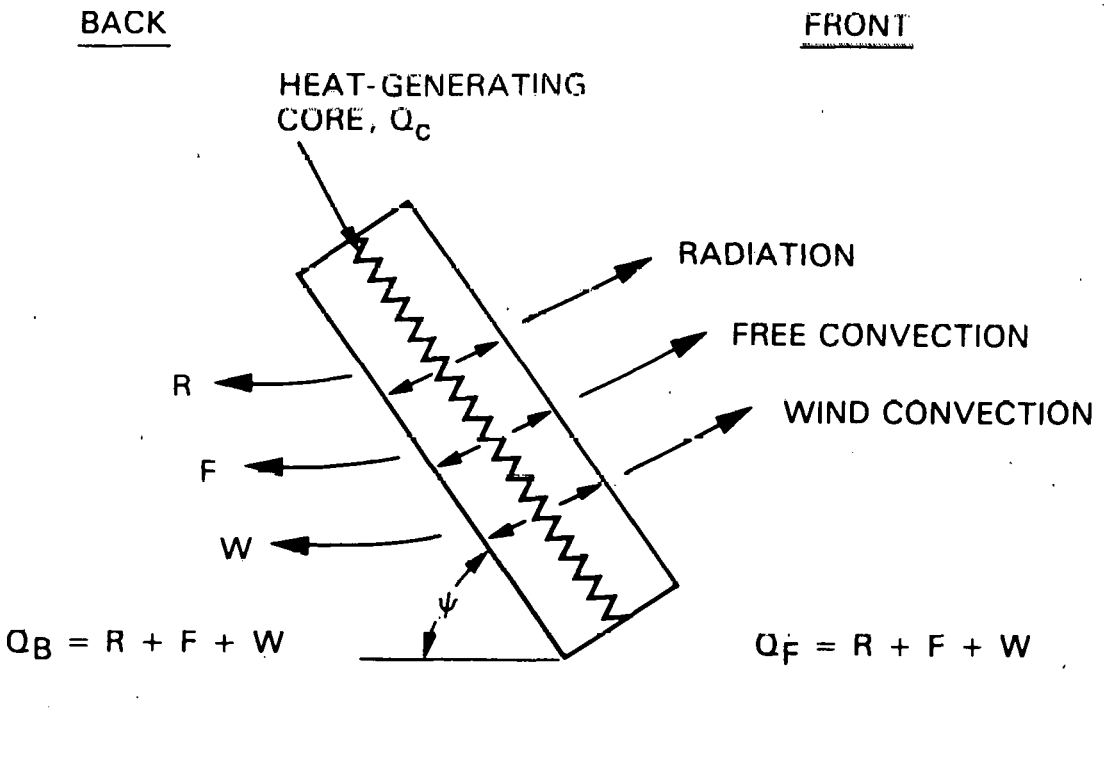

Figure 7. Heat Dissipation Model

Table 10. Heat Transfer Equations for Heat-Dissipation Modeling

Module Sun Side

$Q_{FF} = Q_{FREE\ CONVECTION} = (1.52)\ (\cos\psi)^{1/3}\ (t_F - t_A)^{4/3}\ (W)/(m^2)\ (^oC)$

$Q_{WF} = Q_{WIND\ CONVECTION} = H\ (t_F - t_A)$

$Q_{RF} = Q_{RADIATION} = \epsilon_F \sigma (T_F^{\ 4} - T_{SKY}^{\ 4})$

$Q_{FRONT} = Q_{CONDUCTION} = (t_C - t_F)/\Sigma(L/K)_{FRONT} = Q_{FF} + Q_{WF} + Q_{RF}$

Module Back Side

$Q_{FB} = Q_{FREE\ CONVECTION} = (1.31)\ (\cos\psi)^{1/3}\ (t_B - t_A)^{4/3}\ (W)/(m^2)\ (^oC)$

$Q_{WB} = Q_{WIND\ CONVECTION} = H\ (t_B - t_A)$

$Q_{RB} = Q_{RADIATION} = \epsilon_B\ \epsilon_g \sigma (T_B^{\ 4} - T_A^{\ 4})$

$Q_{BACK} = Q_{CONDUCTION} = (t_C - t_B)/\Sigma(L/K)_{BACK} = Q_{FB} + Q_{WB} + Q_{RB}$

Total Heat Dissipation (Q_c)

$Q_c = Q_{FRONT} + Q_{BACK}$

Terms and Constants

t_F = front-surface temperature, ^oC
t_B = back-surface temperature, ^oC
t_C = core temperature, ^oC
t_A = ambient air temperature, ^oC
σ = Stefan-Boltzman constant, $0.56699 \cdot 10^{-8}$ $mW/cm^2(^oK^4)$
ψ = module tilt angle from horizontal, deg
T_F = front-surface temperature, ^oK
T_B = front-surface temperature, ^oK
T_A = ambient air temperature, ^oK
T_{SKY} = 0.914 T_A, ^oK (Reference 12)
$\Sigma(L/K)_{FRONT}$ = thermal resistance of sun-side encapsulation layers
$\Sigma(L/K)_{BACK}$ = thermal resistance of back-side encapsulation layers
ϵ_F = front-surface emissivity
ϵ_B = back-surface emissivity
ϵ_g = ground emissivity
V = wind velocity, m/s
H = wind convection coefficient, $W/(m^2)\ (^oC)$
(a) $H = 3.8\ V$, $V \leq 5$ m/s
(b) $H = 7.17\ V^{0.78} - 6.0$, $V > 5$ m/s

Table 11. Thermal Resistivities

Material	K, $\frac{\text{Watts-mils}}{\text{ft}^2 - {}^{o}\text{C}}$	Representative Thickness L, mils	Thermal Resistance, L/K
Acrylic film	7×10^2	3	4.3×10^{-3}
Glass	3×10^3	125	41.6×10^{-3}
EVA	9×10^2	10	11.1×10^{-3}
Steel	2×10^5	28	0.14×10^{-3}
Wood (hardboard)	7×10^2	125	178×10^{-3}
Mylar	6×10^2	3	5×10^{-3}
Aluminum foil	7×10^5	2	0.003×10^{-3}
Stainless-steel foil	2×10^5	2	0.01×10^{-3}

Table 12. Thermal-Resistivity Sums for Glass-Superstrate and Wooden-Substrate Module Designs

Module Design	Thermal Resistivity, $\frac{\text{ft}^2 - {}^{o}\text{C}}{\text{watts}}$
Glass, EVA,[a] Mylar	$\Sigma(L/K)_{FRONT} = 52.7 \times 10^{-3}$ $\Sigma(L/K)_{BACK} = 16.1 \times 10^{-3}$
Acrylic, EVA,[a] Wood, Mylar	$\Sigma(L/K)_{FRONT} = 15.4 \times 10^{-3}$ $\Sigma(L/K)_{BACK} = 194.1 \times 10^{-3}$

[a]This example assumes that the EVA layer in front of the cells and the EVA layer behind the cells are each 10 mils thick.

for front-side and back-side material layers of glass-superstrate and wooden-substrate module designs. With fixed environmental conditions, and thermal resistivity values calculated for a specific encapsulation design, the equations in Table 10 can be solved simultaneously for the equilibrium relationship between Q_c and T_c, with negligible error. For this analysis, a value of 0.8 was used for the ground emissivity ϵ_g.

Using the equations in Table 10 and the thermal resistivity values in Table 11, the equilibrium relationship between Q_c and T_c for a 1/8-in.-thick glass-superstrate module was found, and is plotted in Figure 8. Two cases are shown: a field-array installation in which heat dissipation can occur from both the front and back surfaces, and a rooftop installation where heat dissipation can occur from the front side only (i.e., $Q_B = 0$). The fixed environmental conditions are an air temperature T_{AIR} of 20°C, and a wind speed of 1 m/s, both of which are nominal operating cell temperature (NOCT) environmental conditions. The module tilt angle is 34° above horizontal, and the front-side and back-side surface emissitivities are 0.9.

The relationship between T_c and Q_c is nearly linear over the range from 30 to 100 mW/cm^2, suggesting that the experimentally observed linear relationship between $T_{CELL} - T_{AIR}$ and S is a consequence of the heat dissipation property of the photovoltaic module. The average slope of the array installation line is about 0.321 (°C)(cm^2)/(mW), which is of the order of magnitude of the experimental slopes cited in Figures 3 through 6. For the example illustrated in Figure 8, if the glass-superstrate module mounted on an array installation were required to dissipate 70 mW/cm^2 of heat, its equilibrium temperature would be near 47°C. Mounted on a rooftop with no back-side heat dissipation ($Q_B = 0$), its equilibrium temperature to dissipate 70 mW/cm^2 would be near 67°C.

The effect of air temperature on the operating temperature of a glass-superstrate module is shown in Figure 9 for air temperatures of 10°C, 20°C, and 30°C. Figure 9 is plotted as $T_c - T_A$ versus Q_c, for both rooftop and array installation. The difference between the operating temperature and the air temperature is almost independent of the air temperature, as has been observed experimentally.

Figure 10 compares the heat-dissipation behavior of three module designs: a glass-superstrate module, a wooden-substrate module, and a mild-steel-substrate module. The behavior of all three for both rooftop and array installation is virtually the same, reinforcing a previously reported key finding (Reference 7) that heat dissipation from photovoltaic modules is dominated by surface radiation and convection, and to a lesser extent by bulk thermal conduction. However, it is to be noted that the minor differences in operating temperatures and slopes of the lines are primarily regulated by the differences in the thermal resistivities of the encapsulation layers. This shows up in the experimental data of Figures 3 through 6, where the Figure 3 and Figure 4 modules with lower slope values used aluminum pan substrates, and the Figure 5 and Figure 6 modules, with higher slope values, used structural plastic substrates (NEMA G-10 epoxy boards), which have higher thermal resistance than aluminum has.

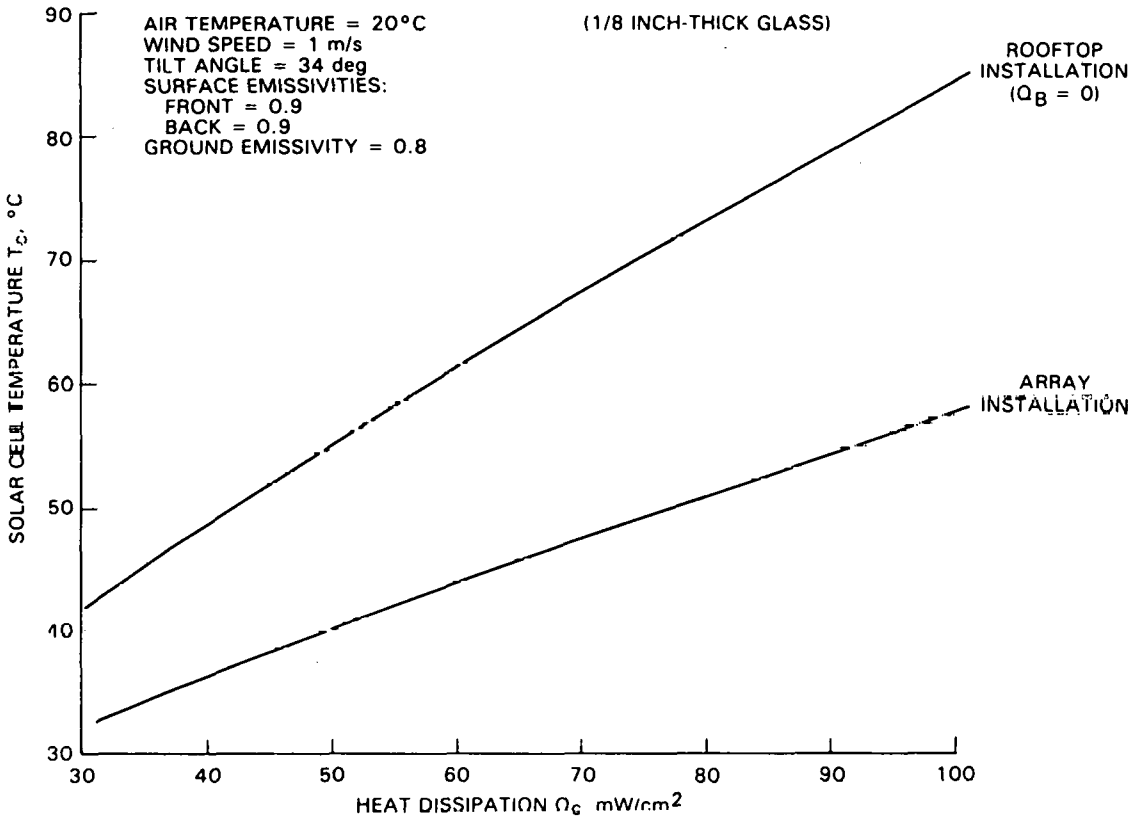

Figure 8. Heat-Dissipation Behavior of a Glass-Superstrate Module

The absorption and conversion to heat of incident sunlight that must be dissipated from a module, Q_c, can be estimated from simple considerations when modules are classified into three distinct absorption types (Figure 9). Simplifying assumptions for all three module types are that sunlight incidence is normal to the module surfaces, and that surface back-reflection losses are 4%. Therefore, 96% of insolation incident on the module enters the module. Further, sunlight is absorbed only by solar cells, and not by any encapsulation materials, including the white background between solar cells, if it exists. In a module with this white background, it is assumed that incident sunlight will be back-scattered, and that one third of the back-scattered sunlight will be absorbed by solar cells, and two thirds will be reflected out of the front surface of the module; therefore, they contribute no heat to the module. If the intercell area is not white, but transparent, it is assumed that all sunlight transmitted through the transparent intercell area passes out through the back side of the module, and contributes no heat to the module. All sunlight absorbed by solar cells is divided between heat to be dissipated (Q_c) and electric power. In modules with less than 100% solar cell area coverage, it is assumed that sunlight absorption is proportional to actual solar-cell area coverage, but that heat dissipation will occur over the full module area. Last, for NOCT estimates, wherein no electric power is taken from the module, it is assumed that all sunlight absorbed by the solar cells is converted to heat, Q_c.

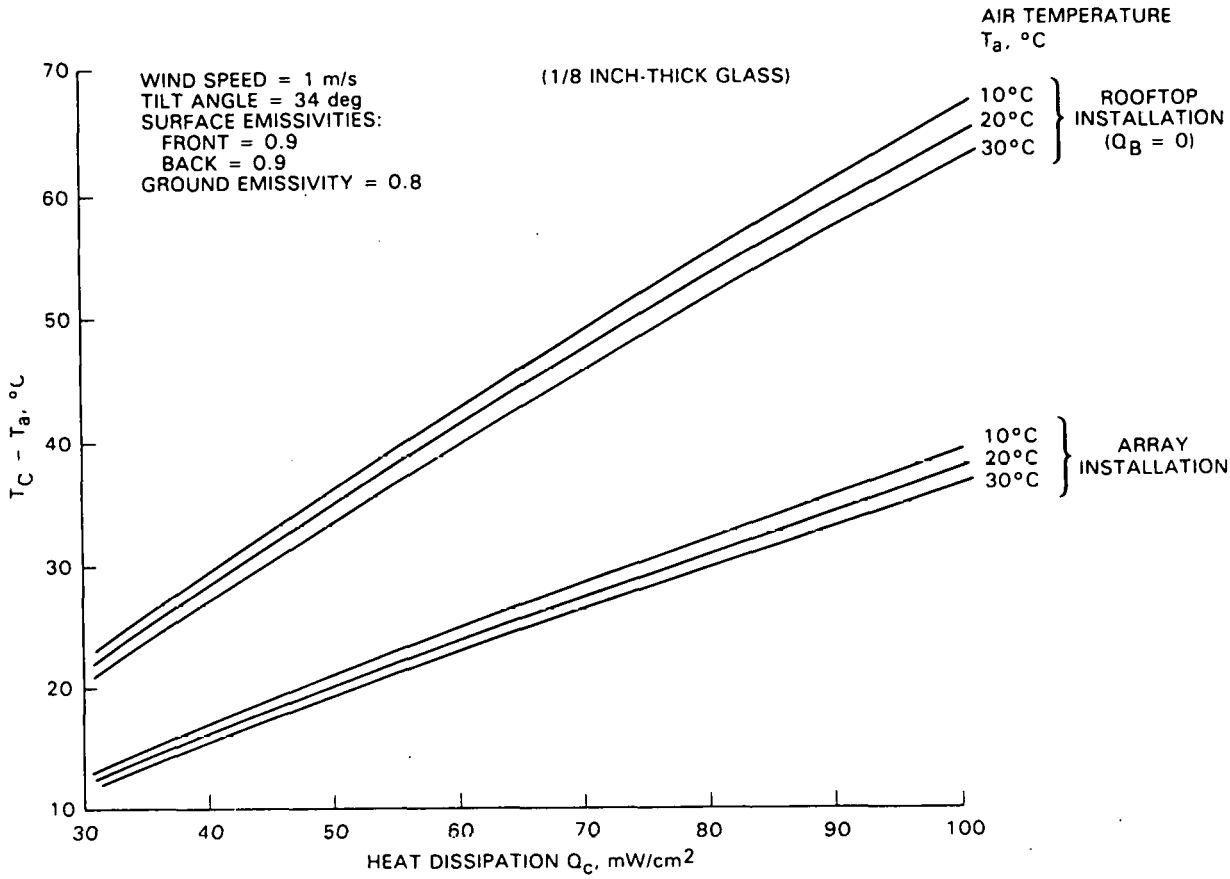

Figure 9. Effect of Air Temperatures (T_A) on the Heat-Dissipation Behavior of a Glass-Superstrate Module

Module Type A in Figure 11 has 100% solar cell area coverage. Hence, Q_c is simply entering insolation minus any electric power output; mathematically,

$$Q_c = (0.96)(S) - \text{electric power} \tag{9}$$

For NOCT estimates, electric power is zero; therefore, $Q_c = (0.96)(S)$.

Module Type B in Figure 11 has partial solar-cell coverage (less than 100%), with transparent intercell spaces. Denoting the fraction of solar-cell area coverage as A, then Q_c is estimated by

$$Q_c = (0.96)(A)(S) - \text{electrical power} \tag{10}$$

It is assumed that all insolation entering the transparent intercell area, 1 - A, passes out of the module with no heat contribution. Again, for NOCT estimates, electric power is zero, and therefore $Q_c = (0.96)(A)(S)$.

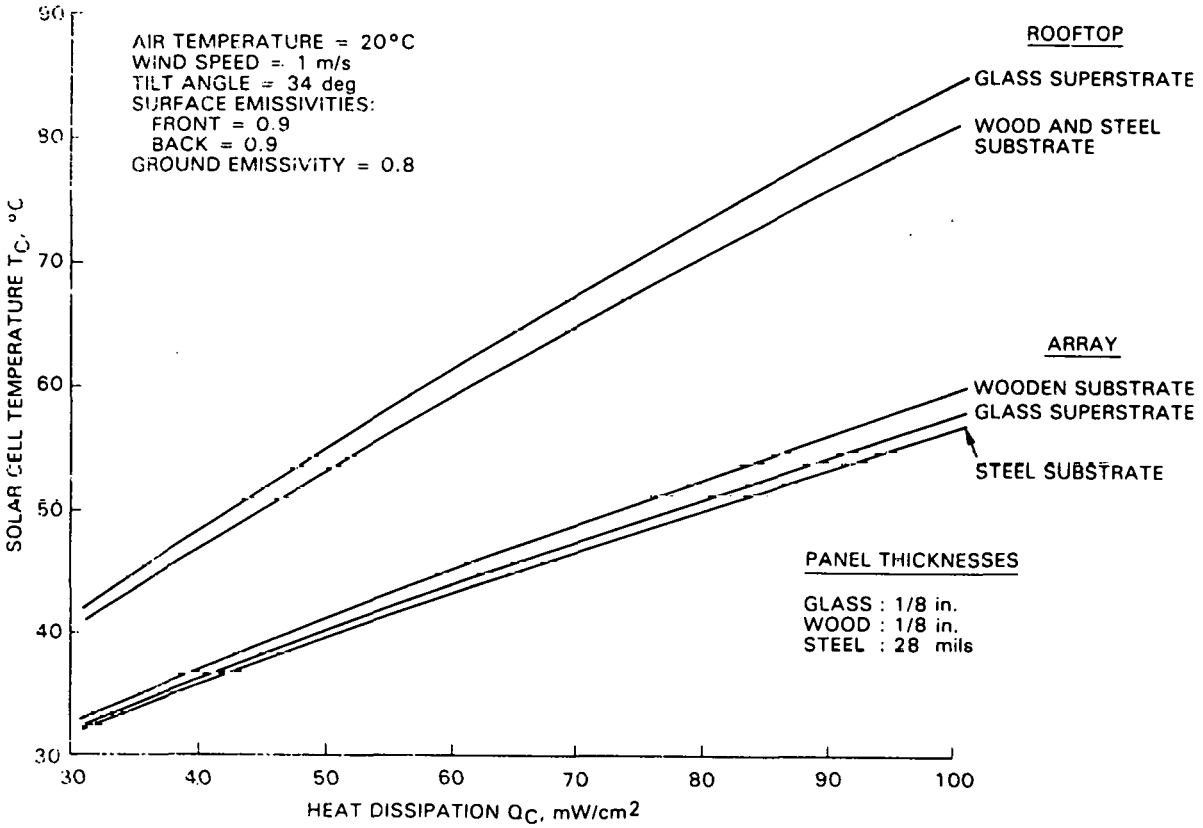

Figure 10. Comparative Heat-Dissipation Behavior of a Glass-Superstrate Module and of a Wood-and-Steel Substrate Module

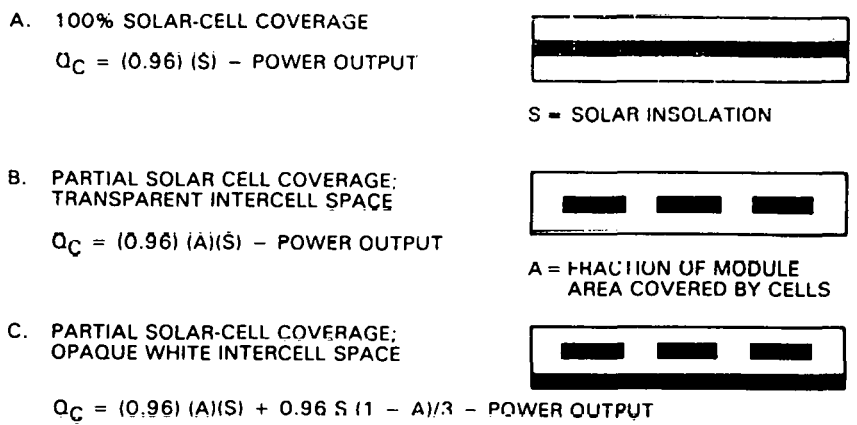

Figure 11. Module Models for Q_c Calculations

Module Type C in Figure 11 has partial solar cell coverage, with a white background in the intercell spaces. For this case, Q_c is estimated:

$$Q_c = (0.96)(A)(S) + (0.96)(1 - A)(S)/3 - \text{electrical power} \qquad (11)$$

The assumption is made that one third of the sunlight incident on the white background is absorbed by the solar cells. Again, for NOCT estimates, electric power is zero, and therefore $Q_c = (0.96)(A)(S) + (0.96)(1 - A)(S)/3$.

NOCT values have been measured experimentally and reported (Reference 13) for a Block II Spectrolab, Inc., module in an array installation and for a Block II Solar Power Corp. module in both array and rooftop installations. The Spectrolab Block II module had a glass superstrate with transparent intercell area (Module Type A); the Solar Power Block II module had a structural plastic substrate with a white background in the intercell area (Module Type C). Both module designs had a solar-cell area coverage A of about 0.7. The experimentally measured NOCT values are given in Table 13.

The NOCT solar insolation level S is 80 mW/cm^2. Therefore, for the Spectrolab Block II module, Q_c is estimated as

$$Q_c = (0.96)(80)(0.7) = 53.7 \text{ mW/cm}^2 \quad (12)$$

Using this value of Q_c and the heat dissipation line for a glass-superstrate module in Figure 10, NOCT is estimated at 42°C. The more extensive thermal-optical model used in the Spectrolab computer program also yields a NOCT in the range of 42°C to 43°C (Reference 6).

For the Solar Power Block II module, Q_c is estimated as

$$Q_c = (0.96)(80)(0.7) + (0.96)(80)(0.3)/3 = 61.4 \text{ mW/cm}^2 \quad (13)$$

No heat dissipation line has been generated for a plastic-substrate module, but inspection of Figure 10 indicates little sensitivity of the T_c/Q_c line to the selection of the load-carrying panel, and since the thermal resistance of plastic substrates would be more closely matched by that of a wooden substrate, the heat dissipation line generated for the wooden substrate is used. Using the above value of Q_c, and the wooden-substrate heat-dissipation line of Figure 10, an array installation NOCT value of 45°C is estimated. The rooftop NOCT value is estimated to be near 60°C, using the same value of Q_c and the wooden-substrate and steel-substrate rooftop heat dissipation line in Figure 10.

The method described herein for estimating module operating temperatures is intended to be a convenient, desktop approach for photovoltaic-module designers assessing their specific encapsulation systems, or encapsulation design options. The heat dissipation curves shown in Figures 8, 9 and 10 were generated with the equations in Table 10, using a Commodore 64 home computer system.

Table 13. Experimental and Predicted NOCT Values for Spectrolab, Inc. and Solar Power Corp. Block II Modules (Reference 12)

Spectrolab	Array Installation			
	Measured	Predicted		
	41°C	42°C		
Solar Power	Array Installation		Rooftop Installation	
	Measured	Predicted	Measured	Predicted
	45°C-46°C	45°C	61.5°C	60°C

C. STRUCTURAL MODELING

1. Introduction

Volume I of this document (References 1 and 14) reported on the development and use of reduced-variable master curves in estimating stresses in encapsulated solar cells, resulting from thermal expansion and wind deflection of PV modules. The structural analysis had two parts: prediction of stress distribution throughout a module when deflected by a 100-mi/h wind (50 lb/ft^2 loading pressure), and prediction of stress distribution throughout a module set up by thermal-expansion differences when a module is heated or cooled over a temperature range ΔT. For both cases, a zero-stress state was assumed to exist throughout the module before deflection or thermal stressing. Also, at that time, the two cases were separately analyzed; the combined action of wind deflection and thermal stressing were not then analyzed.

Details of the module structure that was analyzed were:

(1) Module dimensions: 1.2 m square (4 x 4 ft square).

(2) Solar cells: 10 x 10 cm square x 0.4 mm (4 x 4 in. x 0.015 in. thick).

(3) Spacing between solar cells: 1.3 mm (0.050 in.).

The reduced-variable master curve for thermal stress as then developed is shown in Figure 12. The variable parameters included the thickness and Young's modulus of the pottant, the Young's modulus and thermal-expansion coefficient of the structural panel, and the temperature difference ΔT. A reduced-variable master curve for wind deflection was not yet developed. The master-curve shape was established (Figure 13), but the reduced-variable expressions had not been generated.

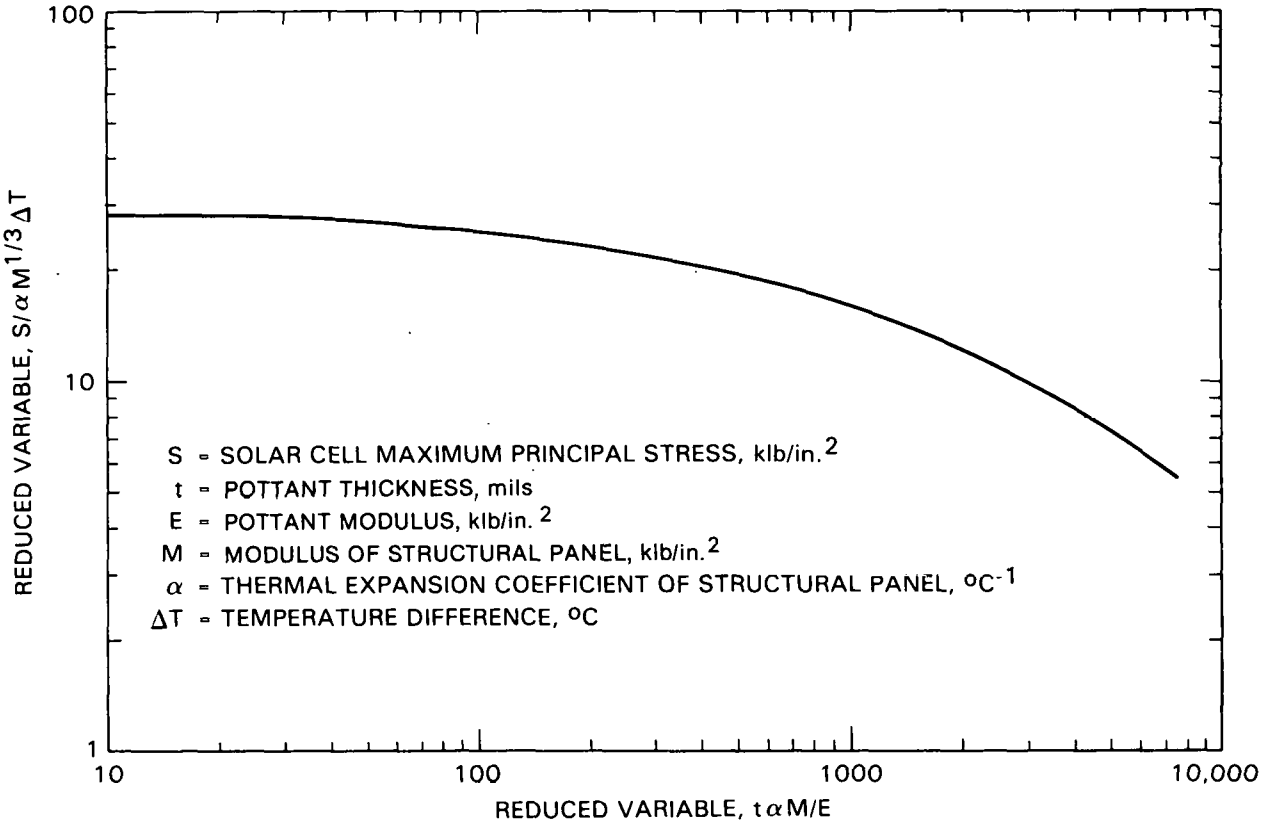

Figure 12. Master Curve for Thermal Stress Analysis (Circa 1982)

Structural modeling during 1983 involved three activities:

(1) Establishing reduced-variable expressions for the wind-deflection master curve.

(2) Expanding the inventory of structural parameters for master-curve analysis.

(3) Initiating an investigation of the combined action of wind deflection and thermal expansion.

Table 14 is a general list of structural parameters under investigation for inclusion in the master-curve reduced-variable expressions. As details of this year's work will be published soon (Reference 6), this section will present a summary version with key findings and conclusions.

2. Master Curves

The expanded master curves as currently developed are shown in Figure 14 for deflection loading and in Figure 15 for thermal loading. The parameters investigated to date for each are listed in the figures. The deflection master curve (Figure 14) contains two curves: Curve A, to be used for pressure loadings up to 10 lb/ft^2, and Curve B, to be used for 50 lb/ft^2.

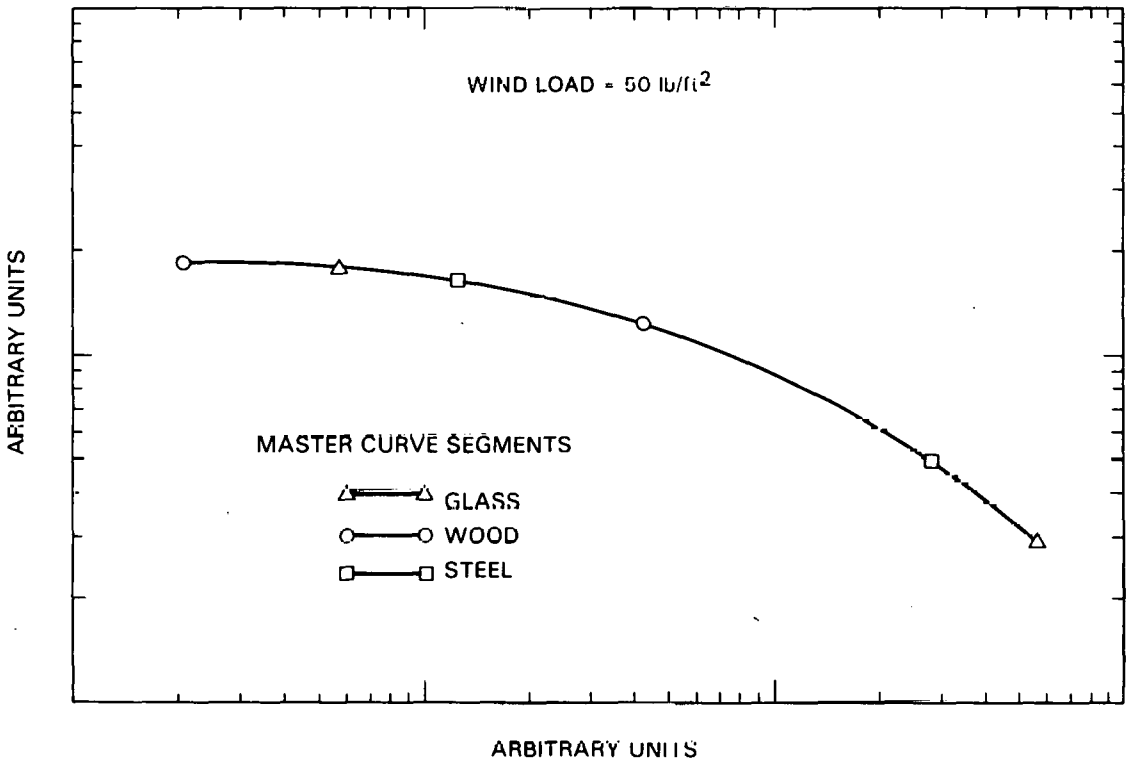

Figure 13. Master Curve for Deflection Stress Analysis (Circa 1982)

Table 14. General List of Structural Parameters Considered for Reduced-Variable Master-Curve Studies

Pottants	Solar Cells	Panel
Modulus	Modulus	Modulus
Thickness	Dimensions (thickness, width, length)	Dimensions (thickness, width, length)
Thermal-expansion coefficient	Thermal-expansion coefficient	Thermal-expansion coefficient
Hygroscopic-expansion coefficient	Intercell-spacing geometry (i.e., round, square, rectangular, etc.)	Hygroscopic-expansion coefficient

A linear interpolation between Curve A and Curve B is to be used for pressure loadings between 10 lb/ft^2 and 50 lb/ft^2.

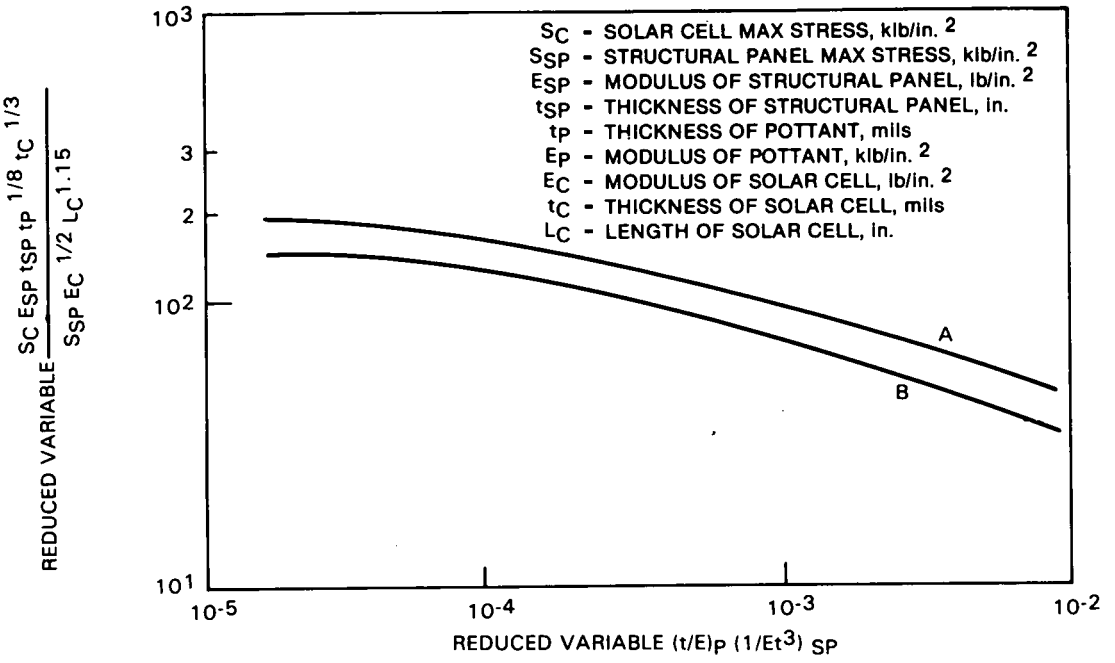

NOTE: USE CURVE A FOR PRESSURE ≤ 10 LB/IN.; USE CURVE B FOR PRESSURE 50 LB/IN.^{2} FOR INTERMEDIATE LOADS. INTERPOLATE LINEARLY BETWEEN A AND B

Figure 14. Master Curve for Deflection Stress Analysis (Circa 1983)

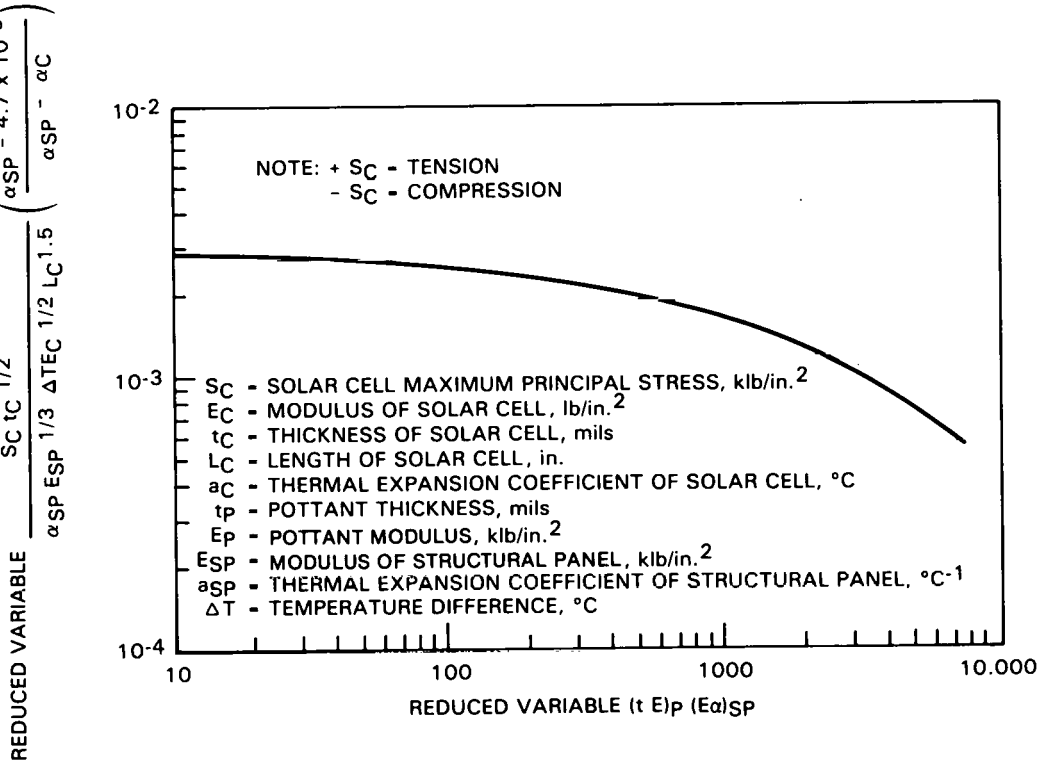

Figure 15. Master Curve for Thermal Stress Analysis (Circa 1983)

a. Reduced-Variable Parameters.

Structural Panel. The important structural panel parameters are Young's modulus E, thickness t, and coefficient of thermal expansion α. Important parameter combinations include flexural stiffness Et^3, and membrane stiffness, Et. Thermal stresses are sensitive to thermal stiffness, $E\alpha$. The cause of thermal stress in the cell is the mismatch of coefficients of thermal expansion of the structural panel and the cell, $\alpha_{SP} - \alpha_c$, and the temperature change, ΔT.

Pottant. The key pottant parameters are Young's modulus and thickness. Cell stress decreases as the pottant stiffness decreases. For an elastomeric pottant, the stiffness decreases when the thickness is increased, or as Young's modulus is decreased. If the pottant is not elastomeric (i.e., $E > 10^4$ lb/in.^{2}), cell stress does not decrease as the pottant thickness is increased. A stiff pottant does not permit relative movement between the cell and the structural panel. Therefore, consistent with conventional beam theory, cell stress for stiff pottants increases as the distance between the cell and the structural panel increases.

Solar Cell. Cell stress is sensitive to Young's modulus, thickness, and cell size. In addition, thermal stress is sensitive to the difference between the coefficients of thermal expansion of the cell and the structural panel.

Cell stress decreases as Young's modulus is decreased. Cell stress is also decreased as the thickness is increased, perhaps because the cell is more resistant to strain as the thickness increases.

Cell stress decreases as the size decreases. As the cell gets smaller, it is deformed less as the module deflects.

If the coefficient of expansion of the cell is less than that of the load-bearing layer, an increase in module temperature generates tension stress in the cell, and a decrease in module temperature generates compression in the cell. The stresses are reversed if the coefficient of thermal expansion of the cell is greater than that of the load-bearing layer.

Parameter Limits. The computer analyses from which the master curves were derived encompassed the following parameter ranges (in general, these limits can be increased or halved by a factor of two without degrading the accuracy; cell thickness should not be less than 2 to 3 mils because the master curves have not been verified for thin-film solar cells):

Structural Panel

E 0.75 to 30 x 10^6 lb/in.^{2}

t 0.04 to 0.25 in.

α 7 to 24 x 10^{-6} in./in. • ^oC.

Pottant

E 0.5 to 2.5 x 10^3 lb/in.^{2}

t 0.001 to 0.020 in.

Cell

E 5 to 30 x 10^6 lb/in.^{2}

t 0.005 to 0.015 in.

α 1 to 12 x 10^{-6} in./in. ^oC

L 1 to 4 in.

b. Additional Considerations.

Structural-Panel Stress. The master curve for pressure loading requires the stress in the structural panel, S_{SP}. This stress must be determined independently by separate analysis. For example, the design curve of Reference 15, shown in Figure 16, can be used to determine the maximum stress in a simply-supported plate subjected to uniform pressure loading.

Solar-Cell Geometry. The master curves apply for square, rectangular, and round cells. Since cell stress increases as the length increases, the critical dimension is the length of the longest edge, or in the case of round cells, the diameter.

Module Pressure Load. The master curve for pressure stress contains two curves. Curve A is used when the module pressure load is less than or equal to 10 lb/ft^2. Curve B applies for a module load of 50 lb/ft^2, which represents a wind velocity of 100 mi/h. For intermediate loading, interpolate linearly between Curves A and B.

Combined Pressure and Thermal Loading. When a module is subjected to simultaneous temperature and pressure loading, the resultant cell stresses should be combined according to the following criterion (Reference 6):

$$\frac{\sigma_P + \sigma_T}{\sigma_{BT}} \leq 1.0$$

where

σ_P = cell stress due to pressure loading

σ_T = cell stress due to thermal loading

σ_{BT} = cell breaking stress

The design is adequate if the computed value is less than or equal to 1.0. If it is greater than 1.0, cell failure may occur.

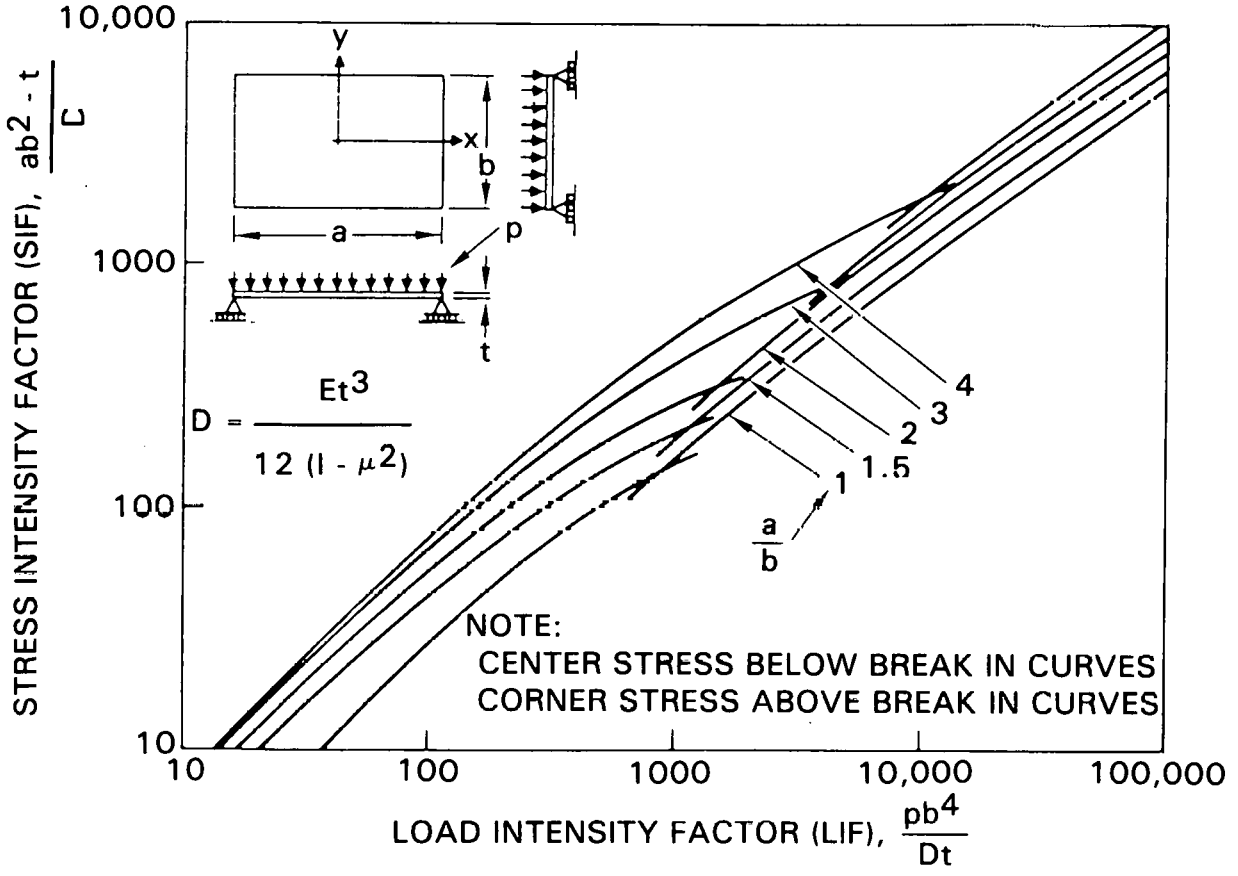

Figure 16. Stress Intensity Factor (SIF) versus Load Intensity Factor (LIF) Showing Composite Curves of the Larger of the Maximum Positive Principal Stresses on Plate (Center Bottom or Top Surface Near Corner); See Reference 15

c. Sample Problem. The following design problem demonstrates the use of the master curves.

Loading: $\Delta T = +100^{o}C$
wind pressure = 50 lb/ft^2

Structural Panel: glass

$E_{SP} = 10 \times 10^6$ lb/in.^{2}

$t_{SP} = 0.125$ in.

$\alpha_{SP} = 9.2 \times 10^{-6}$ in./in. ^{o}C

$S_{SP} = 6$ klb/in.^{2}

Pottant: EVA

$E_P = 1$ klb/in.^{2}

$t_P = 5$ mils

Solar Cell: Silicon, 4 x 0.010 in.

$E_C = 17 \times 10^6$ lb/in.^{2}

$t_C = 10$ mils

$\alpha_C = 4.7 \times 10^{-6}$ in./in. • ^oC

$L_C = 4$ in.

(1) Deflection Stress Analysis (Figure 14)

$$(t/E)_P \left(\frac{1}{Et^3}\right)_{SP} = 2.56 \times 10^{-4}$$

From Curve B, Figure 14

$$\frac{S_C E_{SP} t_{SP} t_P^{1.8} t_C^{1.3}}{S_{SP} E_c^{1/2} L_c^{1.15}} \doteq 9 \times 10^1$$

$\therefore S_C = \sigma_P = 3.33$ klb/in.^{2}

(2) Thermal Stress Analysis (Figure 15)

$$(t/E)_P \, (E\alpha)_{SP} = 460$$

From Figure 6

$$\frac{S_C t_C^{1/2}}{\alpha_{SP} E_{SP}^{1.3} \Delta T \, E_c^{1/2} L_c^{1.5}} \left(\frac{\alpha_{SP} - 4.7 \times 10^{-6}}{\alpha_{SP} - \alpha_c}\right) \doteq 2 \times 10^{-3}$$

$\therefore S_C = \sigma_t = 4.13 \times 10^3$ lb/in.^{2}

(3) Combined Loading Analysis

Compute

$$\frac{\sigma_P + \sigma_T}{\sigma_{BT}} \stackrel{?}{\leq} 1.0$$

where

σ_P = cell stress due to wind pressure = 3330 lb.in.^{2}

σ_T = cell stress due to thermal excursion = 4130 lb/in.^{2}

σ_{BT} = cell breaking stress = 5000 lb/in.^{2}, silicon (Reference 1)

$$\frac{\sigma_P + \sigma_T}{\sigma_{BT}} = \frac{3330 + 4130}{5000} = 1.5$$

$$1.5 > 1.0$$

Conclusion: Cell fracture may occur

Recommendation: Increase pottant thickness

3. Summary

The key results of this work to date are:

(1) The master curves are useful design tools for predicting solar-cell stress for any combination of structural panel, pottant, and solar cell of conventional thickness.

(2) Cell stress decreases as the pottant thickness is increased or the pottant elastic modulus is decreased.

(3) Cell stress decreases as the elastic modulus of the cell decreases. Cell stress increases as the cell size increases. Cell stress increases as the cell thickness decreases.

(4) Thermal stress in a cell is a function of the difference between the coefficients of thermal expansion of the cell and of the structural panel.

(5) The master curves are applicable for square, rectangular, or round cells. The critical dimension is the length of the longest edge, or in the case of round cells, the diameter.

(6) The master curves do not depend upon the geometry of the structural panel. The stress in the structural panel due to pressure loading is required. However, this must be determined by independent analysis that takes into account the support conditions, geometry, and load magnitude.

D. ELECTRICAL ISOLATION (SAFETY) MODELING

1. Introduction

The encapsulation materials enclosing the solar cells and their associated electrical conductors and terminals must also function as electrical insulation materials, isolating encapsulated high-voltage points from accidental human contact, and must have sufficient electrical resistance to prevent electrical breakdown or arc-through to external metallic parts in physical contact with the module. Included in this requirement is sufficient electrical insulation between metallic substrates or metallic foils that may be used in back covers, and the encapsulated solar cells with their electrical circuitry. The electrical insulation of solar cells and their circuitry must be provided by nonmetallic construction materials, such as glass, wood, elastomeric pottants, plastic-film top covers, etc. The present FSA requirement is that the encapsulation system be capable of insulating against 3000 Vdc.

A three-part electrical isolation program has evolved encompassing the following:

(1) Electrical stress aging of nonmetallic encapsulation materials.

(2) Investigations related to understanding controlling and/or limiting manufacturing and material flaws.

(3) Computer-assisted-modeling of the levels and intensity of electrical fields and stresses set up in encapsulation materials by encapsulated electrical sources such as solar cells, metallization, interconnects, and terminals and terminal connections.

Experiments in electrical stress aging of nonmetallic encapsulation materials began late in the summer of 1983. Electrical stress aging is a material behavior in which a material's dielectric strength decays gradually as the material is exposed to a sustained or cyclically applied voltage. Typically, the decay rate is logarithmic and insulation lifetime is related in part to the level of the applied voltage and the logarithmic decay rate. Coupled with this are the presently unknown or unclear effects on electrical stress aging of the absorption of atmospheric water vapor, of material aging caused by thermal oxidation or UV photooxidation, and by any tensile or compressive mechanical forces. Ample evidence in the literature (Reference 16) suggests that the decay mechanism eventually approaches an asymptote, and that there is a design limit below which insulation failure apparently does not occur. Review of the papers in Reference 16 on electrical insulation indicates that this asymptotic level may be as low as 20% of the material's initial dielectric strength. But these same experimental studies were generally carried out under controlled laboratory conditions with applied voltage as the single and only stress imposed on the materials. Aging under multiple-stress conditions, i.e., electrical, mechanical, chemical, and physical, has virtually not been done. Furthermore, almost all electrical-stress-aging studies have been carried out with ac voltage, and relatively little work has been done under dc voltage conditions. And last, there are no known fundamentally sound predictive methods or techniques for estimating electrical insulation lifetime, especially to 20 or 30 years in an outdoor service environment.

Some experimental work related to understanding and quantifying material flaws in plastic-film materials is reported in References 17 and 18. There is currently no further work to report.

In 1983, emphasis was given to developing a computer-assisted model to derive the levels and intensities of electrical fields and stresses set up in encapsulation materials by encapsulated electrical sources. A model was developed, which will be described in detail in a contractor report (Reference 6). Described herein are the results from an initial study with the computer-assisted model, and the generation therefrom of a different view of the definition of the dielectric strength properties of insulation materials. This new concept involves a possible identification of the fundamental dielectric strength as a definable and measurable material property, similar to modulus, expansion coefficiences, etc. Accordingly, then, this fundamental property could be monitored during accelerated or natural aging, independent of the electrical system or electrical environment in which the material is to be used. The background leading to the identification of this intrinsic material property is presented, and, with respect to life prediction, it is intended that this property be investigated as a future FSA activity.

2. Electrical Field Modeling

Figure 17 depicts a round solar cell in an encapsulation pottant, separated by distance t from a flat-plate ground electrode. The latter could be an electrically grounded metal substrate or a metal-foil back cover. The edge of the solar cell is assumed to be a semicircle of radius R. The solar cell is at a dc potential V above ground. Laplace's field equations, which would generate the space distribution of the equipotential lines between the cell and ground, and the values of the electrical field gradients (dE/dt),

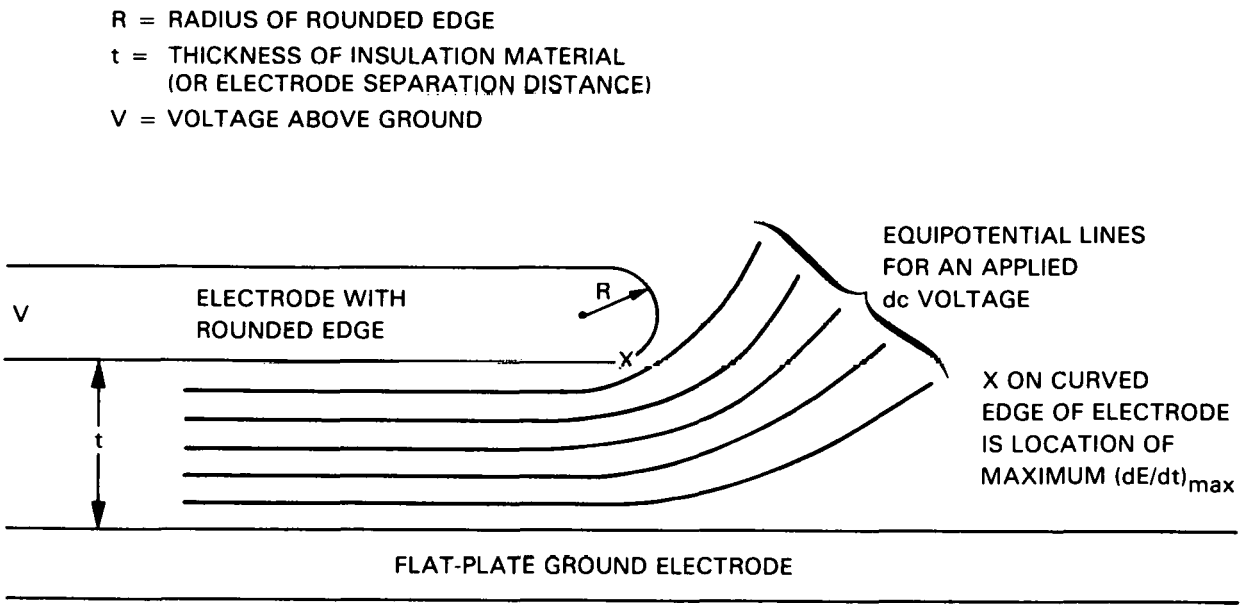

Figure 17. Solar-Cell Electrode Geometry Analyzed by the Spectrolab Computer Program

cannot be solved for this geometry. The computer-assisted model developed by Spectrolab, Inc., can solve, for this and other geometries, the space distribution of the equipotential lines within the pottant insulation material, and generate the value of the maximum electrical field gradient $(dE/dt)_{MAX}$, which will generally occur along the curved edge of the solar cell.

For the geometry represented in Figure 17, it was found that the computer-generated-results could be simply stated by two reduced-variable expressions, one involving the dimensions t and R, and the other involving the maximum field gradient and the average field gradient: that is, $(dE/dt)_{MAX}$ and V/t. It is convenient to define the average voltage gradient V/t as V_a. The reduced-variable expressions are

$$V_a/(dE/dt)_{MAX} = (V/t)/(dE/dt)_{MAX} \tag{14}$$

$$\text{and } (t)/(2R) \tag{15}$$

The computed-generated values for these reduced variables are given in Table 15, for the range of (t)/(2R) from 0.25 to 50.0.

For constant voltage V, the data can be viewed either as increasing or decreasing R at constant t, or as increasing or decreasing t at constant R.

For the former, the data trend indicates that the intensity of the maximum electrical field gradient increases relative to the average field gradient V_A as R decreases. This is expected, as it is known that the

Table 15. Computer-Generated Values of $V_a/(dE/dt)_M$ as a Function of (t/2R) for the Example Illustrated in Figure 17

(t/2R)	$V_a/(dE/dt)_{MAX}$
0.25	0.9116
0.50	0.8200
1.00	0.7004
2.00	0.5648
5.00	0.3916
10.00	0.2968
20.00	0.2305
50.00	0.1898

electrical field intensity increases around sharp corners or edges, or around needle-tip electrodes as the radius of the tip decreases. For the second view, the data indicate that the intensity of the maximum electrical field gradient numerically approaches the average field gradient V_a as t decreases, suggesting that when t = 0, V_a and $(dE/dt)_{MAX}$ become numerically the same.

Given that the electrical field behavior for the geometry represented in Figure 17 can be described by the two reduced-variable expressions, an effort was made to combine the variables into an analytical expression. Figure 18 is a linear-linear plot of these two reduced-variables, using the data in Table 15. Examination of the curve in Figure 18 suggests a hyperbola; therefore, trial plotting of the computer-generated data in hyperbolic format led to a much

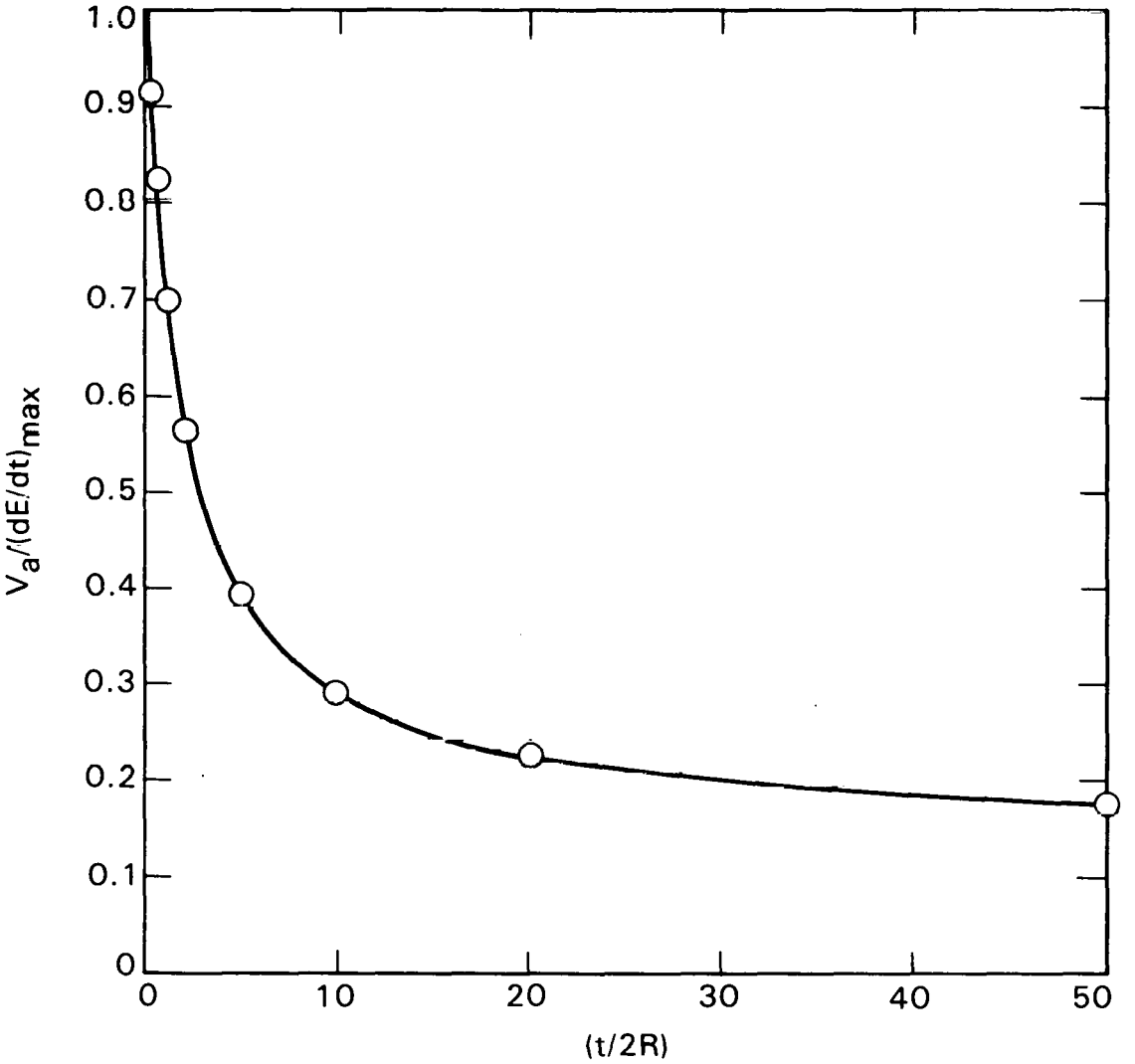

Figure 18. Plot of the Data in Table 15

better, nearly linear plot as shown in (Figure 19). The abscissa variable is generated as follows:

$$\frac{1}{(t/2R) + 1} = \frac{2R}{(t + 2R)} \tag{16}$$

Next, examination of the data trace in Figure 19 suggests that actual linearity may be achieved if the term 2R/(t + 2R) is adjusted by a fractional exponent, which can be determined from a log-log plot as shown in Figure 20. For this plot, a solid line is used on the right side of the trace where it is initially linear for small values of t, and a dotted line is used on the left side where curvature develops for large values of t. The slope of the linear portion is 0.54, or very nearly 1/2.

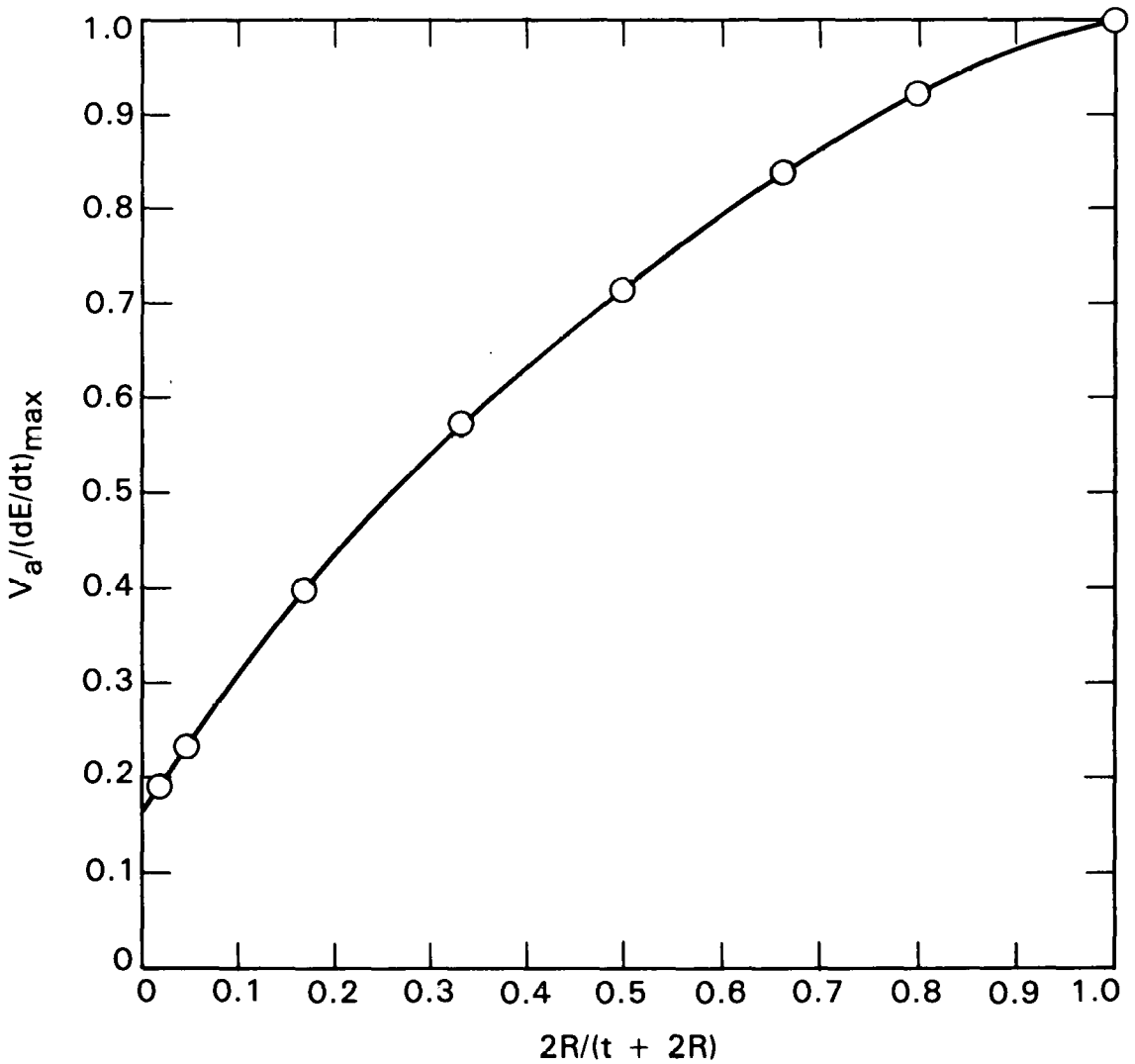

Figure 19. Linear-Linear Plot of Table 15 Data as $V_a(dE/dt)_{MAX}$ Versus the Variable 2R/(t + 2R)

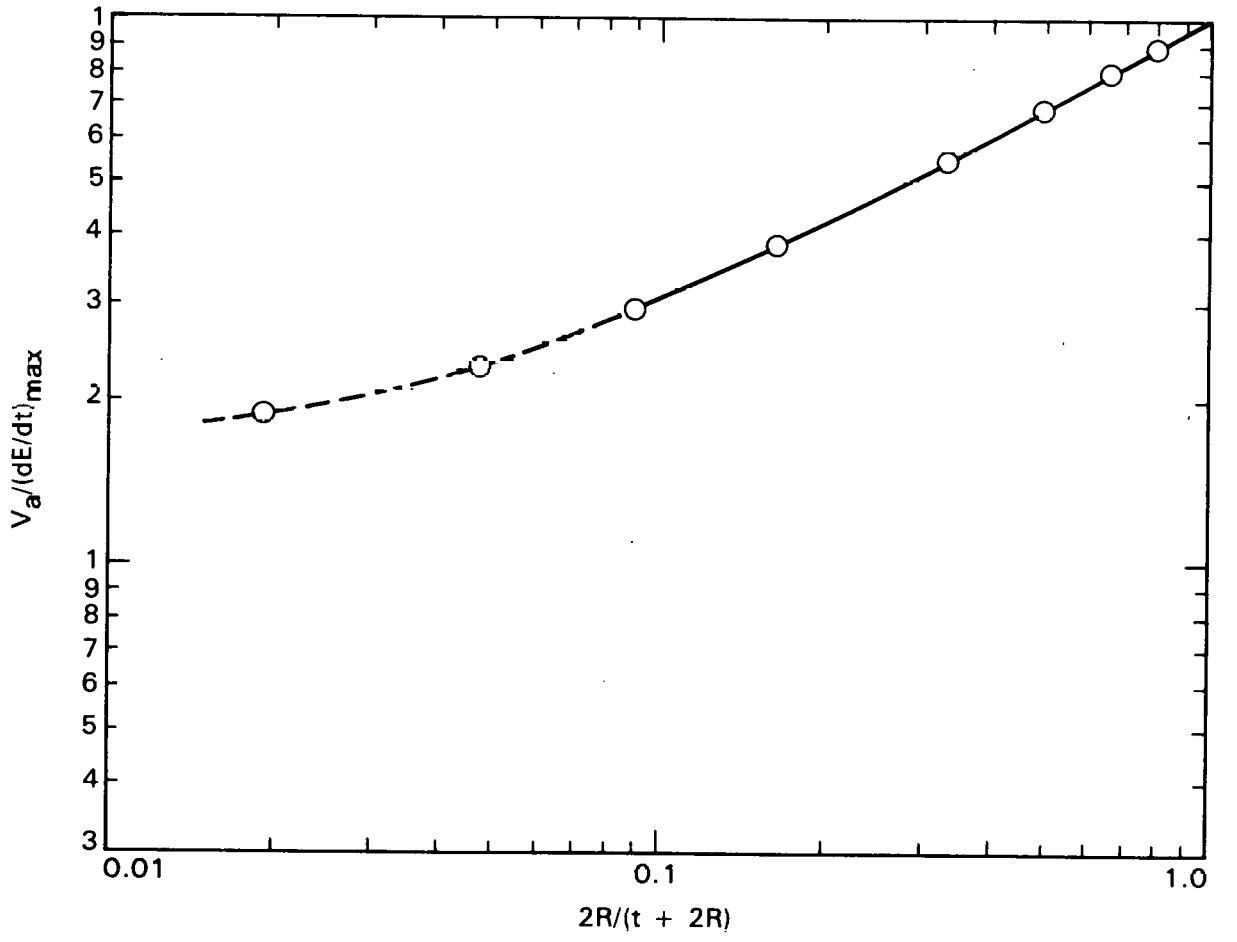

Figure 20. Log-Log Plot of Table 16 Data as $V_a/(dE)/dt)_{MAX}$ Versus the Variable 2R/(t + 2R)

Thus for the linear portion of the log-log trace of Figure 20 the following relationship can be established:

$$V_a/(dE/dt)_{MAX} = k\left(\frac{2R}{t + 2R}\right)^{0.54} = k\left(\frac{t + 2R}{2R}\right)^{-0.54} \quad (17)$$

Further algebra with Equation 17 yields

$$V_a = (dE/dt)_{MAX}(k)(2R)^{0.54}\left(\frac{1}{t + 2R}\right)^{0.54} \quad (18)$$

and if K is defined as $(dE/dt)_{MAX}(k)(2R)^{0.54}$, then

$$V_a = K\left(\frac{1}{t + 2R}\right)^{0.54} \equiv K(t + 2R)^{-0.54} \tag{19}$$

Last, if $t >> 2R$, or if 2R is ignored in Equation 19, then

$$V_a = K/t^{0.54} \equiv K(t)^{-0.54} \tag{20}$$

The resultant Equation 20 is strikingly similar to a historically observed empirical expression that relates V_a to t and which is described in Reference 19. Figure 21, reproduced from Reference 1, is a log-log plot of literature-reported and experimentally measured V_a versus t data for polymethyl methacrylate (PMMA). This empirical relationship between the average voltage gradient V_a at electrical breakdown and insulation thickness t has been known for years, and is described in the ASTM standard (Reference 19) for dielectric strength measurements as a data correlation technique. This correlation behavior has been assigned historically as a property of insulation materials, but this analysis suggests that this may be a consequence of electrode geometry configuration, and not of material behavior. It can be strongly speculated that if Laplace's field equations for the electrode geometrics used in ASTM voltage breakdown testing could have been solved analytically, it would have revealed this electrode-based relationship between V_a and t.

Laplace's field equations have been solved for needle electrodes, which are not ordinarily used for dielectric-strength measurements. Nevertheless, the analytical expressions can be examined for their behavior at small values of t. The analytical solution (Reference 20) for a double-needle electrode geometry, in which the needles are axially aligned and with the needle tips pointing at each other, is

$$(dE/dt)_{MAX} = \frac{Vt(1 + 2R/t)^{1/2}}{2R \tanh^{-1}[t/(t + 2R)]^{1/2}} \tag{21}$$

Simplifying this expression for small t yields:

$$V_a = (dE/dt)_{MAX}(3R)(t + 3R)^{-1} \tag{22}$$

Note that $V_a = (dE/dt)_{MAX}$ for $t = 0$. Also, with this analytical expression at least, the extrapolation of Figure 18 to $V_a/(dE/dt)_m = 1$ at $t = 0$ is justified. Also note the mathematical similarities with Equation 19. For this needle-tip-to-needle-tip geometry, note that the exponent is -1.

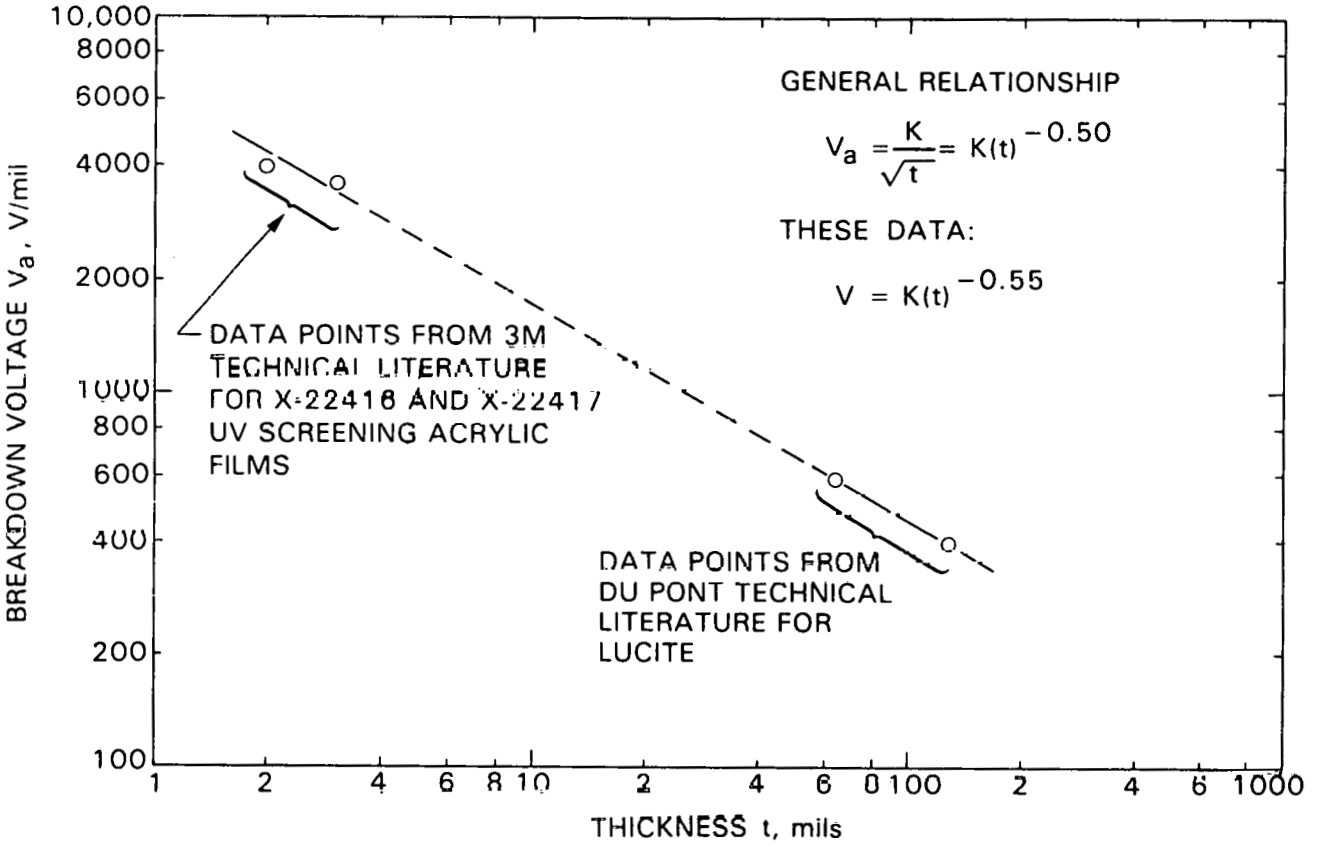

Figure 21. Breakdown Voltage of Polymethyl Methacrylate as a Function of Thickness

An analytical expression similar to Equation 21 has also been solved (Reference 21) for the needle-to-flat-plate case. The analytical expression is:

$$(dE/dt)_{MAX} = 2VtP/Ln(Q) \qquad (23)$$

where

$$P = (1 + R/t)^{1/2}/R$$

and

$$Q = [2t + R + 2t^{1/2}(t + R)^{1/2}]/R$$

For small t, Equation 23 reduces to:

$$V_a = (dE/dt)_{MAX}(R)^{2/3}(t + R)^{-2/3} \qquad (24)$$

Equation 24 is similar in form to Equation 19, and the exponent for this case is a fractional power.

Equations 19, 23 and 24 are all similar in form, and therefore can be represented by the general expression

$$V_a = k(t + a)^n \tag{25}$$

where k, a, and n become constants that must be determined for a set of V_a versus t data. For t = 0, Equation 25 becomes

$$V_a = Ka^n \equiv (dE/dt)_{MAX} \tag{26}$$

and $(dE/dt)_{MAX}$ can be considered as the value of the electric field gradient that must be reached to initiate voltage breakdown of the insulation material. By this approach, $(dE/dt)_{MAX}$ can be viewed as the intrinsic, or fundamental dielectric strength of insulation materials.

Equation 25 was solved by a least-squares technique for the PMMA literature data shown in Figure 21, to yield

$$V_a = 8009(t + 0.87)^{-0.63} \tag{27}$$

The ASTM procedure for measuring these data consisted of a round-edged electrode and flat-plane ground surface. The magnitude of the exponent, -0.63, corresponds to the magnitude noted in Equation 24 for the needle-tip-to-ground-plane configuration.

For t = 0, Equation 27 reduces to

$$V_a = (dE/dt)_{MAX} = (8009)(0.87)^{-0.63} = 8740 \text{ V/mil} \tag{28}$$

suggesting that this may be the value of the electrical field gradient required on electrode surfaces to initiate voltage breakdown of PMMA. In other words, it is the intrinsic dielectric strength of PMMA.

Some preliminary measurements have been made of the breakdown voltage of EVA as a function of its thickness. These data, reported as V_a and t, are given in Table 16. The measurements were made with two equivalent round-faced electrodes, and as such, simulate a needle-tip to needle-tip electrode configuration. Equation 25 was solved by a least-squares technique for the EVA data shown in Table 15, yielding:

$$V_a = 19173(t + 3.74)^{-0.96} \tag{29}$$

Table 16. Dc Voltage Breakdown of A-9918 EVA as a Function of Thickness

Average Voltage Breakdown Gradient[a] V_a, V/mil	Material Thickness t, mils
2500	4.7
2177	6.0
1125	15.7

[a]The average voltage breakdown gradient V_a is defined as V/t

Where V = voltage at breakdown
and t = material thickness

Note that the magnitude of the exponent -0.96 is very nearly -1, in agreement with the expectation for equivalent electrodes.

For t = 0, Equation 29 reduces to

$$V_a = (dE/dt)_{MAX} = 19173(3.74)^{-0.96} = 5404 \text{ V/mil} \quad (30)$$

This suggests that this may be the value of the electric field gradient required to initiate voltage breakdown of EVA, and therefore, the intrinsic dielectric strength of EVA.

It was remarked at the beginning of this subsection that the dielectric strength of insulation materials under sustained electrical stress decays with time, apparently to an asymptote. The PMMA and EVA data reported here are short-term measurements, and therefore represent initial values. It is tempting to view $(dE/dt)_{MAX}$ as the insulation material property that decays with time, which is reflected in K in Equation 25, and to view a and n as time-invariant constants that are fixed by design. This perspective will be investigated as part of the experimental electrical stress-aging program.

E. WOODEN-SUBSTRATE PANEL HYGROSCOPIC RESPONSE MODELING

Photovoltaic modules having hardboard wooden substrate panels, and fabricated with EVA pottant by vacuum lamination, experienced a high failure rate (Reference 1) due to solar-cell breakage and cracking. Analysis (Reference 22) revealed that the hardboard panels dried and shrank during

vacuum lamination at 150°C, and later, when deployed outdoors, reabsorption of moisture led to extreme hygroscopic expansion, which cracked the encapsulated solar cells.

The absorption of atmospheric moisture by wooden hardboard products is virtually linear with increasing atmospheric humidity, and at 70°F and 100% RH, reaches a saturation limit of about 10 wt % of absorbed water. This corresponds to an expansion of about 0.0050 in./in. at saturation. By contrast, the thermal expansion coefficient of hardboard is 7.2 x 10^{-6} in./(in.)(°C), and therefore a temperature excursion of nearly 700°C would be required to achieve the same expansion that results from a moisture reabsorption from 0% RH to 100% RH. Figure 22 traces the dimensional changes of a small piece of hardboard, initially equilibrated to near 45% RH at room temperature, resulting from a heating cycle under vacuum from room temperature to 150°C and back to room temperature. The initial length of the wooden sample at 45% RH was 0.3050 in., decreasing to 0.3047 in. when dried. This corresponds to a contraction of about 0.0023 in./in., which for a 45% RH difference is proportional to the 100% RH saturation value of 0.0050 in./in.

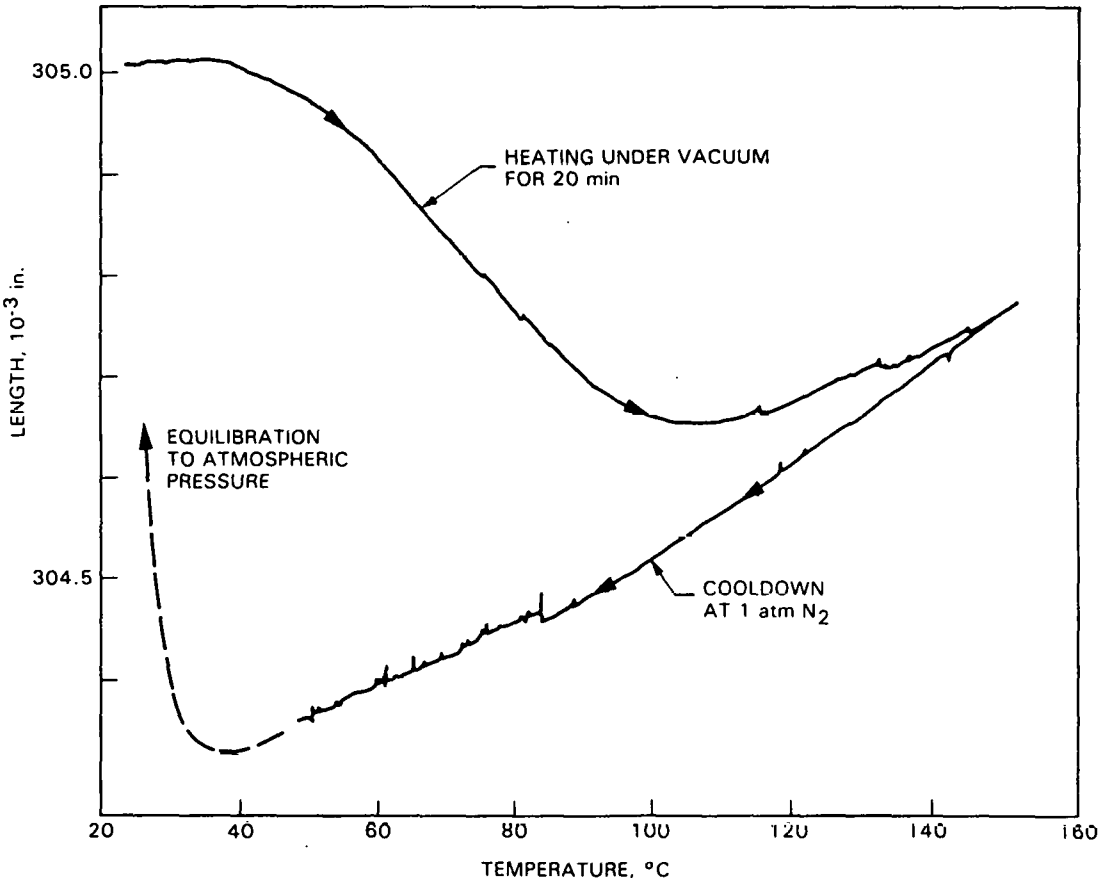

Figure 22. Dimensional Change of Hardboard Under Vacuum-Bag-Lamination Processing Condition (Initial Conditions: Room Temperature, 45% RH)

Master-curve techniques to estimate the level of mechanical stresses imposed on encapsulated solar cells resulting from the expansion of substrate panels were reported in Reference 14; Figure 23, reproduced from Reference 14, depicts the level of stresses imposed on solar cells resulting from hygroscopic wood expansion. The predicted solar-cell tensile stresses tend to be high, requiring very thick layers of pottant material to reduce the generated tensile stresses to acceptable levels. A pottant with a Young's modulus of 500 lb/in.^{2} would have to have a predicted thickness of about 33 mils; a pottant, such as EVA, with a Young's modulus of about 1000 lb/in.^{2}, would have to be at least 66 mils thick. Even if the relative-humidity excursion after vacuum-bag lamination were only up to 50% RH, which is more realistic, the thickness of a pottant such as EVA would still have to be at least 33 mils. The experimental hardboard modules, presently fabricated with EVA, use no more than 18 mils of EVA between the cells and the wood.

The predicted results and actual observations of a high incidence of solar-cell cracking with EVA-hardboard modules fabricated by vacuum-bag lamination generated an impetus to develop wood-lamination techniques and wood-coating technologies to eliminate or greatly reduce problems associated with hygroscopic behavior.

Toward this end, a mathematical model was developed in 1983 to predict the combined hygroscopic and thermal expansion and contraction behavior of plastic-film-coated hardboards exposed to fluctuating conditions of atmospheric temperatures and humidities. Metal-foil coatings on hardboard

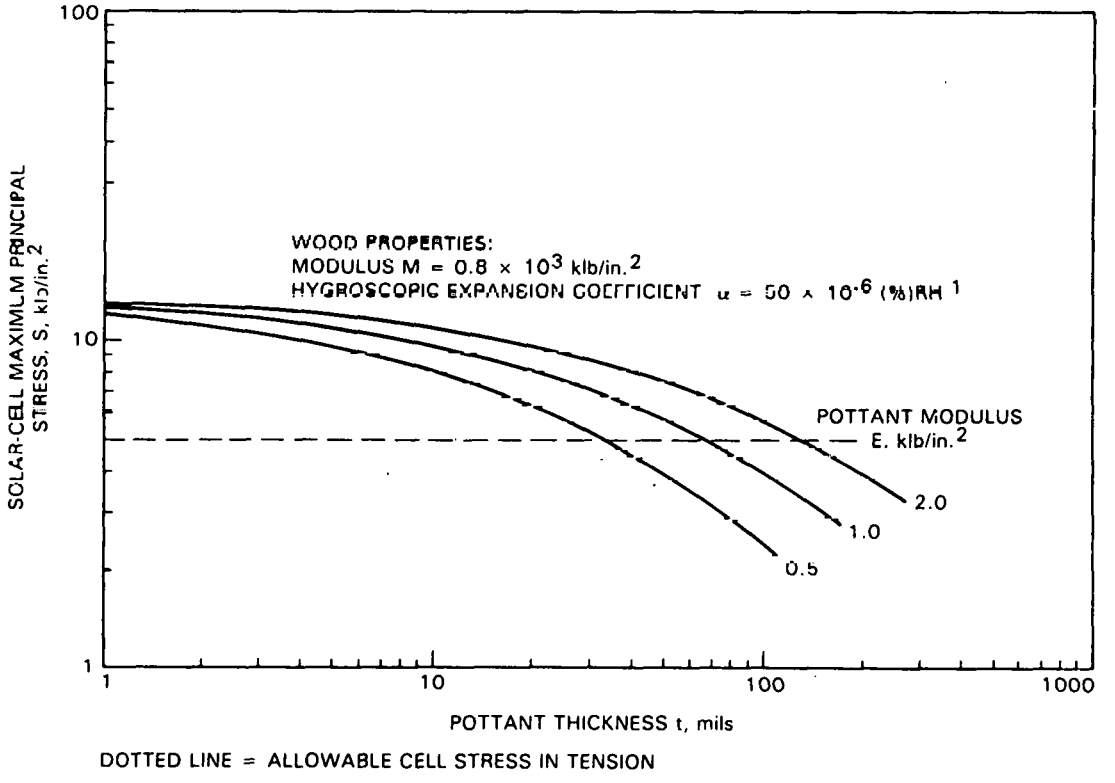

Figure 23. Predicted Stresses in Encapsulated Silicon Solar Cells Resulting from Hygroscopic Expansion of a Hardboard Panel from 0% to 100% Relative Humidity (Reference 14)

would function as humidity barriers, reducing the expansion and contraction of hardboard to temperature fluctuations only. But metal-foil coatings would still require an exterior coating of a plastic film to increase emissivity and thus to reduce module operating temperature (Reference 1). Furthermore, plastic-coated metal foils cost more than plastic films alone. The model described is intended to determine if cost-effective thicknesses of plastic films can reduce substantially the hardboard's hygroscopic response to fluctuating atmospheric moisture to acceptable expansion and contraction levels.

The simple model, relevant equations, and definitions of the variables and constants are shown in Figure 24. A hardboard panel of thickness h is coated on one side with a plastic film of thickness f, and the opposite side of the hardboard is coated with a hermetic barrier. This effectively consists of the thick slab of pottant, solar cells, and outer-cover film on the sun side of the module. Moisture entering or departing the hardboard must permeate through the plastic film, at a rate controlled by the permeation constant P_e of the plastic film, and the difference in the atmospheric water vapor content on the two sides of the film. The permeation constant P_e of plastic films is temperature-dependent, and the relationship between P_e and temperature T (in ^oK) is Arrhenius in form. Since atmospheric temperature T varies with time t, P_e becomes a function of time, i.e., $P_e(t)$. H_p is the activation energy of permeation, which for plastic films typically varies between 5 and 10 kcal/(mol)(^oK) (Reference 23).

The absorbed water content of hygroscopic materials such as hardboard is a function of both atmospheric temperature and atmospheric water vapor concentration. It is convenient to express the concentration of water vapor in the atmosphere in terms of water vapor pressure V, in units of mm Hg. Then the concentration C of absorbed water vapor is given by the relationship

$$C = K(T)V \tag{31}$$

where C is in units of grams of water per gram of dry wood, and K(T) is the absorption isotherm. K(T) is a function of temperature, and its relationship with T is Arrhenius in form. H_A is the activation energy of absorption, which typically varies between 5 and 10 kcal/(mol)(^oK). Since atmospheric temperature varies with time, K(T) becomes a function of time, i.e., K(t).

The saturation water content of hardboard at 70°F (21.1°C) and 100% RH is 10 wt %. This corresponds to a concentration c, as follows:

$$c = 10/90 = 0.111 \text{ grams water/gram dry wood} \tag{32}$$

the saturation vapor pressure of water at 100% RH at 70°F (21.1°C) is 18.7765 mm Hg; therefore, K(T) at 70°F (21.1°C) is

$$K(21.1^oC) = (0.111)/(18.7765) = 5.918 \times 10^{-3} \frac{\text{grams water}}{(\text{grams dry wood})(\text{mm Hg})} \tag{33}$$

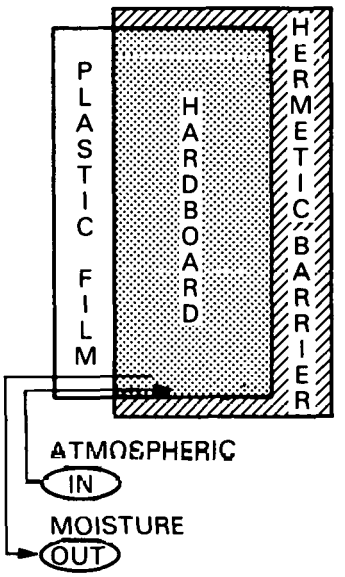

C = ABSORBED WATER CONTENT IN WOOD, g WATER/(g DRY WOOD)
t = TIME, h
h = WOOD THICKNESS, in.
f = FILM THICKNESS, MILS
ρ = WOOD DENSITY, G/in^3
V(t) = ATMOSPHERIC WATER VAPOR CONTENT, mm Hg
T(t) = AIR TEMPERATURE, °K
R = GAS CONSTANT, 1.987
$P_e(t)$ = PERMEATION CONSTANT, (g WATER)(MILS)/(in.^{2})(h)(mm Hg)
K(t) = ABSORPTION ISOTHERM, (g WATER)/(g DRYWOOD)(mm Hg)
H_P = PERMEATION ACTIVATION ENERGY, CAL/(MOL)(°K)
H_A = ABSORPTION ACTIVATION ENERGY, CAL/(MOL)(°K)

Mass Balance Differential Equation:

$$dC/dt = \frac{P_e(t)}{K(t)\ h\ f\ \rho}\left(K(t)\ V(t) - C\right) \tag{4}$$

Plastic Film Permeation Constant:

$$P_e(t) = P_0 \times EXP\left(\frac{-H_P}{RT(t)}\right) \tag{5}$$

Wood's Water Absorption Isotherm:

$$K(t) = K_0 \times EXP\left(\frac{H_A}{RT(t)}\right) \tag{6}$$

Figure 24. Details of the Hygroscopic Model

Unfortunately, a value for the activation energy H_A for water absorption by hardboard could not be found; therefore, H_A was taken to be the midrange value of 7500 cal/(mol) (°K). With this selection of H_A, and the value of K at 21.1°C, the value of the constant K_0 in the Arrhenius expression for the time and/or temperature dependence of the absorption isotherm for hardboard:

$$K(t) = 1.59 \times 10^{-8} \exp\left(\frac{7500}{1.987 \times T(t)}\right) \tag{37}$$

The plastic film chosen for the model calculation was white-pigmented Tedlar. Du Pont Co. technical literature for Tedlar products reports the following water-vapor permeation constant for Tedlar at 39.5°C:

$$P_e(39.5^{\circ}C) = 2.495 \times 10^{-5} \quad \frac{(\text{g water})(\text{mils})}{(\text{in.}^2)(\text{h})(\text{mm Hg})} \tag{38}$$

But the same technical literature does not report on activation energy H_p, nor has such a value been found in any other literature. Therefore, a midrange value of 7500 cal/(mol)(°K) was selected. With this selection, and the value of P_e at 39.5°C, the value of the constant P_0 in the Arrhenius expression(s) can be determined, to yield an expression for the time and/or temperature dependence of the water-vapor permeation constant for Tedlar:

$$P_e(t) = 4.366 \exp \frac{-7500}{1.987 \times T(t)} \tag{39}$$

The differential equation for this water permeation model, shown as Equation 34 in Figure 24, was derived by mass-balance considerations, and assumes that the rate of water distribution to a uniform concentration within the wood is rapid compared with the rate of water permeating into or out of the wood. The first use of this equation was to assess the hygroscopic response rate of an initially dry, 1/8 in.-thick hardboard coated with a 2-mil Tedlar film, when exposed to 70°F and 100% RH. For this test case, the differential equation becomes

$$\frac{dC}{dt} = A_0(C_0 - C) \tag{40}$$

where A_0 has the value 7.034×10^{-4} h^{-1}, and C_0 has the value 0.111 grams water per gram dry wood.

Integrating Equation 40 yields

$$C/C_0 = 1 - \exp(-A_0 t) \tag{41}$$

which for t = 24 h results in $C/C_0 = 0.167$, or $C/C_0 = 1.67\%$. That is, an initially dry 1/8-in.-thick hardboard coated with 2 mils of Tedlar film will absorb in 24 h less than 2% of its total absorption limit. This calculation strongly indicates that the plastic film coating has a potential for reducing to virtually zero the hygroscopic response of hardboard to short-term fluctuations in ambient humidity, including short-term periods of rainfall or dry air. And of course increasing the film thickness and/or wood thickness would result in even more sluggish response to short-term humidity fluctuations.

Accepting that plastic-film coatings can effectively reduce the hardboard's response to short-term fluctuations, the next determination is to assess the wood's response to longer-term weather patterns. Table 17, reproduced from Reference 24, is a tabulation of the annual weather patterns in Boston, Massachusetts, over a 10-year period from 1965 to 1974. The table lists, for each month, the mean air temperature at each three-hour interval for that month. For example, the mean air temperature at 1 a.m. during January was -2.8°C, and the mean air temperature at 4 p.m. (16th hour) during January was +0.2°C. The tables read in like manner for each of the other months of the year.

Table 17 also includes the atmospheric water content, reported as a dew point. It reveals an interesting pattern: for each month, the mean dew point on a 24-hour basis is practically constant, although there are short-term fluctuations as indicated in the Maximum, Minimum, and Standard Deviation columns. Since plastic-film-coated hardboards are being considered as nonresponsive to short-term humidity fluctuations, it may be assumed that the coated wood seeks equilibrium with the monthly mean value of dew point.

Therefore, for each month, the eight values of mean dew points were averaged to a monthly constant value, and this monthly value was used with standard water-vapor-pressure tables to determine a monthly average water-vapor concentration in units of mm Hg. These are given in Table 18, and the water-pressure values are plotted against calendar months in Figure 25. The plot of the mean values of atmospheric water vapor pressure for Boston is nearly sinusoidal on an annual basis. The figure suggests that the maximum of the water content in the air occurs in mid-July and the minimum in mid-January. These data, shown in Figure 25, will be the function V(t) required for the differential equation shown as Equation 43 in Figure 24.

To derive an annual temperature function T(t) for Boston, the same procedure as used for the dew points was followed. The eight mean values for each month were averaged, and those monthly average values versus calendar months are plotted in Figure 26. These plotted mean values of temperature also are nearly sinusodial on an annual basis.

With T and V no longer constants, Equation 34 in Figure 24 cannot be solved analytically; therefore, the equation is solved using a numerical-integration computer technique. The first case investigated consisted of a 1/8-in.-thick hardboard coated with a 2-mil-thick Tedlar film. The hardboard is initially dry, and is deployed outdoors in Boston in mid-March. This time of year was selected for the start because it was the time of year during which the wooden substrate modules that ultimately had high failure rates were manufactured. The computer results for this case are plotted in Figure 27 for the first three years as absorbed water vapor content in the wood in wt % versus calendar months.

The hardboard, initially dry in mid-March, gradually regains moisture to an intermediate plateau just above 6 wt %, which occurs late in the same year between the 10th and 12th months. Late fall was also the time of year during which the first occurrences of failed wooden substrate modules were observed (Reference 22).

Table 17. Descriptive Environmental Statistics for Boston, Massachusetts, at 3-Hour Intervals by Month for the Years 1965 to 1974

Month and Hour	Air Temperature, °C				Dew Point, °C				Relative Humidity, %				Wind Speed, m/s			
	Mean	Standard Deviation	Maximum	Minimum	Mean	Standard Deviation	Maximum	Minimum	Mean	Standard Deivation	Maximum	Minimum	Mean	Standard Deviation	Maximum	Minimum
1 1	2.8	6.0	14.4	20.0	8.7	8.1	12.8	-31.7	65.4	17.3	100.0	29.0	6.0	2.6	17.5	1.0
1 4	3.3	6.2	11.1	-20.0	-8.8	8.1	11.1	-30.6	66.2	16.8	100.0	30.0	6.0	2.5	14.4	1.0
1 7	-3.6	6.4	14.4	-20.0	-9.1	8.3	13.3	-30.6	66.6	16.3	100.0	35.0	6.0	2.5	13.4	0.5
1 10	-1.9	6.3	15.0	-17.2	-8.5	8.0	12.8	-27.8	61.7	16.8	100.0	26.0	6.5	2.9	17.0	0.0
1 13	0.1	6.1	15.7	-16.1	-7.9	7.8	10.0	-27.2	57.0	18.4	100.0	24.0	6.8	3.0	17.0	1.0
1 16	0.2	5.8	16.1	-16.7	-8.0	7.7	12.8	-28.9	56.3	19.1	100.0	21.0	6.5	2.9	16.5	0.0
1 19	-1.1	5.6	14.4	-18.3	-8.2	7.9	12.2	-31.1	60.6	18.9	100.0	23.0	6.1	2.7	17.5	1.0
1 22	-2.1	5.7	14.4	-18.9	-8.5	7.8	12.8	-30.6	63.1	18.0	100.0	25.0	6.2	2.8	16.5	0.0
2 1	-2.6	5.1	11.7	-17.2	-8.5	7.6	10.0	-35.0	64.9	18.7	100.0	20.0	6.1	2.6	15.4	1.0
2 4	-3.2	5.3	10.6	-18.9	-8.7	7.7	8.3	32.2	67.1	17.5	100.0	29.0	6.0	2.6	14.9	1.0
2 7	-3.6	5.3	9.4	18.9	-8.9	7.5	7.8	-30.0	67.8	17.5	100.0	29.0	6.0	2.7	14.4	0.0
2 10	-1.7	4.9	11.1	-16.1	-8.6	7.5	8.3	-30.0	62.0	19.0	100.0	19.0	6.5	3.0	18.0	1.0
2 13	0.3	4.8	12.8	-12.8	-7.7	7.0	7.8	-26.1	57.8	20.4	100.0	14.0	6.8	3.1	19.0	0.0
2 16	0.7	4.7	13.9	-12.2	-7.5	7.2	11.7	-30.6	57.2	21.0	100.0	18.0	6.9	3.0	20.1	1.0
2 19	-6.0	4.6	13.3	-12.8	-7.7	7.3	10.6	-30.0	61.0	19.8	100.0	22.0	6.2	2.8	15.4	0.5
2 22	-1.6	4.9	13.9	-15.6	-8.0	7.3	10.0	-26.7	63.2	18.9	100.0	24.0	6.1	2.8	12.9	0.0
3 1	1.6	4.2	16.7	-13.3	-4.3	6.2	11.1	-23.3	67.0	18.1	100.0	25.0	5.8	2.5	14.4	0.0
3 4	0.8	4.1	15.0	-13.9	-4.7	6.2	9.4	-23.3	68.8	17.5	100.0	23.0	5.6	2.7	17.5	0.0
3 7	0.8	4.2	13.3	-14.4	-4.7	6.3	11.1	-21.7	68.2	16.9	100.0	26.0	5.9	2.6	18.5	1.0
3 10	3.2	4.4	16.7	-10.6	-4.2	6.3	12.8	-21.7	61.6	19.8	100.0	23.0	6.3	2.9	18.0	0.5
3 13	5.0	4.7	20.6	-8.9	-3.6	6.3	13.9	-21.1	58.0	21.3	100.0	16.0	6.9	2.7	19.5	0.5
3 16	5.2	4.6	19.4	-7.2	-3.6	6.4	14.4	-20.6	57.5	22.1	100.0	16.0	6.8	2.8	17.0	1.0
3 19	3.6	4.1	17.2	-10.6	-3.8	6.4	14.4	-22.2	61.8	20.8	100.0	19.0	6.0	2.7	19.0	0.5
3 22	2.5	4.0	14.4	-11.7	-4.0	6.3	11.1	-22.2	65.2	19.2	100.0	25.0	5.8	2.7	18.0	0.0
4 1	6.4	4.1	23.9	-3.9	0.4	5.6	13.3	-14.4	67.7	17.4	100.0	26.0	5.5	2.4	13.9	0.0
4 4	5.6	4.0	21.1	-4.4	0.1	5.6	13.3	-15.6	70.0	16.8	100.0	29.0	5.3	2.4	14.4	0.0
4 7	6.3	4.1	20.6	-4.4	0.2	5.7	13.3	-16.7	67.5	17.8	100.0	27.0	5.6	2.5	14.9	0.0
4 10	9.5	4.9	23.9	-2.2	0.5	5.8	14.4	-16.1	57.0	20.0	100.0	23.0	6.2	2.6	16.5	0.5
4 13	10.9	5.4	28.9	-2.2	0.9	5.7	15.0	-13.9	54.4	21.1	100.0	16.0	6.9	2.5	16.5	0.5
4 16	10.9	5.3	28.9	0.6	0.9	5.4	15.0	-14.4	55.0	21.5	100.0	15.0	7.0	2.5	16.5	1.0
4 19	9.0	4.6	23.9	-1.1	0.9	5.5	13.3	-15.0	60.8	20.6	100.0	16.0	6.0	2.4	12.9	0.0
4 22	7.6	4.0	22.2	-1.7	0.8	5.3	13.3	-14.4	65.4	19.0	100.0	24.0	5.5	2.3	12.3	1.0
5 1	11.2	3.3	21.7	4.4	6.1	5.0	17.2	-12.8	73.2	17.7	100.0	28.0	4.6	2.0	10.8	0.0
5 4	10.5	3.3	20.6	2.8	6.1	4.8	17.8	-12.2	76.4	15.7	100.0	33.0	4.5	2.0	12.9	0.0
5 7	11.9	3.4	22.8	3.9	6.3	5.0	19.4	-12.8	70.7	17.3	100.0	29.0	4.9	2.0	13.4	0.0
5 10	14.7	4.6	28.9	5.6	6.5	5.3	18.3	-11.7	61.6	20.5	100.0	19.0	5.6	2.3	15.4	0.5
5 13	16.0	5.3	31.7	5.6	6.6	5.4	17.8	-11.7	58.3	21.7	100.0	13.0	6.5	2.3	15.4	1.5
5 16	15.9	5.5	32.8	4.4	6.4	5.4	17.2	-11.7	58.4	23.0	100.0	13.0	6.7	2.5	20.1	1.5
5 19	14.1	4.7	30.0	3.9	6.5	5.2	17.2	-11.7	64.6	21.8	100.0	15.0	5.6	2.5	21.6	0.0
5 22	12.5	3.8	23.9	4.4	6.3	5.2	17.8	-12.8	69.2	19.7	100.0	22.0	5.1	2.3	14.9	0.0
6 1	17.1	3.5	28.3	8.9	12.8	3.8	20.6	-1.7	77.4	13.7	100.0	32.0	4.3	1.8	10.3	0.0
6 4	16.1	3.4	23.9	8.3	12.6	3.7	20.6	2.2	80.8	12.0	100.0	44.0	4.1	1.7	12.3	0.0
6 7	17.8	3.5	27.8	9.4	12.8	3.8	20.6	1.1	74.0	14.1	100.0	39.0	4.5	1.8	10.3	0.0
6 10	21.1	4.8	32.8	10.6	13.2	4.4	21.1	-0.6	63.3	17.9	100.0	26.0	5.1	1.8	12.3	0.0
6 13	22.3	5.5	35.0	10.6	13.3	4.3	21.7	-0.6	60.1	19.7	100.0	23.0	5.9	2.0	11.3	1.0
6 16	22.2	5.6	35.6	10.6	13.3	4.3	22.2	-2.2	60.6	19.2	100.0	18.0	5.9	2.0	12.3	0.5
6 19	20.1	4.6	33.3	9.4	13.3	4.2	22.2	-2.8	67.9	17.9	100.0	20.0	5.1	2.1	11.3	0.5
6 22	18.2	3.9	30.0	9.4	13.2	3.9	21.7	-2.8	74.6	15.4	100.0	25.0	4.6	2.0	10.3	0.0

Table 17. Descriptive Environmental Statistics for Boston, Massachusetts, at 3-Hour Intervals by Month for the Years 1965 to 1974 (Cont'd)

Month and Hour	Air Temperature, °C				Dew Point, °C				Relative Humidity, %				Wind Speed, m/s			
	Mean	Standard Deviation	Maximum	Minimum	Mean	Standard Deviation	Maximum	Minimum	Mean	Standard Deviation	Maximum	Minimum	Mean	Standard Deviation	Maximum	Minimum
7 1	20.4	2.7	29.4	13.9	15.8	3.4	22.8	5.0	76.3	12.9	100.0	4[illegible] 0	4.2	1.7	9.3	0.0
7 4	19.4	2.7	27.2	12.8	15.6	3.3	22.2	6.1	79.4	11.5	100.0	4[illegible] 0	4.0	1.5	7.2	0.0
7 7	21.1	2.6	28.9	15.0	15.7	3.4	22.2	5.6	72.8	13.2	100.0	4[illegible] 0	4.3	1.7	9.3	0.5
7 10	24.3	3.4	32.8	17.2	15.8	3.9	22.2	1.7	61.0	14.9	93.0	2[illegible] 0	5.0	1.7	11.8	0.5
7 13	25.8	4.0	35.6	17.8	15.7	4.0	22.8	2.2	55.9	16.3	93.0	2[illegible] 0	5.7	1.9	11.8	0.5
7 16	25.6	4.1	36.1	16.7	15.7	3.9	22.8	3.3	57.0	17.0	97.0	1[illegible] 0	6.0	1.9	12.3	0.5
7 19	23.3	3.4	34.4	16.1	16.0	3.7	22.8	2.8	65.7	15.9	100.0	2[illegible] 0	4.9	1.8	10.3	0.5
7 22	21.4	2.8	31.7	15.6	16.0	3.5	23.3	3.9	72.8	14.4	100.0	3[illegible] 0	4.4	1.8	9.3	0.0
8 1	20.0	2.8	26.7	10.0	15.7	3.8	22.8	1.7	77.1	13.0	100.0	3[illegible] 0	4.3	1.8	9.3	0.0
8 4	19.1	2.9	26.1	8.9	15.4	3.9	22.2	2.2	79.9	11.7	100.0	4[illegible].0	4.0	1.6	9.3	0.0
8 7	20.2	2.9	26.7	10.0	15.3	4.0	22.2	2.2	74.5	12.3	100.0	4[illegible].0	4.3	1.8	9.3	0.5
8 10	23.7	3.6	32.2	13.3	15.5	4.1	22.8	1.7	61.7	15.0	100.0	3[illegible].0	4.9	1.9	14.4	0.5
8 13	25.4	4.2	36.1	14.4	15.3	4.1	22.8	1.1	56.0	15.9	100.0	2[illegible].0	5.9	1.9	12.9	0.5
8 16	24.9	4.2	34.4	13.9	15.4	4.1	23.3	0.0	58.2	16.9	100.0	2[illegible].0	6.0	1.9	11.3	0.5
8 19	22.5	3.6	31.1	11.7	15.7	3.9	22.2	-0.6	67.4	16.1	100.0	2[illegible].0	4.9	1.9	12.9	1.0
8 22	21.0	3.0	27.8	11.1	15.8	3.8	22.2	2.8	73.4	14.1	100.0	4[illegible].0	4.5	1.8	8.7	0.5
9 1	16.1	3.6	25.6	5.6	12.3	4.7	21.7	0.0	79.4	12.0	100.0	4[illegible].0	4.6	1.8	10.8	0.0
9 4	15.2	3.7	25.6	4.4	12.0	4.7	21.1	0.6	81.8	11.0	100.0	5[illegible].0	4.4	1.7	9.8	0.0
9 7	15.8	3.7	26.7	5.6	11.9	4.8	20.6	0.6	78.7	11.5	100.0	5[illegible].0	4.7	1.9	12.9	0.0
9 10	19.2	4.1	31.7	8.3	12.3	5.0	22.2	-0.6	66.1	15.5	100.0	3[illegible].0	5.4	2.0	12.3	1.0
9 13	20.8	4.6	34.4	10.6	12.4	5.1	22.2	-1.1	60.7	16.6	100.0	2[illegible].0	6.1	2.0	11.3	1.5
9 16	20.3	4.5	33.9	10.6	12.4	5.0	22.8	0.0	63.1	17.8	100.0	2[illegible].0	6.0	1.8	13.4	2.1
9 19	18.1	3.8	30.0	8.9	12.5	4.9	21.7	-2.8	71.7	16.3	100.0	2[illegible].0	4.8	1.9	13.4	0.0
9 22	16.8	3.5	27.8	7.8	12.3	4.8	21.7	-2.2	75.8	14.0	100.0	3[illegible].0	4.6	2.0	12.3	0.0
10 1	10.6	4.2	22.2	-1.1	6.0	6.5	17.8	-11.1	74.6	16.5	100.0	2[illegible].0	4.9	2.1	13.9	1.0
10 4	9.9	4.3	18.9	-1.1	5.7	6.2	16.7	-10.6	76.4	15.2	100.0	3[illegible].0	4.8	2.0	13.4	0.5
10 7	9.9	4.3	18.9	-0.6	5.5	6.2	18.3	-10.0	75.5	14.6	100.0	3[illegible].0	4.9	2.0	11.3	0.0
10 10	13.5	4.4	25.6	1.7	5.9	6.7	18.3	-10.6	62.5	17.5	100.0	2[illegible].0	5.7	2.4	13.9	1.0
10 13	14.2	4.9	29.4	3.3	6.0	6.8	18.9	-11.7	56.5	18.6	100.0	1[illegible].0	6.3	2.3	13.9	1.0
10 16	14.8	4.6	28.9	2.8	5.8	6.9	18.3	-13.3	57.9	19.8	100.0	1[illegible].0	6.0	2.1	13.9	2.1
10 19	12.5	4.1	24.4	0.0	5.9	6.7	19.4	-12.8	66.5	18.6	100.0	2[illegible].0	5.1	2.2	12.9	0.0
10 22	11.2	4.1	23.9	-0.6	6.0	6.6	19.4	-11.7	71.3	17.3	100.0	3[illegible].0	5.1	2.2	12.3	1.0
11 1	5.6	4.5	20.0	-6.1	0.8	6.5	16.7	-13.9	72.9	16.0	100.0	3[illegible].0	5.4	2.3	14.4	1.0
11 4	5.2	4.7	18.3	-7.2	0.6	6.6	15.0	-12.8	73.9	15.7	100.0	3[illegible].0	5.4	2.2	13.4	0.5
11 7	4.9	4.7	17.2	-8.3	0.5	6.6	15.6	-13.9	75.0	15.3	100.0	4[illegible].0	5.6	2.2	11.3	1.0
11 10	7.0	4.5	22.2	-3.9	0.9	6.7	16.7	-13.9	67.2	17.9	100.0	3[illegible].0	6.1	2.8	17.5	0.5
11 13	8.6	4.3	24.4	-1.1	1.0	6.6	18.9	-15.6	61.8	19.6	100.0	2[illegible].0	6.5	2.8	17.0	0.0
11 16	8.0	4.3	23.3	-3.3	0.8	6.8	18.3	-16.7	63.4	19.9	100.0	2[illegible].0	6.1	2.5	14.9	1.5
11 19	6.7	4.2	21.7	-5.0	0.8	6.5	18.3	-15.0	68.4	17.8	100.0	2[illegible].0	5.7	2.4	14.9	1.0
11 22	6.0	4.4	21.7	-5.0	0.8	6.5	17.8	-13.3	71.0	16.5	100.0	3[illegible].0	5.5	2.4	18.5	0.0
12 1	0.6	5.1	17.2	-18.3	-4.7	6.9	15.0	-30.5	69.5	15.6	100.0	3[illegible].0	5.9	2.5	13.9	0.0
12 4	0.2	5.4	16.1	-18.9	-4.7	7.1	14.4	-28.9	71.4	15.2	100.0	3[illegible].0	5.8	2.5	15.4	0.5
12 7	-0.0	5.6	15.0	-19.4	-4.7	7.3	13.9	-30.0	72.3	15.1	100.0	3[illegible].0	6.0	2.6	18.0	0.5
12 10	1.5	5.5	15.6	-18.3	-4.4	7.3	13.9	-29.4	66.3	17.0	100.0	2[illegible].0	6.4	2.8	17.5	1.0
12 13	3.2	5.3	20.0	-13.3	-3.9	6.9	13.3	-26.7	62.1	19.2	100.0	2[illegible].0	6.4	2.9	18.5	1.0
12 16	2.9	4.9	17.2	-13.3	-4.1	7.1	14.4	-28.9	63.1	19.6	100.0	2[illegible].0	6.2	2.8	17.0	0.0
12 19	1.8	4.9	15.0	-14.4	-4.3	7.1	14.4	-28.9	66.4	18.4	100.0	2[illegible].0	6.2	2.7	15.9	1.0
12 22	1.0	5.0	16.1	-16.1	-4.5	7.0	13.9	-29.4	68.2	16.7	100.0	3[illegible].0	6.0	2.6	17.5	0.0

Table 18. Monthly Mean Atmospheric Water-Vapor Concentration in Boston, Massachusetts

Month	Water Vapor Concentration	
	Dew Point, °C[a]	Pressure, mm Hg
January	-8.46	2.425
February	-8.20	2.475
March	-4.11	3.381
April	+0.59	4.780
May	+6.35	7.184
June	+13.06	11.236
July	+15.78	13.450
August	+15.51	13.216
September	+12.26	10.702
October	+5.85	6.941
November	+0.78	4.846
December	-4.41	3.306

[a]Average of the eight values reported for each month in Table 1.

Figure 27 shows that the absorbed water content thereafter meanders gradually upward toward steady-state behavior, as shown for a steady-state three-year period in Figure 28. Also shown in Figure 28, for comparison, is the seasonal variation in absorbed water content of an unprotected hardboard responding only to the atmospheric mean conditions of temperature (Figure 26) and humidity (Figure 25). Note in Figure 28 that the seasonal high and low of absorbed water content for this plastic-film-coated hardboard are out of phase with the seasonal high and low of unprotected hardboard, and therefore also out of phase with the seasonal high and low of temperature (Figure 26) and humidity (Figure 25). This suggests for plastic-film-coated hardboard that some of the annual thermal expansion and contraction may be countered by the annual hygroscopic expansion and contraction, thereby in effect reducing the annual extreme between the dimensional highs and lows. This suggests interesting possibilities for coating design optimization.

In Figure 26, the seasonal spread in Boston mean air temperatures is about 24.5°C, which for hardboard having a thermal expansion coefficient of 7.2×10^{-6} in./(in.)(°C) corresponds to a seasonal dimensional spread of about 17.6×10^{-5} in./in. for thermal expansion and contraction only. For the plastic-film-coated hardboard example described, that is a 2-mil Tedlar film on 1/8-in.-thick hardboard, the combined annual thermal and hygroscopic expansion and contraction results in a seasonnal dimensional spread of 26.9×10^{-5} in./in. The thermal expansion coefficient of glass is 9.2×10^{-6} in./(in.)(°C), which for a temperature range of 24.50°C results in a

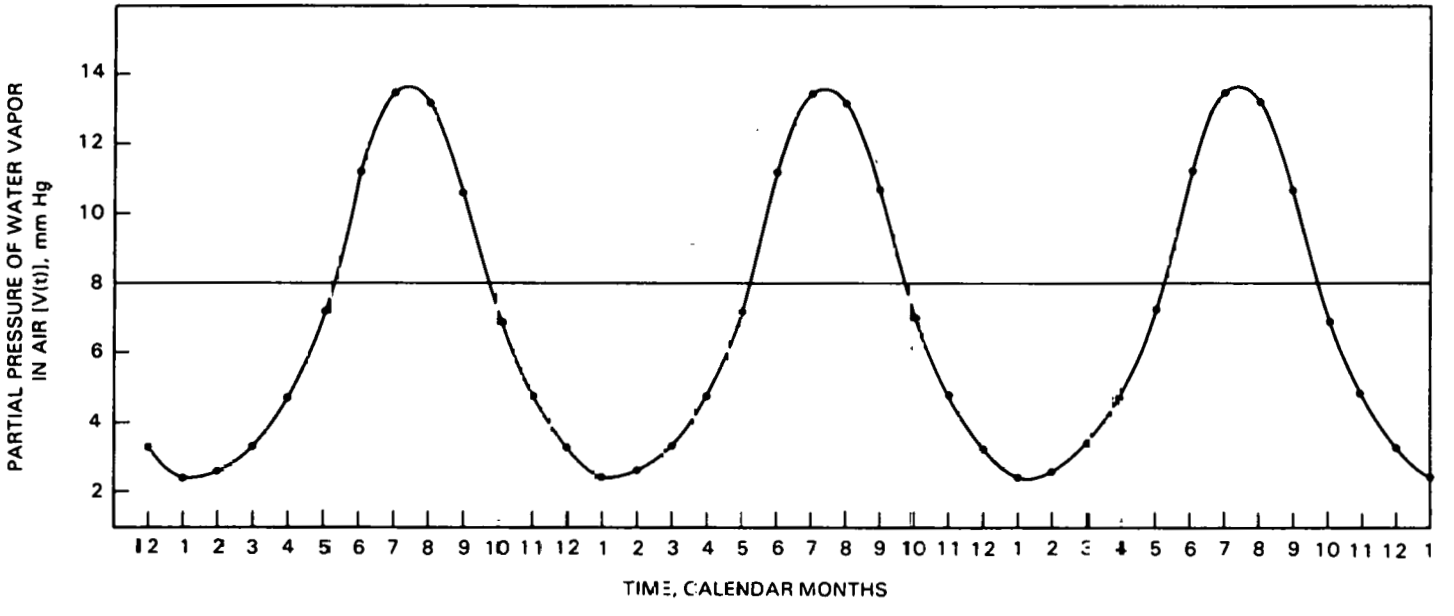

Figure 25. Annual Variation of the Mean Atmospheric Water-Vapor Concentration in Boston, Massachusetts

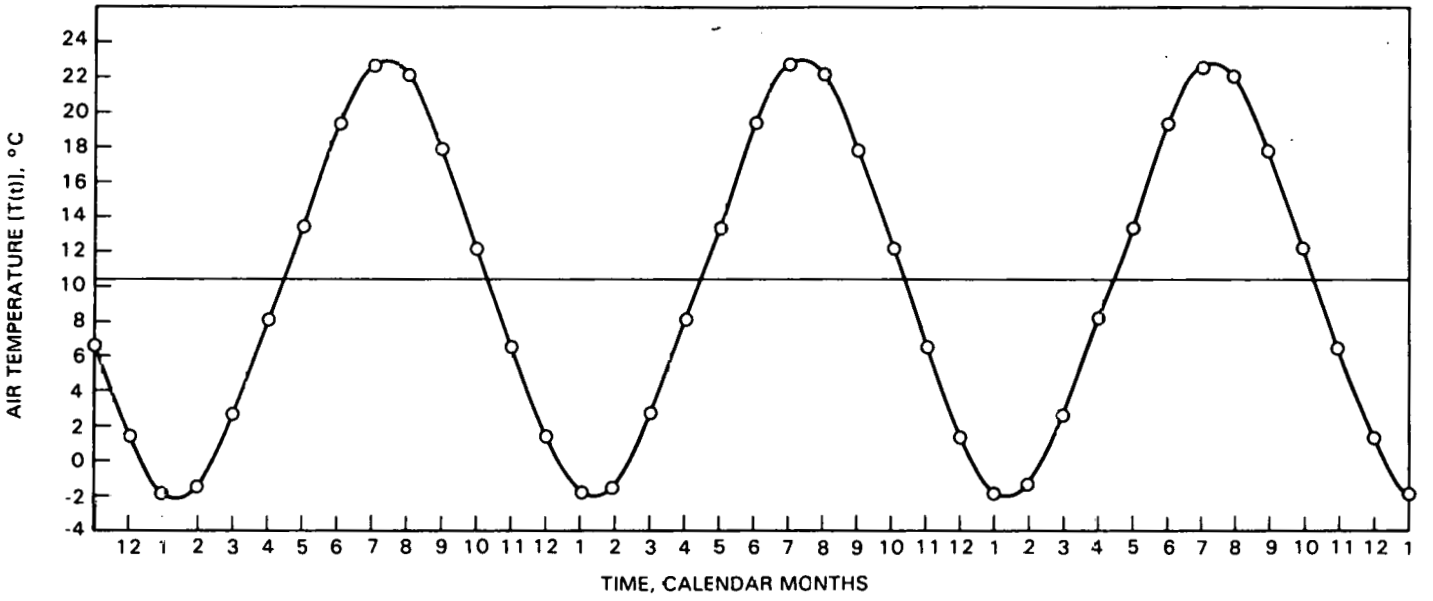

Figure 26. Annual Variation of the Mean Air Temperature in Boston, Massachusetts

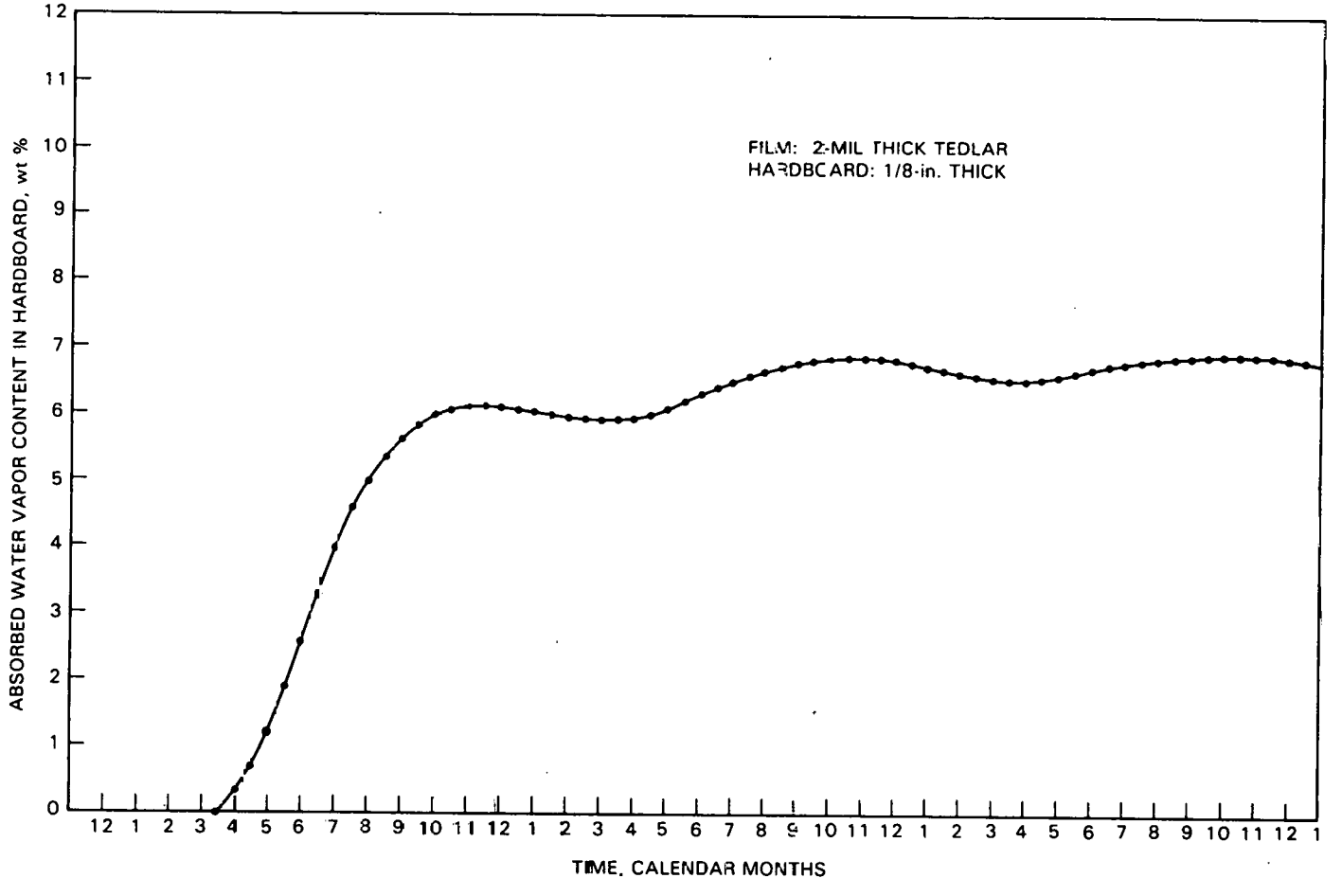

Figure 27. Absorption of Atmospheric Water Vapor by an Initially Dry, Plastic-Film-Coated Hardboard in Boston, Massachusetts

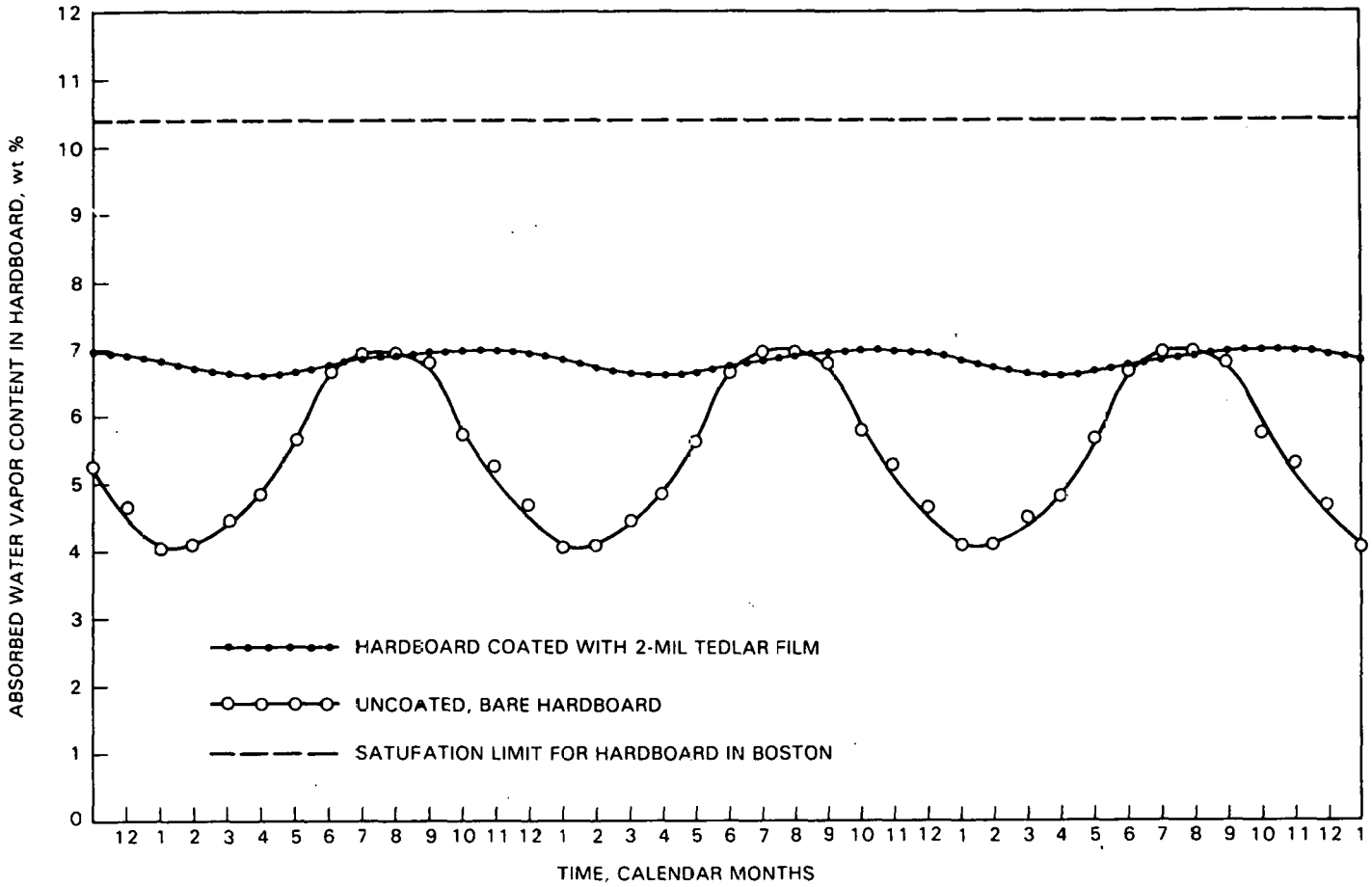

Figure 28. Annual Variation of Absorbed Atmospheric Water Vapor in Plastic-Film-Coated and Uncoated Hardboards for Annual Mean Temperature and Humidity Conditions in Boston, Massachusetts

seasonal dimensional spread of 22.5 x 10^{-5} in./in. Thus a 2-mil Tedlar film on 1/8-in.-thick hardboard has reduced the seasonal dimensional spread of the hardboard to nearly that of glass.

Recently, for structural and manufacturing reasons, interest has shifted from ribbed 1/8-in.-thick hardboard to unribbed 1/4-in.-thick hardboard. Equation 34 in Figure 24 was resolved for a 2-mil-thick Tedlar film on 1/4-in.-thick hardboard, yielding a seasonal dimensional spread of 20.6 x 10^{-6} in./in. from combined thermal and hygroscopic expansion and contraction, which is now slightly less than that of glass. Figure 29 compares the seasonal expansion and contraction of glass with that of 1/4-in.-thick hardboard coated with a 2-mil-thick Tedlar film. Additionally, the steady-state level of absorbed water level is also near 7 wt. %, as found (Figure 28) for the 1/8-in. hardboard with a 2-mil thick Tedlar film.

Hygroscopic modeling of hardboard has indicated that plastic film coatings can substantially and significantly reduce the contribution of hygroscopic expansion and contraction to the seasonal dimensional spread of hardboard. Further, the plastic-film coatings virtually eliminate the hygroscopic response of hardboard to short-term fluctuations in atmospheric water content (e.g., rain, dew, dry air).

Before this modeling was carried out, a 24-in.-square, 1/8-in.-thick hardboard sample coated on both sides with a 1-mil white-pigmented polyester film (Scotchpar 10-CP-White, 3M) was exposed outdoors in Pasadena, California. Strain transducers were mounted on it to monitor dimensional changes, which were set to a zero reading on the start date of December 14, 1982. Table 19 records the dimensional high and lows, in inches, observed at monthly intervals from December 14 to the last reading date, May 26, 1983. Over this period the dimensional changes of the plastic-film-coated hardboard ranged from a low of -0.011 in. to a high of +0.005 in., for a span of 0.016 in. The dimensional spread in inches per inch for this span is (0.016)/(24) = 66.7 x 10^{-5} in./in. An uncoated 1/8-in. hardboard functioning as a comparative control has undergone a dimensional spread of nearly 250 x 10^{-5} in./in. over this same period. Clearly the 1-mil plastic film on each side of 1/8-in.-thick hardboard has reduced the hygroscopic contribution to expansion and contraction, but 66.7 x 10^{-5} in./in. is still a high value.

The 1/8-in. hardboard coated on both sides with 1-mil-thick plastic film can be viewed symmetrically as a 1/16-in.-hardboard coated on one side with a 1-mil-thick plastic film, and having a hermetic barrier on the opposite side. Therefore, Equation 34 in Figure 24 was solved for this case; the combined thermal and hygroscopic dimensional spread is plotted in Figure 30. Although the data pattern for such a thin cross section of wood is interesting, it is more significantly to be noted that that predicted magnitude of the dimensional spread is of the order of 70 x 10^{-5} in./in., which is of the order of magnitude being observed experimentally in the outdoor test. This near agreement in the magnitude of experimental data with the predictions of a model increases confidence in model results.

To avoid wood dryout associated with the vacuum lamination process, a split lamination process is being investigated experimentally. In this process, solar cells are vacuum-laminated in EVA with its outer cover plastic film, then this section is adhesively bonded to the hardboard substrate at room temperature. In a prior operation, the white-pigmented back-cover plastic

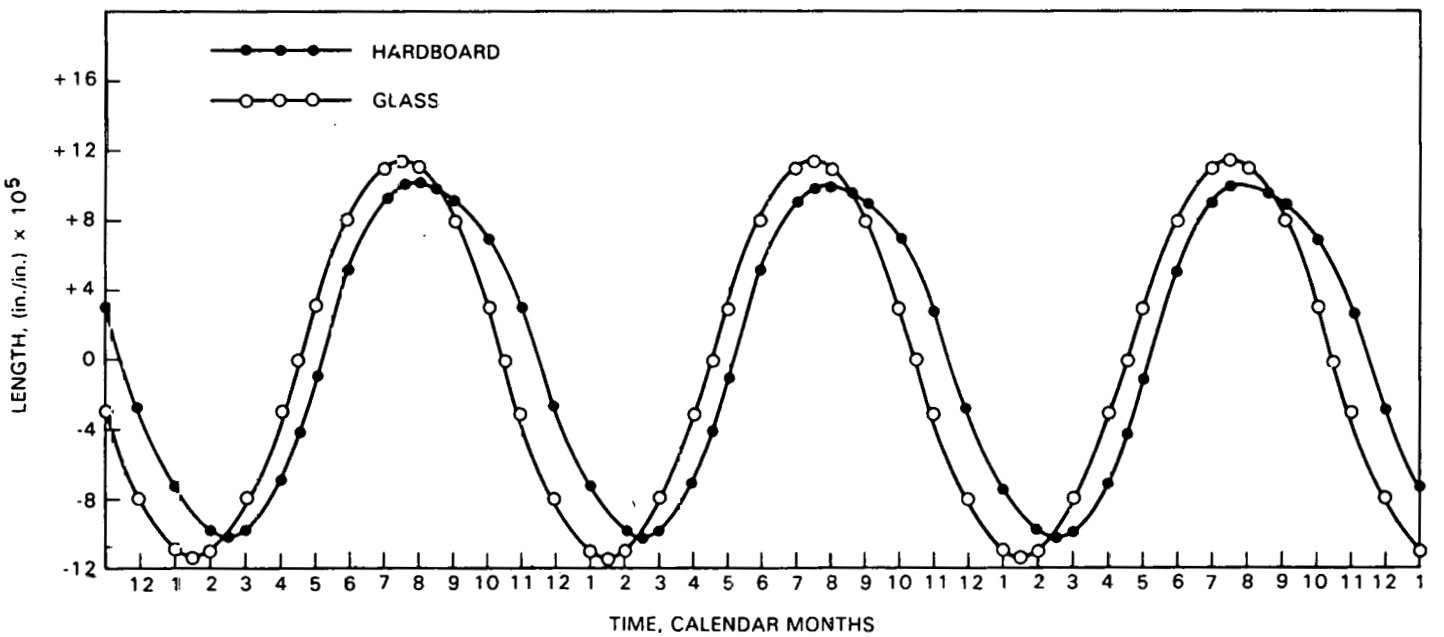

Figure 29. Annual Dimensional Expansion and Contraction of Plastic-Film-Coated 1/4-in. Hardboard, Compared With That of Glass, in Boston, Massachusetts

Table 19. Experimentally Measured Expansion and Contraction of a 1/8-in.-Thick Hardboard[a] Coated on Both Sides With a 1-mil-Thick Polyester Film, in Pasadena, California

Monthly Interval	Dimensional Extremes, in.[b]	
	High	Low
Dec. 14, '82 - Jan. 13, '83	+0.001	-0.010
Jan. 14 - Feb. 13	+0.004	-0.011
Feb. 14 - March 13	+0.005	-0.005
Mar. 14 - April 13	+0.005	-0.006
April 14 - May 13	+0.003	-0.007
May 14 - May 26, '83	-0.002	-0.008

[a]Hardboard specimen is 24 in. square.

[b]Measurements are from a strain gauge that was set to a zero reading on the start date, Dec. 14, 1982.

film is bonded adhesively to the back side of the hardboard. The hygroscopic modeling indicates that the steady-state absorbed water content of coated hardboard will be near 7 wt %, which corresponds to about 70% RH at room temperature. Hardboard panels should be equilibrated to these environmental conditions before being fabricated into photovoltaic modules.

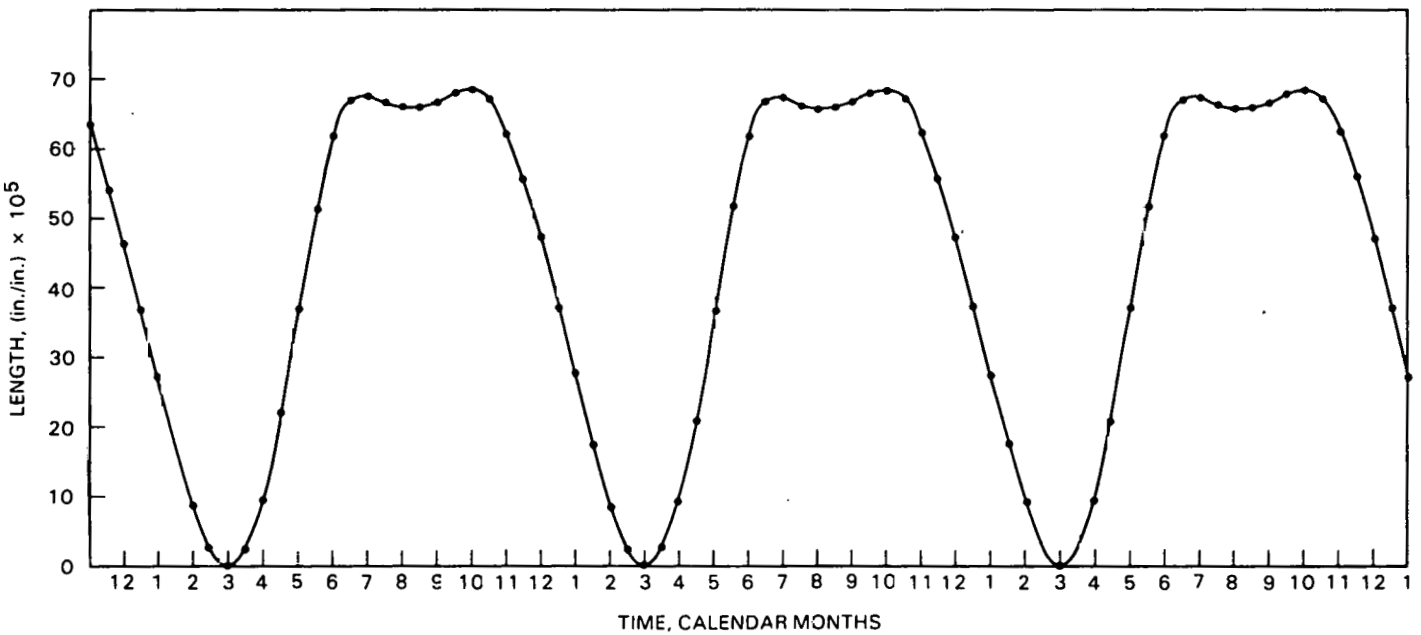

Figure 30. Annual Dimensional Expansion and Contraction of a 1/8-in.-Thick Hardboard Coated on Both Sides With 1-mil-Thick Tedlar, in Boston, Massachusetts

F. FIELD TESTING OF EXPERIMENTAL ENCAPSULATION SYSTEMS

1. Introduction

A minimodule and submodule field-testing program was initiated in 1980 as part of the Environmental Isolation Task of FSA. Its purpose is to provide information about the weatherability, compatibility, and corrosion protection of experimental module designs, and of new and developing materials, using real-time outdoor exposure supplemented by a limited amount of accelerated testing. Observations of degradation modes and mechanisms resulting from such exposure can be combined with data from more extensive accelerated testing to define the phenomena that limit module life--knowledge that is crucial to the development of accurate models for predicting solar array performance.

This field-testing program, of three years' duration, made use of 150 minimodules of 12 types--some quite similar in design--and 365 submodules (containing two cells) of four types. Figure 31 provides a convenient guide to the important features of these module types. In brief, several modules of each type were subjected to standard JPL qualification testing: thermal-cycle and humidity-freezing cycle tests, determination of nominal operating cell temperature (NOCT), partial-discharge test, and hail-impact test. Some modules underwent accelerated testing at DSET Laboratories, Inc., Phoenix, Arizona. Most, however, were weathered at three locations in Southern California: JPL's main laboratory site in Pasadena, JPL's Goldstone Tracking Station in the Mojave Desert, and at a site just outside the U.S. Coast Guard Station at Point Vicente. Table 20 shows how these modules were distributed among the various tests.

Results show little loss of maximum power output, except in two types of modules. In the first of these (Types I and II, Figure 31), failure is due to hygroscopic expansion and contraction of hardboard substrates as described in the preceding section, and in the second, the glass superstrate is sensitive to cracking, which also damages the cells electro-statically bonded to it; inadequate bonding of interconnects to the cells is also a problem in these modules. (Type VII, Figure 31). In a third type of module, a polyurethane pottant has begun to yellow, though without significant effect yet on maximum power output (Types XI and XII, Figure 31). (Note: The polyurethane pottant is not Z-2591).

All JPL qualification testing and DSET accelerated testing for this program have been completed. Minimodule and submodule field testing is a continuing effort that includes periodic visual, electrical, and chemical evaluation of the deployed modules. All modules that have failed during field testing (including those with zero power output) have been returned to their test sites after failure analysis so that additional materials degradation can be monitored.

An extensive document, FSA Field Test Report 1980-1982 (Reference 22), was published April 15, 1983, describing this activity in detail. This section is a summary of that report; readers desiring additional details or expanded information should see Reference 22.

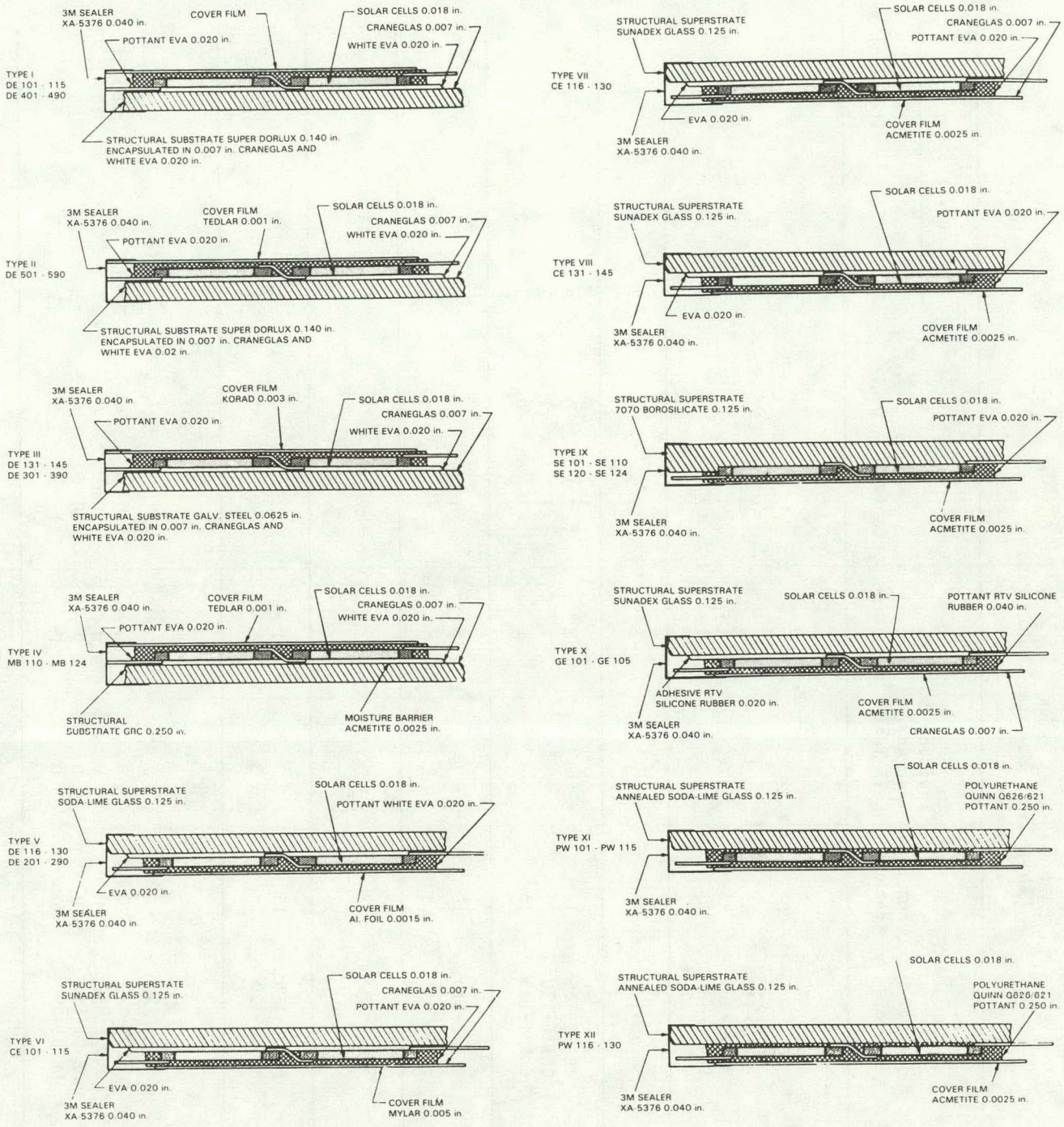

Figure 31. Module Types

Table 20. Module Distribution

Module Type	Manufacturer	Serial Numbers	Quantity Tested	Environment and Hail Test	Partial Discharge	Control	DSET	Outdoor Exposure		
								JPL	Goldstone	Point Vicente
Mini-modules										
I	Springborn Laboratories	DE101-115	15	3	1	1	1	3	3	3
III		DE131-145	15	3	1	1	1	3	3	3
V		DE116-130	15	3	1	2	0	3	3	3
IV	Tracor MBA	MB110-124	15	3	1	2	0	3	3	3
VI	Applied Solar Energy Corp.	CE101-115	15	3	1	2	0	3	3	3
VII		CE116-130	15	3	1	1	1	3	3	3
VIII		CE131-145	15	3	1	2	0	3	3	3
IX	Spire Corp.	SE101-110	10	1	1	1	1	2	2	2
		SE120-124	5	0	0	2	0	1	1	1
X	General Electric Co.	GE101-105	5	1	1	0	0	1	1	1
XI	Photowatt International, Inc.	PW101-115	15	3	1	2	0	3	3	3
XII		PW116-130	15	3	1	2	0	3	3	3
Sub-modules										
V	Springborn Laboratories	DE201-290	90	0	0	19	6	23	21	21
III		DE301-390	90	0	0	20	6	23	21	20
I		DE401-490	90	0	0	18	6	23	20	23
II		DE501-590	90	0	0	19	6	23	21	21

2. Module Designs and Materials

a. Overview. The field-testing program is intended to investigate both the degradation processes that occur in the materials of photovoltaic modules and the resultant effects on electrical performance. It was not considered necessary to work with full-size commercial modules manufactured in a normal production run. Instead, smaller modules were produced in special laboratory runs, using designs and processes that could be used for manufacture of future full-sized modules. For these reasons, it must be emphasized that the field-test results cannot be applied directly to the rating of commercial products, although they do provide insight into material responses to common environmental stresses and into the sensitivity of the design to these stresses.

Two module configurations were used: minimodules are 12 x 16 in. (30 x 40 cm) and contain several cells (Figure 32); submodules are 5 x 9 in. (13 x 23 cm) and contain two 4-in. (10-cm)-diameter cells. Use of the simple two-cell submodules allows comprehensive statistical examination of the behavior of encapsulants, sealants, interconnects, terminations, etc., relatively inexpensively. In contrast, interactions between nonadjacent cells, effects of unmatched or anisotropic thermal expansion, edge phenomena, etc., may require testing the larger and more expensive minimodules. Such problems as module stability when subjected to wind loading or out-of-plane torques would require full-scale modules, but are considered design-related rather than materials-related, and so are beyond the scope of this section.

Materials were selected for use in fabricating these test modules on the basis of the following considerations:

(1) Suitability of their physical, mechanical, and chemical properties, not only in terms of module life but also of module producibility.

(2) Availability in sufficient quantity for industrial use at relatively low cost.

(3) Lack of available design-related data, including expected materials lifetimes, at the outset of the program.

(4) Generality of designs, intended to be representative of concepts that may be used in next-generation modules.

Consequently, several low-cost materials were used to fabricate structural substrates, but only glasses were used as structural superstrates.

b. Modules With Structural Substrates. The first four module types shown in Figure 31 are made with structural substrates. The designs are fundamentally the same: the photovoltaic circuit is encapsulated in EVA (clear above and white below), and sandwiched between a protective top cover film and a layer of Craneglas over the substrate.

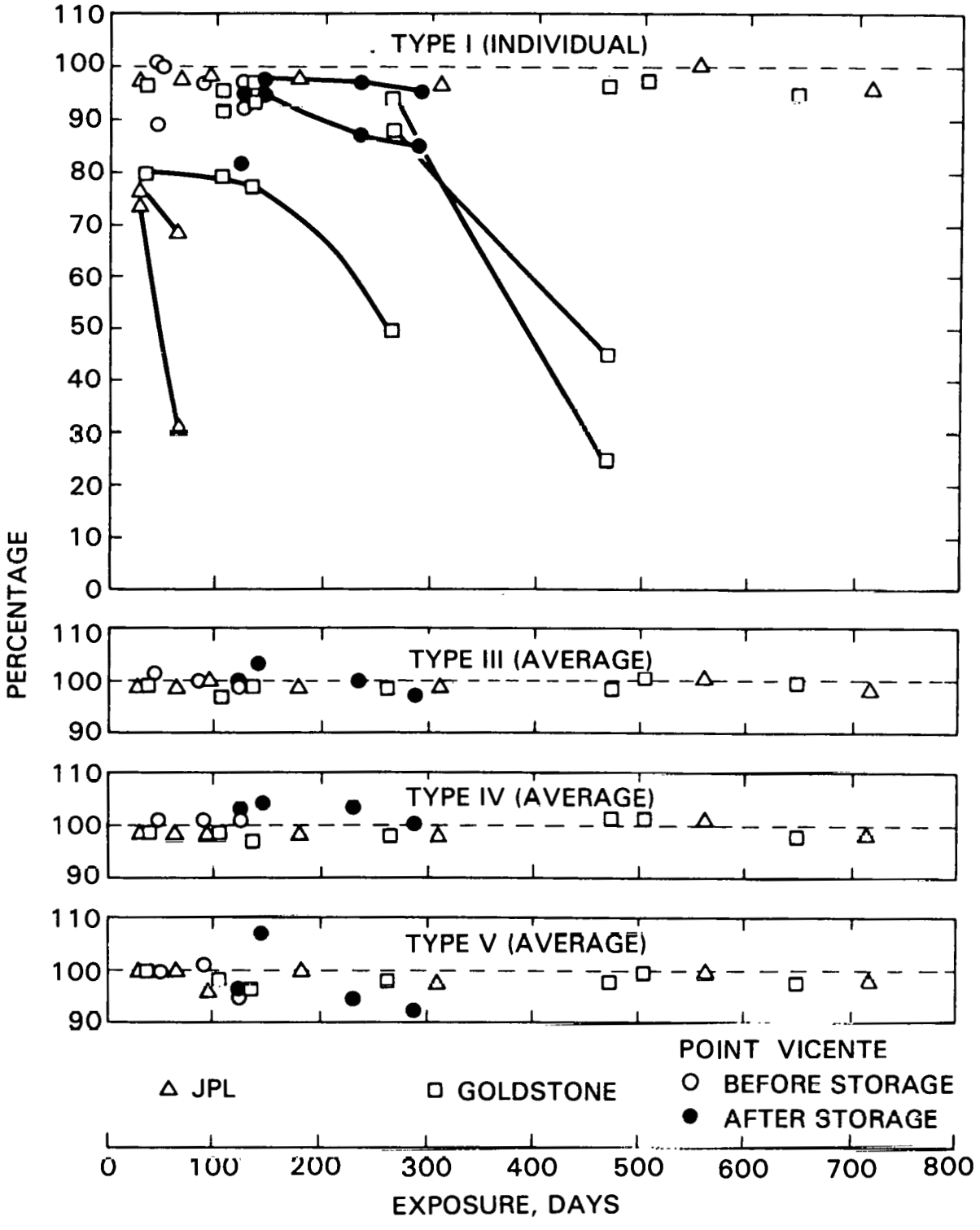

Figure 32. Minimodule Field-Test Results: Percentage of Initial Maximum Power Output as a Function of Outdoor Exposure Time

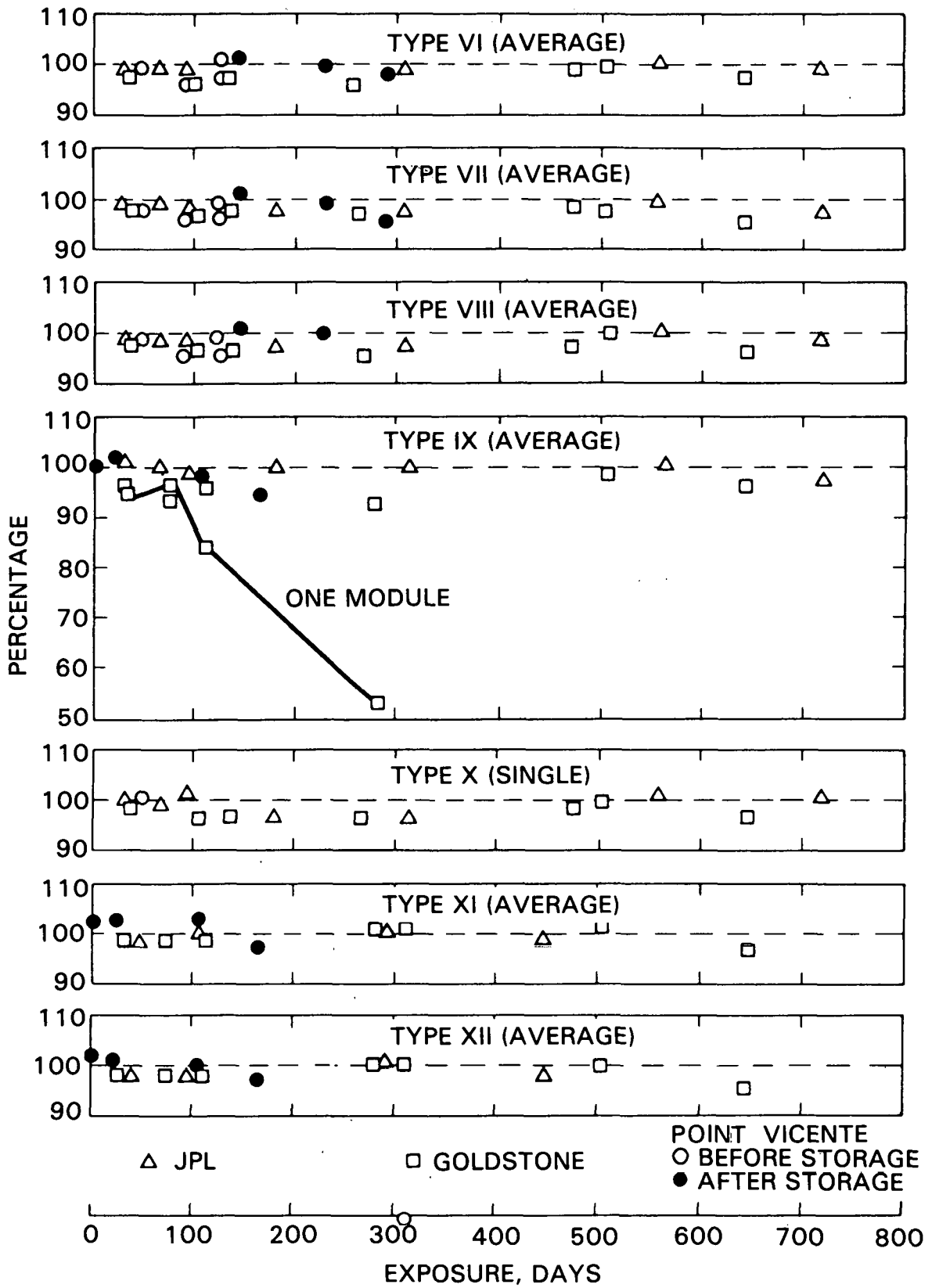

Figure 32. Minimodule Field-Test Results: Percentage of Initial Maximum Power Output as a Function of Outdoor Exposure Time (Cont'd)

The substrate material used for Types I and II is Super Dorlux hardboard that has been vacuum-encapsulated in EVA with a Craneglas layer on each side of the board. Type I has a Korad cover film; Type II uses a Tedlar cover.

The substrate for Type III is galvanized steel, also encapsulated in EVA with a Craneglas layer on each side of the metal; the cover is again Korad.

In these three types, the PV circuits are the same and make use of Solar Power Corp. cell assemblies.

In Type IV, the substrate is glass-reinforced concrete with an Acmetite moisture barrier on its inner surface. ARCO Solar, Inc. cell strings are used as the PV circuit.

c. Modules With Structural Superstrates. The eight modules of Types V through XII (Figure 31) represent five basic designs.

Type V uses a soda-lime glass superstrate, a PV circuit containing Solar Power Corp. cell strings encapsulated in EVA (clear above and white below), and an aluminum-foil back cover.

Types VI, VII, and VIII use a Sunadex glass superstrate, a PV circuit containing Applied Solar Energy Corp. (ASEC) cell strings encapsulated in EVA, and various backings; Type VI uses a layer of Craneglas between the EVA and a Mylar back cover; Type VII uses Craneglas between the EVA and an Acmetite back cover, and in Type VIII there is no Craneglas between the EVA and the Acmetite back cover. No submodules of these three types were produced.

In Type IX modules, two kinds of Spire Corp. cells are electrostatically bonded to a Corning 7070 borosilicate glass superstrate; EVA seals the back of the cells, and the back cover is Acmetite. No submodules of this type were produced.

In Type X modules, ASEC cell strings are bonded to a Sunadex glass superstrate by means of a room-temperature-vulcanized (RTV) silicone-rubber adhesive, then encapsulated in RTV silicone rubber; the back cover film is Acmetite. No submodules of this type were produced.

Types XI and XII use a soda-lime glass superstrate and ASEC cell strings potted in polyurethane; Type XI has no back cover; Type XII has an Acmetite film. No submodules of these types were produced.

3. Summary of Test Results

a. Laboratory Tests.

Environmental-Chamber Testing. Three designs degraded significantly during temperature cycling (Types I, III, and V); further degradation occurred during humidity-freeze testing of Types I, IV, and IX. These include all the designs with structural substrates--in particular, two

of the three modules incorporating Super Dorlux (Type I) showed dramatic power losses. This is related to the module manufacturing process, as discussed above. The modules incorporating galvanized steel (Type III) showed only borderline changes after temperature cycling and little change after humidity-freeze cycling. The encapsulant was wrinkled after each test, however, and probably cracked one or more cells as it deformed. Those with glass-reinforced concrete substrate (Type IV) withstood temperature cycling rather well but degraded during humidity-freeze cycling, when distortion of the encapsulant again led to cell cracking.

Of the other designs with evidence of degradation, Type V (glass superstrate, EVA encapsulant, and aluminum backing) showed borderline power loss after temperature cycling and little change during humidity-freeze cycling; once more, the encapsulant wrinkled during test. Type IX (cells electrostatically bonded to Corning 7070 borosilicate glass, EVA encapsulant, Acmetite backing) showed no loss after temperature cycling, yet one of the two modules failed completely after humidity-freeze cycling while the other showed no change. In both cases the glass superstrate cracked during test, which also cracked one or more cells. In one case this apparently opened the photovoltaic circuit; in the other it did not.

Hail Testing. Only two of the modules tested exhibited any signs of damage (Table 21). The Type VII module (CE130) cracked at the third hail impact at 52 mi/h (84 km/h). The position struck was near the edge of the panel and failure may have been due to an edge flaw in the glass superstrate. The Type IX module (SE104) cracked at each of the first four impacts at 25 mi/h (40 km/h), so testing was stopped.

Partial Discharge Testing. All module designs except those incorporating electrostatically bonded cells (Type IX) or RTV encapsulant (Type X) were evaluated in the JPL partial-discharge test facility; results are given in Table 22. In reviewing these data, it is important to remember that at an inception level of approximately 20 pC, the higher the values of both rms and peak test voltage, the better the module; the same is true at the 100-pC level. An accepted rule of thumb is that the inception voltage should be three to five times the operating voltage.

The comments as to type of partial discharge or other observations are important because leakage paths or shorts typically indicate a design or manufacturing flaw. A notation of "charging effect" indicates a floating ground. This effect is seen in two of the three superstrate designs that incorporate Acmetite film as the back cover (Types VIII and XII).

Nominal Operating Cell Temperature (NOCT). NOCT values for these experimental modules ranged from 40° to 46°C, as shown in Table 23.

b. Accelerated Testing in Concentrated Sunlight. Although analysis of this portion of the program has not been completed, several observations can be reported:

Table 21. Summary of Minimodule Hail Testing

Type	Serial Number	Result
Substrate		
I	DE113	Passed
III	DE143	Passed
IV	MB121	Passed
Substrate		
V	DE127	Passed
VI	CE114	Passed
VII	CE130	Cracked at edge only, third impact, at 52 mi/h (84 km/h)
VIII	CE143	Passed
IX	SE104	Failed: 4 cracks at 25 mi/h (40 km/h)
X	GE105	Passed
XI	PW110	Passed
XII	PW126	Passed

Three of the four minimodules, exposed on the SuperMaq*, failed electrically: DE114 (Type I), CE116 (Type VII), and SE103 (Type IX). Almost all submodules tested on the EMMAQUA* showed some electrical degradation, and modules DE502 and DE503 (Type II) specifically exhibited considerable structural damage. Interestingly, the other modules containing Super Dorlux, DE405 and DE410, were not as strongly affected. One of the submodules exposed on the EEKQUA* DE440 (Type I) failed, as did one of the submodules, DE242 (Type V), exposed on the 34-deg S racks*.

*DSET proprietary solar testing equipment.

Table 22. Summary of Minimodule Partial Discharge Testing

Type	Serial Number	Partial Discharge at Inception: Test Voltage, kV rms	Partial Discharge at Inception: Test Voltage, kV Peak	Partial Discharge at Inception: Charge, pC	Partial Discharge at Inception: Type of Partial Discharge	Partial Discharge at 100 pC Level: Test Voltage, kV rms	Partial Discharge at 100 pC Level: Test Voltage, kV Peak	Partial Discharge at 100 pC Level: Charge, pC	Partial Discharge at 100 pC Level: Type of Partial Discharge	Notes	Performance
I	DE110	4.6	6.44	25	Void	4.9	6.86	150	Voids		Very good
III	DE140	0.09	0.126	N.A.	19.5 k leakage path	-	-	-	-		Failed
IV	MB119	1.0	1.4	20	Voids	1.35	1.89	103	Voids		OK
V	DE116	250-Ω short between frame and cell				----------					Failed
VI	CE108	1.3	1.82	40	Void	1.6	2.24	225	Voids		OK
VII	CE127	1.1	1.54	60	Voids	1.25	1.75	160	Voids		OK
VIII	CE131	1.0	1.4	30	Voids	1.1	1.54	101	Voids		
	CE131	Rerun after trimming thermocouple leads				1.3	1.82	200	Flashover, void	Charging effect	OK
XI	PW107	1.8	2.52	25	Point to plane on frame	2.4	3.36	102	Point to plane on frame		OK
XII	PW122	-	-	-	-	0.5	0.7	230	Surface condition	Flashover at thermocouple, charging effect	Failed

Notes: All tests performed at room temperature. Types IX and X were not tested.

Table 23. Minimodule Nominal Operating Cell Temperature (NOCT)

Type	Serial Number	NOCT, °C
I	DE114	45.7
III	DE145	39.8
V	DE116	45.5
VI	CE109	42.2
VII	CE116	42.9
VIII	CE131	44.0

More complete physical examinations, large-area pulsed solar simulator (LAPSS) I-V curves, and failure analysis of the nonfunctional modules will be required before more can be said about these tests.

c. Field Exposure.

Soiling. Electrical degradation of the modules undergoing field exposure was monitored through changes in maximum power output calculated from LAPSS I-V curves.

Two groups of curves were obtained: the first with the unwashed modules, the second after they had been washed. In general, washed modules showed maximum power output gains that were consistently 2% to 6% higher (occasionally even more) after washing.

Electrical Performance. Figures 32 and 33 summarize the effects of field exposure on electrical performance of minimodules and submodules, respectively. Eight module types showed essentially no change in maximum power over 500 to 700 days of field exposure. However, those that incorporate Super Dorlux (Types I and II) began to degrade early, and in a number of cases failure also occurred early; e.g., relative maximum power outputs below 70% after less than 100 days exposure at JPL. This is again due to hygroscopic expansion and contraction of the hardboard substrate. The eventual result was cell cracking and power loss. One Type V minimodule at Point Vicente began to show power loss after 232 days of exposure, and one Type IX minimodule at Goldstone began to lose power after 77 days of exposure.

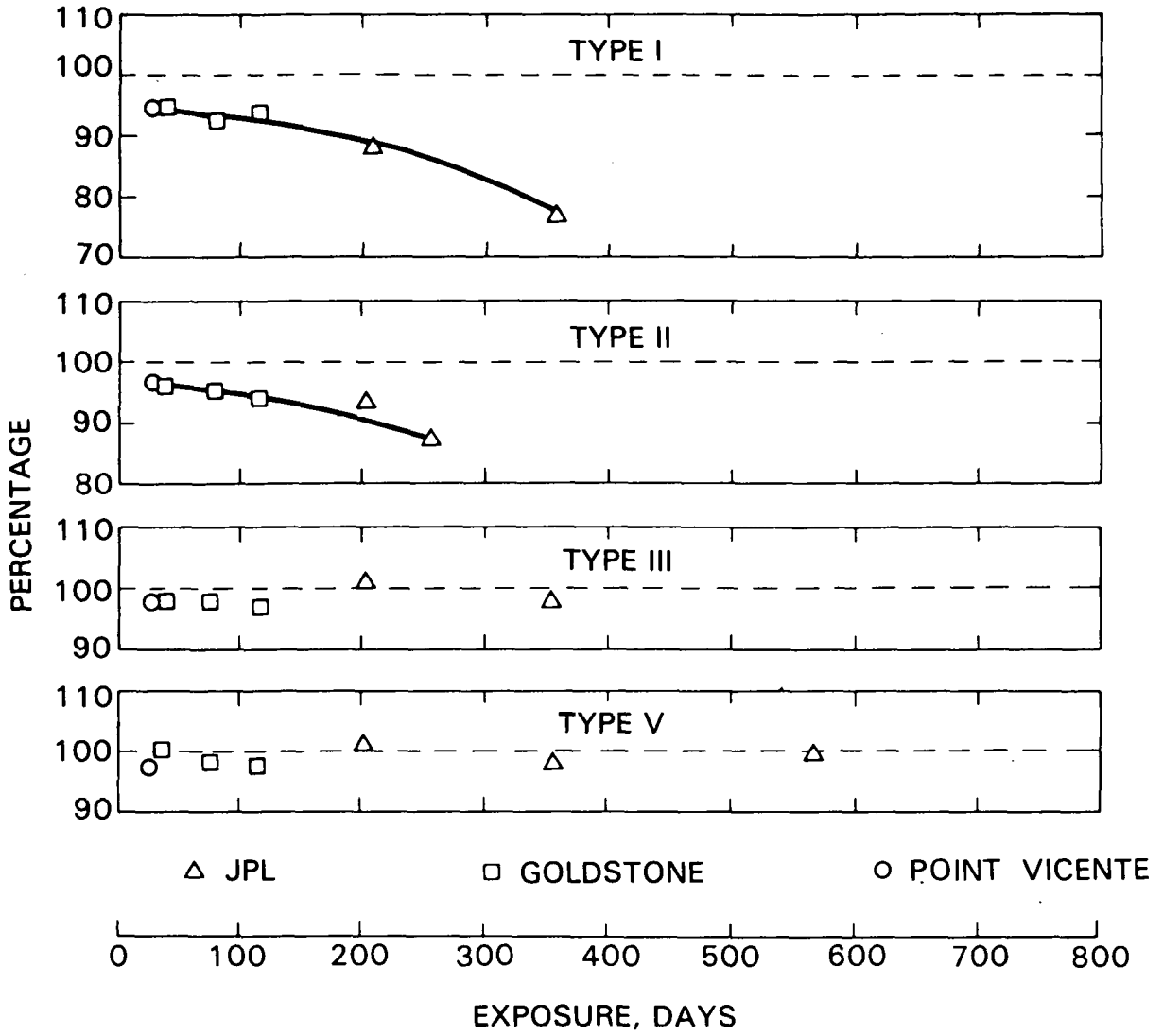

Figure 33. Submodule Field-Test Results: Percentage of Initial Maximum Power Output as a Function of Outdoor Exposure Time

Other changes have taken place in the modules that have not led to significant loss of maximum power output. At the JPL test site the following have been noted at the most recent examination of the minimodules:

(1) Cracking of Korad cover film over corner cell: DE101 (Type I) and DE132 (Type III).

(2) Widely spaced crazing of Korad film: DE131 (Type III).

(3) Crazing of Tedlar cover film: MB110, MB111, and MB112 (Type IV).

(4) Delamination of encapsulant: CE110 and CE111 (Type VI).

(5) Tarnish and occasional small corrosion spots on PV circuits: PW104, PW105, and PW106 (Type XI) and SE101 and SE102 (Type IX).

(6) Darkening of encapsulant near sealant: all DE modules (Types I, III, and V), all MB modules (Type IV) (intense), and the GE module, GE102 (Type X).

4. Discussion

Even though this field testing program has been in progress for only a short time compared with the intended 20-year life of commercial modules, several interesting observations have been made. For the most part, little degradation of maximum power output has occurred in modules other than Types I and II, which incorporate Super Dorlux, and Type IX, in which the cells are electrostatically bonded to Type 7070 borosilicate glass.

The failures of Types I and II modules result primarily from the hygroscopic contraction and expansion of the hardboard substrate, associated with the manufacturing process (see preceding subsection). A new manufacturing process calls for precoating both sides of the hardboard at room temperature with adhesive-bonded white plastic film and then adhesive-bonding the encapsulated cell string to the sandwich. Calculations indicate that such a technique will produce a substrate insensitive to humidity fluctuations.

The Type IX modules have been found to be quite easily degraded during laboratory testing. Two were subjected to temperature and humidity-freeze cycle testing; both glass superstrates cracked, implying that cells also cracked, and one of the modules lost electrical continuity. The hail-test module cracked at all four of the lowest-velocity impacts; the cover of the DSET SuperMaq module cracked early in testing. During field exposure the modules fared rather better: output of the two modules at JPL remain essentially unchanged after two years, and two of the three at Goldstone are essentially unchanged after 10 months, although one failed after nine months. The three at Point Vincente may have degraded slightly after five months.

There are two main causes of failure in Type IX modules. First, edge flaws may initiate cracks in the glass superstrate, even though it is reported to be stronger than window glass; since the solar cells are bonded directly to the glass, they crack along with it. Second, it has apparently been difficult to achieve good electrical bonding of the interconnects to the cells. Slight motions can therefore lead to increased contact resistance or even to loss of continuity altogether.

Soiling of all module types, measured by the increase in maximum power output after washing, seems to be slightly greater at the JPL Pasadena site than at Goldstone or Point Vicente. There appears to be a fairly consistent change of 2% to 4% for the JPL modules; the others are generally unchanged. This is consistent with other results obtained by exposure of various modules (Reference 25).

Otherwise, there is little difference between modules with glass superstrates and those with low-cost structural substrates. Similarly, there is little difference in maximum power output among modules employing EVA, polyurethane, or RTV silicone rubber as pottants. Whether Mylar, Acmetite, or aluminum foil is used as a back cover makes little difference.

G. PERFORMANCE OF ANTISOILING COATINGS

The accumulation of dust, dirt, pollen, and other atmospheric contaminants and particles on the surfaces of PV modules results in a loss of performance due to a decrease in transmitted sunlight. This accumulation of a diversity of deposited atmospheric materials, here simply referred to as soil, reduces light transmission by a combined action of absorption and scattering. To minimize performance losses caused by soiling, PV modules should have surfaces or surface coatings that have low soil retention, should have maximum susceptibility to natural cleaning by wind and rain, and should be readily cleanable by simple and inexpensive maintenance cleaning techniques.

One of FSA's tasks has been to seek a fundamental understanding of soiling mechanisms (References 1 and 26), and to identify therefrom the chemical, physical, and mechanical criteria for low-soiling surfaces or surface coatings.

Evolving soiling theories and physical examination of module surfaces suggest that surface soiling accumulates in three layers. The first layer involves strong chemical attachment, or strong chemisorption of soil matter on the primary surface. The second layer is physical, consisting of a highly organized arrangement of soil matter effecting a gradation in surface energy from a high, associated with the energetic first layer, to the lowest possible state on the outer surface of the second layer. The lowest possible surface energy state on this second layer is dictated by the chemical and physical nature of the regional atmospheric soiling materials.

These first two layers are resistant to removal by rain and wind. After the first two layers are formed, the third layer thereafter constitutes a settling of loose soil matter, accumulating in dry periods and being removed during rainy periods. The aerodynamic lifting action of wind can remove particles greater than about 50 μm from this layer, but is ineffective for smaller particles (Reference 27). Thus, the particle size of soil matter in the third layer is generally found to be less than 50 μm (Reference 28).

Figure 34 illustrates the generally observed time dependence of the natural soiling behavior on material surfaces. The oscillating solid line traces the time-dependent magnitude and behavior of the surface soiling, which increases during dry periods and decreases during rainy periods.

Consistent with the soil-layering concept, the curve of Figure 34 reflects the existence of rain-resistant and rain-removable soil layers. The dotted line connecting the minima is associated with the light obscuration caused by the development of two rain-resistant layers; the solid, oscillating line riding on the dotted line is associated with the light obscuration caused by the rain-controlled third layer.

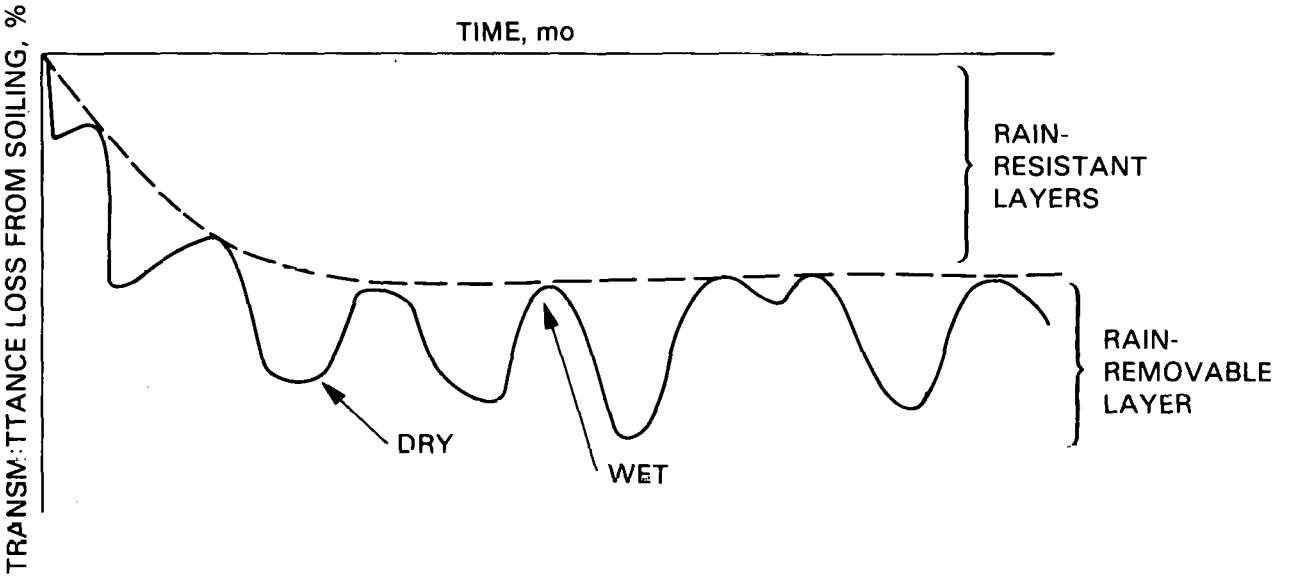

Figure 34. Behavior of Natural Outdoor Soiling

Theories and evidence suggest that surfaces that should be naturally resistant to the formation of the first two rain-resistant layers are hard, smooth, hydrophobic, and free of first-period elements (for example, sodium), and have the lowest possible surface energy. These evolving requirements for low-soiling surfaces suggest that surfaces, or surface coatings, should be based on fluorocarbon chemistry.

Two fluorocarbon coating materials, a fluorinated silane (L-1668, E-3820, 3M Co.,), and perfluorodecanoic acid, are under test. The L-1668 contains chemically reactive function groups for chemical attachment to surfaces, and the perfluorodecanoic acid is chemically attached to the surfaces with a Dow Corning chemical primer, Z-6020. The two chemically attachable fluorocarbon coatings are being tested on the surfaces of outer-cover materials that are being evaluated for PV modules: Sunadex (ASG) soda-lime glass, and Acrylar (3M) and Tedlar (Du Pont) UV-screening plastic films. L-1668 and E-3820 will attach chemically to the surfaces of these three outer cover materials, but it was found that the chemical attachment of E-3820 to Acrylar and L-1668 to Tedlar is weak. Therefore, for these specific coatings, the surfaces of the plastic films were treated with ozone to generate polar groups for enhanced chemical reactivity and therefore enhanced chemical attachment. This technique worked, and although not indicated as needed from trial testing, L-1668 was also applied to an ozone-treated Acrylar surface, and E-3820 was also applied to an ozone-treated Tedlar surface.

The coatings on glass, and on the two films, are being exposed outdoors in Enfield, Conn., and the loss of optical transmission by natural soil accumulation is being monitored by the percentage of reduction in short-circuit current (I_{sc}) of standard solar cells positioned behind the glass and film test specimens. These test specimens are not washed.

Table 24 records the percentage of reduction in I_{sc} for all of the test specimens over 23 months of continuous outdoor exposure (Reference 29). I_{sc} is measured monthly. For Tedlar, the best coating is found to be E-3820, and Figure 35 compares the soiling behavior of uncoated Tedlar (control) and E-3820 coated Tedlar. For Acrylar, the best coating is found to be E-3820 in combination with ozone, and Figure 36 compares the soiling behavior of uncoated Acrylar (control) and the E-3820-ozone-coated Acrylar specimen. For glass, little difference is noted in comparing E-3820 and L-1668, but E-3820 may be slightly better (Figure 37).

Comparing the uncoated controls, glass has the least tendency to retain natural soil, followed by Tedlar and then Acrylar, both having the greater tendencies to retain natural soil. This difference in soiling behavior between glass and plastic films had been observed earlier (References 25 and 30). However, with the fluorocarbon antisoiling coatings, the soiling behavior of all three materials becomes essentially the same. Thus soiling-related energy losses of glass superstrate designs and substrate designs with plastic film outer covers will be essentially the same.

Figure 38 is a plot of the rainfall pattern in Enfield, Connecticut, over the soiling exposure period. The data are plotted as monthly rainfall totals in inches versus the month in which the rainfall occurred. The highs and lows in the rainfall totals generally correlate with the soiling highs and lows shown in Figures 35, 36, and 37. A sustained dry period with little rain occurred during the fourth to the tenth month, with no rain at all in the eighth and ninth months. This resulted in the maximum accumulation of surface soiling observed from all test specimens over the entire outdoor exposure period. After the ninth and tenth months, rainfall began to increase, and the surfaces became cleaner.

Over this exposure period, the monthly rainfall totals were accumulated from a fair number of rainstorms distributed throughout this month. In the 21st month, however, an especially intense and heavy rainstorm of several days' duration accounted for almost all of the monthly total. As shown in Figures 35, 36, and 37, this intense rainstorm removed virtually all of the measurable soil from the fluorocarbon-coated surfaces.

Inspection of the control data curves in Figures 35, 36, and 37 reveals the formation of a rain-resistant soil base on each of the three materials. This amounts to about 2% loss for glass, 4.1% loss for Tedlar, and about 6.2% loss for Acrylar. Soiling data measured on similar materials in Pasadena, California (Reference 25), showed about 3% loss for glass, 3% loss for Tedlar, and 5% loss for Korad acrylic film, which is similar in chemistry to Acrylar. Inspection of the fluorocarbon-coated-surface data curves in Figures 35, 36, and 37 suggest that little, if any at all, of a rain-resistant soil base had formed on these surfaces.

Outdoor exposure testing will continue.

Table 24. Experimental Evaluation of Fluorocarbon Antisoiling Coatings, Monitored by Measurements of Percentage Reduction in Solar-Cell Short-Circuit (I_{sc}) From Accumulation of Natural Surface Soiling (Reference 29)

Materials	MONTHS																						
	1	2	3	4	5	6	7	8	9	10	11	12	13	14	15	16	17	18	19	20	21	22	23
Sunadex Glass																							
Control	1.5	2.0	1.9	1.7	3.0	2.8	2.3	2.9	4.1	3.2	2.0	3.1	3.8	2.3	1.9	2.4	2.5	1.7	4.0	3.7	2.2	2.0	3.2
L-1668	0.0	1.2	1.3	0.3	0.4	0.4	1.0	1.0	4.3	2.3	1.0	1.0	1.5	1.0	2.1	3.0	2.0	1.7	3.3	3.0	0.0	2.9	2.1
E-3820	0.1	0.1	2.2	1.2	1.5	1.2	2.3	2.0	3.8	2.7	0.6	1.3	1.7	0.8	1.6	1.6	1.5	1.1	2.6	2.0	0.0	0.5	2.3
Tedlar 100BG30UT																							
Control	2.4	3.3	1.0	3.5	4.7	4.7	5.1	6.3	7.7	8.8	6.7	6.5	5.8	4.5	5.0	4.9	4.6	5.8	6.3	6.2	5.0	4.1	7.4
L-1668	1.5	1.5	2.7	1.8	3.8	2.9	3.5	3.7	6.0	5.3	3.9	4.2	5.3	4.6	5.3	5.0	4.9	5.4	6.0	6.0	4.4	4.9	5.4
L-1668/ozone	0.7	0.9	2.1	2.2	2.8	3.1	3.5	3.4	5.9	5.0	3.7	4.8	5.1	4.4	5 0	5.4	5.7	5.2	5.1	5.1	2.3	4.4	6.0
E-3820	0.0	0.0	3.5	0.8	1.5	1.7	0.9	1.3	2.4	3.8	2.1	2.4	2.3	2.3	1 7	1.8	1.6	1.7	2.3	2.8	0.0	0.9	0.4
E-3820/ozone	3.2	2.9	0.0	2.4	3.9	3.7	4.3	4.4	5.8	6.4	3.9	4.1	4.4	3.2	5 5	5.8	6.5	5.8	5.6	6.9	4.3	4.1	6.6
Acrylar X-22417																							
Control	3.1	3.9	4.4	3.7	5.1	5.4	6.4	7.5	10.2	10.8	7.9	7.8	8.1	6.4	7.2	7.6	7.2	7.3	9.4	9.8	6.2	7.3	8.2
L-1668	0.8	0.4	1.8	2.1	3.5	3.5	5.0	3.9	5.1	6.6	5.6	5.0	4.9	3.2	4.6	5.0	4.7	4.7	6.4	6.2	0.9	2.6	5.3
L-1668/ozone	2.9	2.5	2.8	2.5	3.4	3.2	4.5	5.0	6.3	6.1	4.5	4.6	6.1	5.3	4.8	5.5	5.6	5.3	7.5	6.7	2.8	5.9	6.5
E-3820	1.5	1.6	2.4	2.3	2.8	2.6	3.9	3.9	6.7	6.8	4.4	5.4	6.0	4.2	5.0	4.0	3.6	5.5	6.0	5.7	1.3	4.3	4.6
E-3820/ozone	0.8	2.0	2.3	1.8	2.5	3.1	4.0	3.2	5.0	4.9	3.2	4.0	4.9	3.8	1.0	2.1	1.4	1.0	2.6	3.8	0.0	2.0	1.9

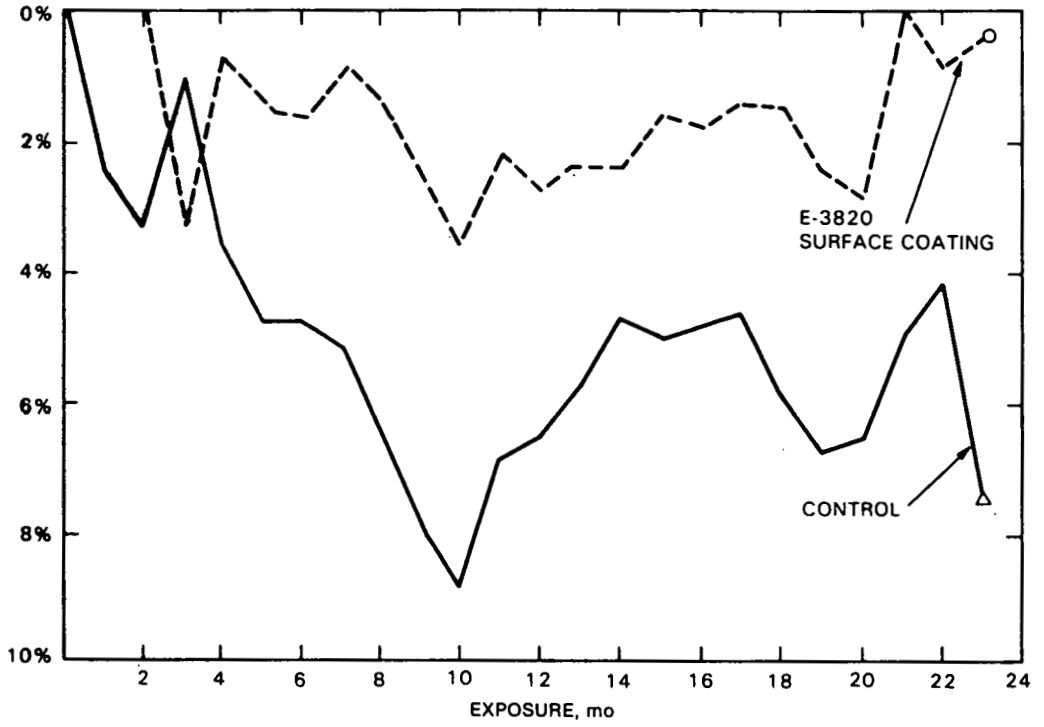

Figure 35. Outdoor Soiling Behavior of Tedlar 100BG30UT Plastic Film, With and Without a Fluorocarbon Antisoiling Coating

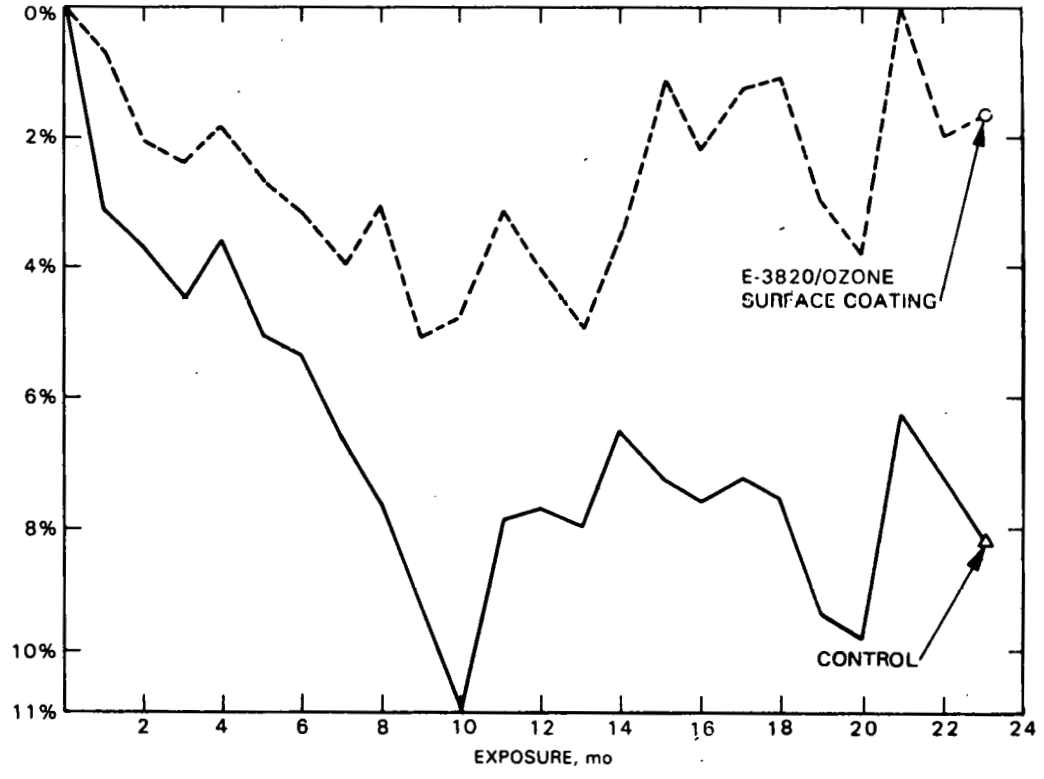

Figure 36. Outdoor Soiling Behavior of Acrylar X-22417 Plastic Film, With and Without a Fluorocarbon Antisoiling Coating

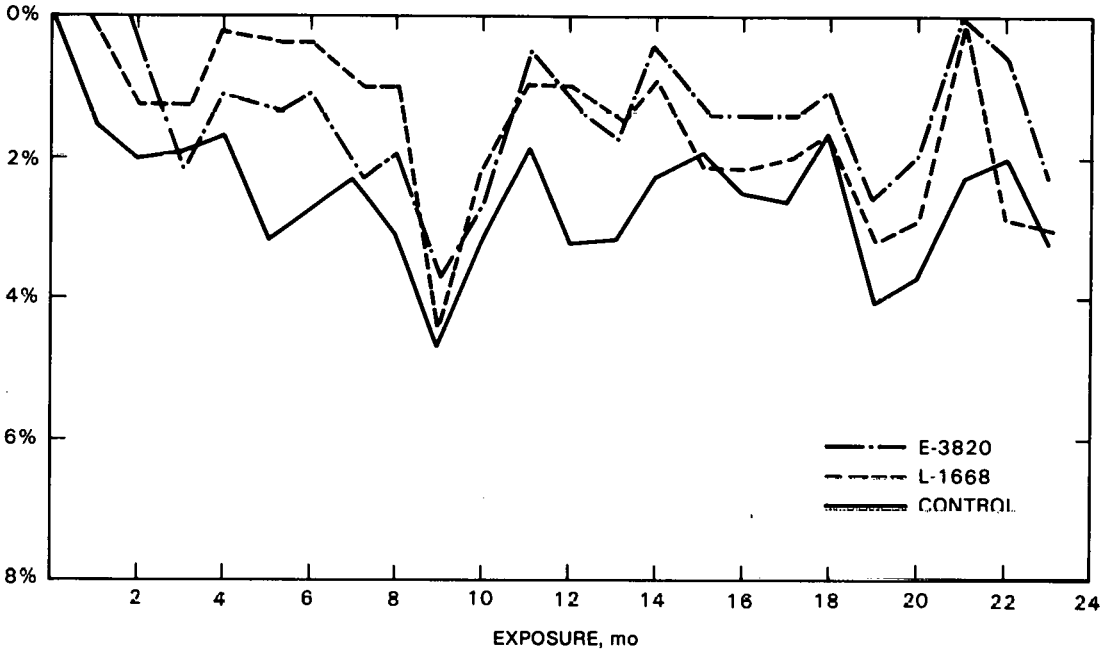

Figure 37. Outdoor Soiling Behavior of Sunadex Glass, With and Without a Fluorocarbon Antisoiling Coating

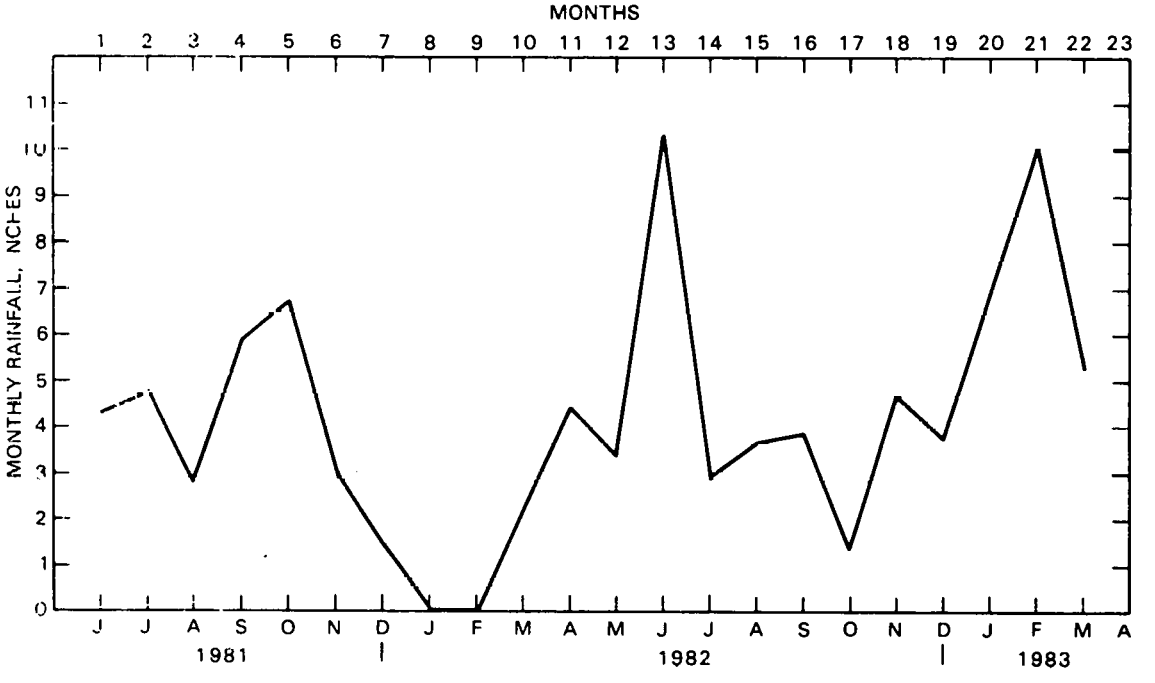

Figure 38. Monthly Rainfall in Enfield, Connecticut, for the Period June 1, 1981 to March 31, 1983

H. EVALUATION OF SHRINKAGE IN TEDLAR FILMS

1. Introduction

Shrinkage of white-pigmented Tedlar film used in PV modules has been experienced by various manufacturers. The condition appears on one end of the affected module after thermal cycling tests from -40° through +90°C. It has been observed only in the long direction of rectangular modules.

Du Pont has indicated that residual internal stresses that can cause shrinkage occur in Tedlar as a result of the manufacturing process. The film material is extruded at elevated temperatures and pulled in the machine direction under tension (see Figure 39 for definitions of conventional nomenclature). This results in residual stress and shrinkage in the machine direction and the transverse direction of the film, but the stress and shrinkage are different in the two directions.

A test program was designed to provide the coefficient of expansion characteristics, dimensional changes, and magnitudes of the shrinkage forces of two Tedlar films of different thicknesses (1.5 and 4.0 mils). The data were obtained on as-received and stress-relieved specimens. In addition, tests were conducted in both the machine and the transverse directions.

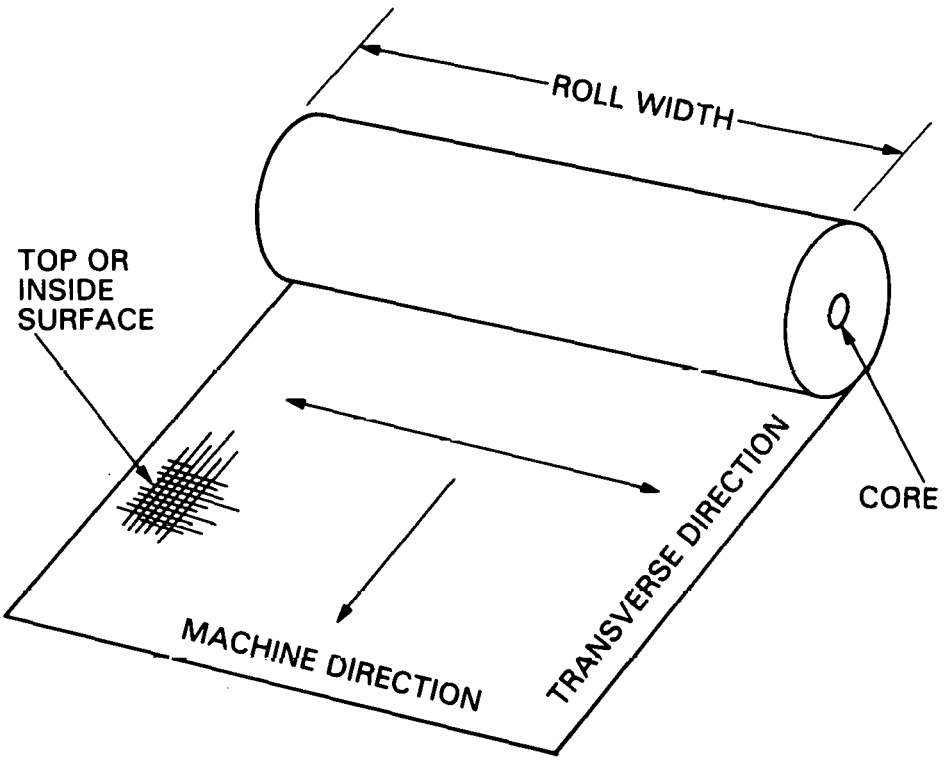

Figure 39. Nomenclature for Rolls of Tedlar Film

2. General

Two types of Tedlar film were obtained: 150-BL30WH and 400-BS30WH. Specimens were tested as received and after being stress-relieved for one hour at 100°C, 150°C and 200°C. The specimens that were stress-relieved for one hour at 200°C were excessively shrunken and distorted, and were not suitable for use as test specimens.

Dimensional changes were obtained while the test specimens were temperature-cycled from -40° through +90°C. Similarly, the changes in force with the specimens held at constant length were measured as the temperature was cycled. Specimens were mounted with the film oriented in both the machine and transverse directions.

The sample size was as large as the test chamber could accommodate. The temperature range is the same as that used in module quality-control tests (Reference 31).

Separate test specimens were used for each test during evaluation of as-received properties. Some of the same stress-relieved test specimens were used in both dimensional and force measurements, with dimensional evaluations done first.

XY measurements were obtained at the temperatures shown below:

(1)	Ambient	(7)	+75°	(13)	-20°
(2)	+30°C	(8)	+60°	(14)	-40°
(3)	+45°	(9)	+45°	(15)	-20°
(4)	+60°	(10)	+30°	(16)	0°
(5)	+75°	(11)	+15°	(17)	+15°
(6)	+90°	(12)	0°	(18)	Ambient

The procedures followed in the study of expansion and contraction forces were:

(1) Mount the sample in the sample holders.

(2) Mount the sample in an Instron oven that has a glass door of sufficient size to permit visual examination.

(3) Attach the sample holders in the jaws of the Instron machine, using a 0-to-200-pound-load cell.

(4) Preload the test sample to 1 lb at +30°C.

(5) Record visible effects (e.g., wrinkling and sagging).

The temperature cycle as shown in the list of temperatures above was used with as-received specimens. Most of the remainder were tested at +30°, down to -40°, and back to +30°C, because the preconditioned specimens had already been exposed to the +90oC test temperature.

3. Results

Tables 25, 26 and 27 present a summary of the test results. Both Tedlar films reacted similarly. The main reorientation is in the machine direction, as expected. The aging at 150° gave results that indicated slightly more stress relief than aging at 100°C. Aging at 200°C virtually destroyed the specimens.

The coefficient of expansion data in Tables 26 and 27 reflect similar results. The coefficients of expansion of the control specimens were taken from plots of the data after the initial temperature increase to +90°C and the subsequent cycle to -40°C as shown in Figures 40 and 41. Length measurements of control specimens during the initial increase in temperature show that the Tedlar was shrinking, even though the coefficient of expansion was counteracting the stress-relieving phenomenon. Plots of the data in the Y axis were consistent; those in the X axis were erratic, because the specimens were retained, on the top and bottom, in specimen holders along the X axis. Wrinkles generally appeared at temperatures higher than 100°C.

Although the stress relief was effective, the data show that some orientation effects on the coefficient of expansion, shrink force and tensile strength were retained. The shrink force is expressed in lb/in. width per degree Celsius. Interestingly, the tensile strengths were higher in the transverse direction than in the machine direction.

4. Conclusions

Stress relief of free-standing Tedlar films can be effective in reducing stresses in PV modules. The duration of 1 h was chosen arbitrarily. The temperature cycling of non-relieved material indicated that this could be reduced to a few minutes.

Although stress relief was more pronounced at 150°C, the maximum processing and/or subsequent qualification test temperatures should be acceptable.

5. Summary

Commercially produced white-pigmented Tedlar (Du Pont) plastic films retain manufacturing-induced internal stresses that can lead to irreversible shrinkage when the films are heated above 45°C to 50°C. This shrinkage behavior appears to be a one-time event associated with the initial heating of fresh film. These internal stresses and their resultant shrinkage can thereforebe relieved by preheating free-standing film before use in a photovoltaic module. However, these same internal stresses and shrinkage tendencies are apparently not relieved if first-time heating of the film happens to be associated with the module lamination process. This is believed to be caused by lamination pressure, which constrains the film mechanically from self-relief, deferring the relief mechanism until the fabricated module is heated later during a thermal qualification test.

Table 25. Dimensional Stress Relief of 12 x 12 Tedlar Specimens After 1 Hour

Test Temperature, °C	Orientation	
	Machine	Transverse
	150-BL30WH	
100	11.74 (-2.2%)	12.15 (+1.3%)
150	11.50 (-4.2%)	12.16 (+1.3%)
200	Specimens not usable due to shrinkage and distortion	
	400-BS30WH	
100	11.83 (-1.4%)	12.04 (+0.3%)
150	11.60 (-3.3%)	11.96 (-0.3%)
200	Specimens not usable due to shrinkage and distortion	

Table 26. Test Data, Tedlar 400-BS30WH

Specimen Description	Coefficient of Expansion, in./in.-°C-10^{-6}	Shrink Force, lb/in.-°C	Tensile Strength, $lb/in.^2$
As Received			
Machine Direction	75.1	0.188	8310
Transverse Direction	60.7	0.028	12435
Stress-Relieved, 1 h at 100°C			
Machine Direction	83.4	0.135	10570
Transverse Direction	55.3	0.105	14540
Stress-Relieved, 1 h at 150°C			
Machine Direction	76.2	0.123	10965
Transverse Direction	64.7	0.111	15315

Table 27. Test Data, Tedlar 150-BL30WH

Specimen Description	Coefficient of Expansion, in./in.-^{o}C-10^{-6}	Shrink Force, lb/in.-^{o}C	Tensile Strength, lb/in.^{2}
Control			
Machine Direction	67.2	0.068	9480
Transverse Direction	57.5	0.005	13650
Stress-Relieved, 1 h at 100^{o}C			
Machine Direction	75.5	0.040	11560
Transverse Direction	57.5	0.031	11570
Stress-Relieved, 1 hr at 150^{o}C			
Machine Direction	81.5	0.042	11785
Transverse Direction	57.5	0.035	15005

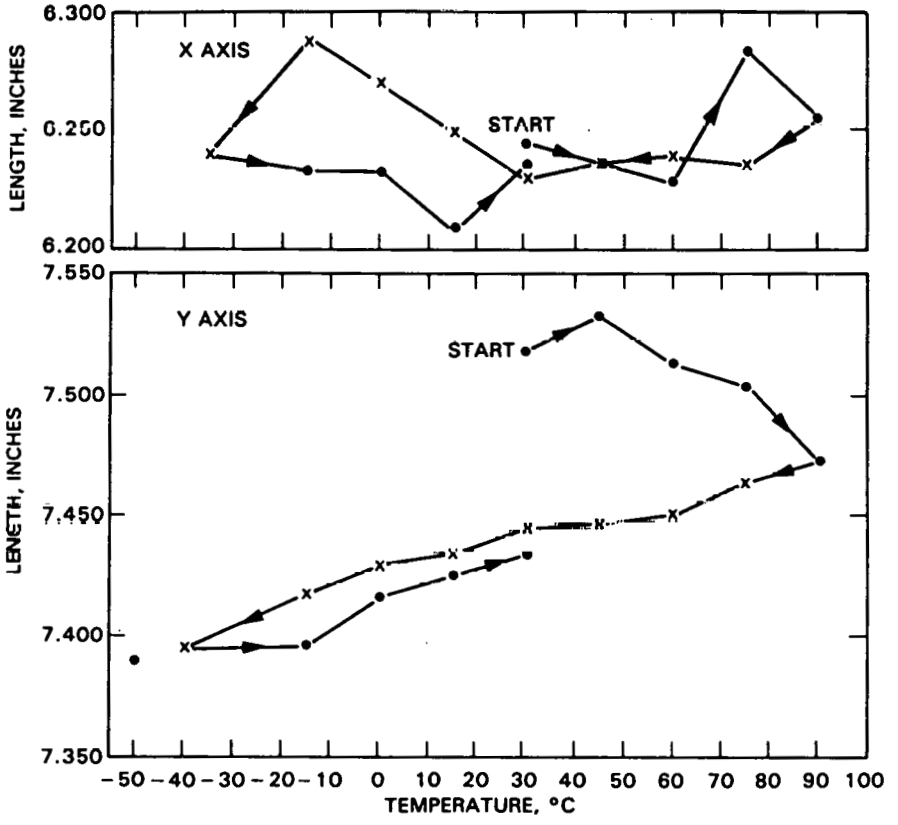

Figure 40. Tedlar Film 150BL30WH Control, Machine Direction

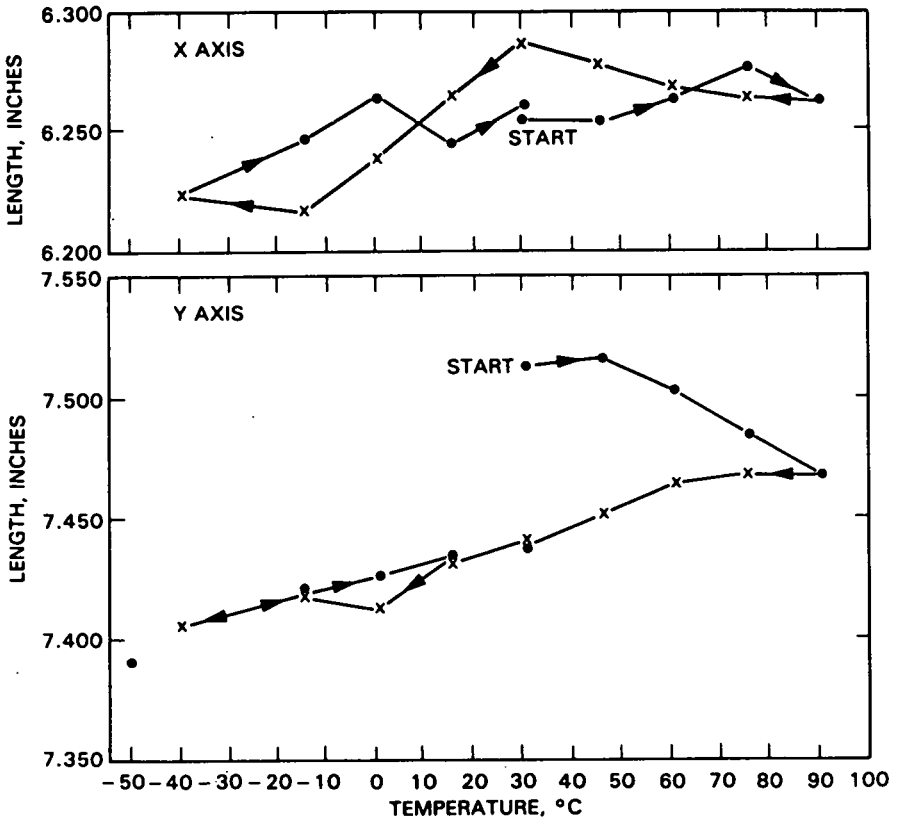

Figure 41. Tedlar Film 400BS30WH Control, Machine Direction

REFERENCES

1. Cuddihy, E., et al, Photovoltaic Module Encapsulation Design and Materials Selection: Volume I, JPL Publication 81-102, JPL Document No. 5101-177, DOE/JPL-1012-56, Jet Propulsion Laboratory, Pasadena, California, June 1, 1982.

2. Cuddihy, E.F., et al, Applications of Ethylene Vinyl Acetate as an Encapsulation Material for Terrestrial Photovoltaic Modules, JPL Publication 83-35, JPL Document No. 5101-220, Jet Propulsion Laboratory, Pasadena, California, April 15, 1983.

3. Willis, P., and Baum, B., Investigations of Test Methods, Material Properties, and Processes for Solar-Cell Encapsulants, Annual Report, DOE/JPL-954527-83/24, Springborn Laboratories, Inc., Enfield, Connecticut, July 1983.

4. Willis, P., and Baum, B., Investigations of Test Methods, Material Properties, and Processes for Solar-Cell Encapsulants, Annual Report, Springborn Laboratories, Inc., Enfield, Connecticut, DOE/JPL 954527-80-15, Jet Propulsion Laboratory, Pasadena, California, July 1981.

5. Coulter, D.R., Cuddihy, E.F., and Plueddemann, E.P., Chemical Bonding Technology for Terrestrial Photovoltaic Modules, JPL Publication 83-86, JPL Document No. 5101-232, DOE/JPL-1012-91, Jet Propulsion Laboratory, Pasadena, California, November 15, 1983.

6. Design and Analysis of Advanced Encapsulation Systems for Terrestrial Photovoltaic Modules, 1983 Annual Report, Spectrolab, Inc., Sylmar, California (in press).

7. Spectrolab, Inc., Phase I Technical Report for Flat-Plate Solar Array Project Contract 955567, November 1981.

8. Stultz, J.W., Thermal and Other Tests of Photovoltaic Modules Performed in Natural Sunlight, JPL Document No. 5101-76, DOE/JPL-1012-78/9, Jet Propulsion Laboratory, Pasadena, California, July 31, 1978.

9. Wen, L., An Investigation of the Effect of Wind Cooling on Photovoltaic Arrays, JPL Publication 82-28, JPL Document No. 5101-201, DOE/JPL-1012-69, Jet Propulsion Laboratory, Pasadena, California, March 1982.

10. Raithby, G.D., and Hollands, H.G.T., "A General Method of Obtaining Approximate Solutions to Laminar and Turbulent Free-Convection Problems," Advances in Heat Transfer, Vol. II, pp. 265-315, ed. T.F. Irvine and J.P. Hartnett, Academic Press, 1975.

11. McAdams, W.H., Heat Transmission, 3rd Edition, McGraw-Hill Book Co., Inc., New York, 1954.

12. Ware, J.C., "Clear Sky Temperature," presented at ISES Meeting, Fort Collins, Colorado, August 1974.

13. Stultz, J.W., and Wen, L., Thermal Performance Testing and Analysis of Photovoltaic Modules in Natural Sunlight, JPL Internal Document No. 5101-31, Jet Propulsion Laboratory, Pasadena, California, July 29, 1977.

14 Cuddihy, E.F., Development of Reduced-Variable Master Curves for Estimating Tensile Stresses of Encapsulated Solar Cells Caused by Module Deflection or Thermal Expansion, JPL Internal Document No. 5101-182, October 1, 1981.

15. Moore, D.M., Proposed Method for Determining the Thickness of Glass in Solar Collector Panels, JPL Publication 80-34, JPL Document No. 5101-148, DOE/JPL-1012-41, Jet Propulsion Laboratory, Pasadena, California, March 1, 1980.

16. Publications of the Biannual Conference Records of the IEEE International Symposiums on Electrical Insulation, IEEE Society, 1976 to 1982.

17. Mon, G.R., "Defect Design of Insulation Systems for Photovoltaic Modules," presented at 15th IEEE Photovoltaic Specialists Conference, Kissimmee, Florida, May 12-15, 1981.

18. Proceedings of the Flat-Plate Solar Array Project Research Forum on Quantifying Degradation, JPL Publication 83-52, JPL Document No. 5101-231, DOE/JPL-1012-89, Jet Propulsion Laboratory, Pasadena, California, June 1982.

19. Tests for Dielectric Breakdown Voltage and Dielectric Strength of Electrical Insulating Materials at Commercial Power Frequencies, ASTM D-149-64, 1970.

20. Ashcraft, A.C., Eichhorn, R.M., and Shaw, R.G., "Laboratory Studies of Treeing in Solid Dielectrics and Voltage Stabilization of Polyethylene," Paper No. F4, Conference Record of the 1976 IEEE International Symposium on Electrical Insulation, IEEE Society, 1976.

21. Mason, J.M., "Dielectric Breakdown in Solid Insulation," Chapter 1 in Progress in Dielectrics, Volume I, Ed. J.B. Birks and J.H. Shulman, Heywood and Company, Ltd., London, 1959.

22. Maxwell, H.G., et al, FSA Field Test Report 1980-1982, JPL Publication 83-29, JPL Document No. 5101-215, DOE/JPL-1012-85, Jet Propulsion Laboratory, Pasadena, California, April 15, 1983.

23. Rogers, C., "Permeability and Chemical Resistance," Chapter 9 in Engineering Design for Plastics, ed. E. Baer, Reinhold Publishing Co., New York, 1964.

24. Terrestrial Service Environments for Selected Geographic Locations, ERDA/JPL-954328-76/5, Battelle Columbus Laboratories, Columbus, Ohio, June 24, 1976.

25. Hoffman, A.R., and Maag, C.R., Photovoltaic Module Soiling Studies, May 1978 to October 1980, JPL Publication 80-87, JPL Document No. 5101-131, DOE/JPL-1012-49, Jet Propulsion Laboratory, Pasadena, California, November 1, 1980.

26. Cuddihy, E.F., "Theoretical Considerations of Soil Retention," Solar Energy Materials, Vol. 3, pp. 21-33, 1980.

27. Schneider, H., "Mechanical Removal of Spacecraft Microbial Burden," Subtask I of Spacecraft Cleaning and Decontamination Techniques, Chapter 6 of Planetary Quarantine, Annual Review, Space Technology and Research, JPL TR-900-597, Jet Propulsion Laboratory, Pasadena, California, February 1973.

28. Roth, E.P., and Anaya, A.J., "The Effect of Natural Cleaning on the Size Distribution of Particles Deposited on Silvered Glass Mirrors," presented at the Second Solar Reflective Materials Workshop, sponsored by the U.S. Department of Energy, San Francisco, California, February 12-14, 1980.

29. Willis, P.B., and Baum, B., Investigation of Test Methods, Material Properties, and Processes for Solar Cell Encapsulants, Annual Report, Springborn Laboratories, Inc., Enfield, Connecticut, DOE/JPL-954527-82/83, July 1982.

30. Hoffman, A.R., and Maag, C.R., "Airborne Particulate Soiling of Terrestrial Photovoltaic Modules and Cover Materials," Proceedings of the Institute of Environmental Sciences, Philadelphia, Pennsylvania, May 11-14, 1980, Institute of Environmental Sciences, Mt. Prospect, Illinois, 1980.

31. Griffith, J.S., Environmental Testing of Block III Solar Cell Modules, Part I: Qualification Testing of Standard Production Modules, JPL Publication 79-92, JPL Document No. 5101-134, DOE/JPL-1012-31, Jet Propulsion Laboratory, Pasadena, California, September 1, 1979.

☆ U. S. GOVERNMENT PRINTING OFFICE:1984--746-081/10125